

2023-12-01

Evaluation Of Inconel 718 Laser Powder Bed Fusion Angled Wall Artifact

Laura Itzel Marquez
University of Texas at El Paso

Follow this and additional works at: https://scholarworks.utep.edu/open_etd



Part of the [Engineering Commons](#)

Recommended Citation

Marquez, Laura Itzel, "Evaluation Of Inconel 718 Laser Powder Bed Fusion Angled Wall Artifact" (2023).
Open Access Theses & Dissertations. 3995.
https://scholarworks.utep.edu/open_etd/3995

This is brought to you for free and open access by ScholarWorks@UTEP. It has been accepted for inclusion in Open Access Theses & Dissertations by an authorized administrator of ScholarWorks@UTEP. For more information, please contact lweber@utep.edu.

EVALUATION OF INCONEL 718 LASER POWDER BED FUSION
ANGLED WALL ARTIFACT

LAURA ITZEL MARQUEZ

Master's Program in Mechanical Engineering

APPROVED:

Francisco Medina, Ph.D., Chair

Ryan Wicker, Ph.D.

Amit Lopes, Ph.D.

Stephen L. Crites, Jr., Ph.D.
Dean of the Graduate School

Copyright ©

by

Laura Itzel Marquez

2023

Dedication

I dedicate this thesis to my parents for their endless love, support, and encouragement throughout my education. Who has been my source of inspiration and gave me strength. I hope this achievement will fulfill the dream they envisioned of me.

EVALUATION OF INCONEL 718 LASER POWDER BED FUSION
ANGLED WALL ARTIFACT

by

LAURA ITZEL MARQUEZ, B.S.M.E

THESIS

Presented to the Faculty of the Graduate School of
The University of Texas at El Paso
in Partial Fulfillment
of the Requirements
for the Degree of

MASTER OF SCIENCE

Department of Aerospace and Mechanical Engineering

THE UNIVERSITY OF TEXAS AT EL PASO

December 2023

Acknowledgements

I would like to express my deepest gratitude to my research advisor, Dr. Medina, for his invaluable guidance, mentorship, and unwavering support throughout my academic journey at the Keck Center. Dr. Medina, you have been not only an advisor but also a source of inspiration, encouraging me to set and achieve ambitious goals in my research and studies. I am truly grateful for the opportunity you gave me to embark on this remarkable journey, starting as an undergraduate research assistant and continuing as a graduate research assistant. Your trust in my abilities has been instrumental in shaping my academic and professional growth. Your continuous guidance and belief in my potential have fueled my passion for additive manufacturing technologies and the limitless possibilities they hold for future development.

Kurtis, I want to express my sincere gratitude for your exceptional support during my graduate studies. Your assistance has been invaluable, and I appreciate your willingness to help whenever I needed it. Your support made a significant difference in my experience, and I'm thankful for it.

I also want to express our sincere gratitude to Leslie Trejo for her invaluable contributions to this research. Your expertise, insight, and unwavering commitment have been integral to the success of this study. I also extend my heartfelt thanks to all the students at the W.M. Keck Center for 3D Innovation who have been supportive and encouraging collaborators in this research endeavor. Your camaraderie and shared dedication to advancing our field have been a source of motivation and camaraderie that I will always cherish.

Lastly, but most importantly, I want to acknowledge my parents and brother for their unwavering support and belief in me. Your faith in my abilities has been a constant reminder to keep pushing forward, even when faced with challenges.

Abstract

This research investigates the mechanical properties and microstructural characteristics of Inconel 718 specimens fabricated using different additive manufacturing (AM) systems, focusing on the influence of build orientation. A total of 16 samples were constructed at 45, 60, and 90 degrees to the build platform and analyzed to ascertain variations in mechanical strength, encompassing elongation at break, ultimate tensile strength (UTS), yield stress, and hardness. The comprehensive statistical analysis employs robust methods to quantify the effects of printing parameters on the performance of the builds, thereby identifying the most influential factors in AM processes. Additionally, microstructural analysis through advanced imaging techniques, coupled with fractography, provides insight into the material behavior and failure modes. The results of this study contribute to a deeper understanding of the process-structure-property relationships in AM and pave the way for optimized manufacturing strategies for Inconel 718 and similar superalloys in industrial applications.

Table of Contents

Dedication.....	iii
Acknowledgements.....	v
Abstract.....	vi
Table of Contents.....	vii
List of Tables	x
List of Figures.....	xii
Chapter 1: Literature Review of Metal AM.....	1
1.1 Additive Manufacturing.....	1
1.2 Challenges and Considerations of AM Technology	4
1.2.1 <i>Quality Control</i>	5
1.2.2 <i>Material Limitations</i>	6
1.2.3 <i>Metal AM Cost</i>	6
1.2.4 <i>Size Limitations</i>	7
1.3 Introduction to Powder Bed Fusion Technology.....	8
1.3.1 <i>Electron Beam Melting</i>	9
1.3.2 <i>Laser Powder Bed Fusion</i>	13
1.4 Defects in Additively Manufactured Parts.....	16
1.4.1 <i>Porosity Formation</i>	16
1.4.1.1 Gas Porosity.....	17
1.4.1.2 Lack of Fusion Porosity.....	18
1.4.1.3 Keyhole Formation	20
1.4.2 <i>Crack Formation</i>	21
1.4.3 <i>Laser Spattering</i>	23
1.4.4 <i>Balling Formation</i>	24
1.4.5 <i>Residual Stresses</i>	24
1.4.6 <i>Internal Stresses</i>	25
1.5 Post Processing	25
1.5.1 <i>Powder Removal</i>	26
1.5.2 <i>Stress Relieving</i>	28

1.5.3	<i>Build Plate Removal</i>	29
1.5.4	<i>Support Removal</i>	30
1.5.5	<i>Heat Treatments</i>	30
1.5.6.1	Hot Isostatic Pressing (HIP).....	31
1.5.6.2	Annealing.....	32
1.5.6.3	Aging.....	33
1.5.6.4	Quenching.....	34
1.5.6.5	Tempering.....	34
1.6	Inconel 718.....	35
1.6.1	<i>Applications of Inconel 718</i>	35
1.6.2	<i>Mechanical Properties of Inconel 718</i>	36
1.6.2	<i>Microstructure Phases of Inconel 718</i>	37
Chapter 2:	Materials and Methods.....	39
2.1	Build Plate Description.....	39
2.2	Chemistry of Plates.....	40
2.3	Laser Powder Bed Systems and Parameters.....	45
2.3.2	Laser Scan Strategies.....	46
2.3.3	Recoater Materials.....	47
2.3.4	Build Preparation.....	48
2.4	Heat Treatments.....	48
2.5	Metallographic Preparation.....	49
2.5.1	Fractography Preparation.....	51
2.6	Specimen Testing.....	53
2.7.1	Tensile Testing.....	53
2.7.1.1	Elongation.....	54
2.7.1.2	Ultimate Tensile Stress.....	56
2.7.1.3	Yield Stress.....	56
Chapter 3:	Results and Discussion.....	59
3.1	Specimen Testing Results.....	59
3.1.1	Hardness Testing.....	59
3.1.2	Tensile Testing.....	63
3.1.2.1	Elongation.....	64

3.1.2.2 Ultimate Tensile Stress	66
3.1.2.3 Yield Stress	68
3.1.3 Machine Results.....	70
3.1.4 Angle Results.....	75
3.1.5 Statistical Analysis.....	76
3.1.6 Comparison of Build Nominal Angle to Measured Absolute Angle.....	85
3.1.7 Fractography	86
3.1.8 Metallographic Analysis	97
Chapter 4: Conclusion.....	108
References.....	112
Appendix A.....	131
Appendix B	137
Appendix C	146

Vita 155

List of Tables

Table 1.1: Metal AM machines for fabrication of large products [5].....	8
Table 1.2: Chemical composition of Inconel 718 [71].	36
Table 1.3: Inconel 718 Phase Summary [113].....	38
Table 1.4: Chemistry of plates 1-4.....	41
Table 2.1: Chemistry of plates 5-8.....	42
Table 2.2: Chemistry of plates 9-12.....	43
Table 2.3: Chemistry of plates 13-16.....	44
Table 2.4: Machine overview from shared information of vendor build parameters.	45
Table 2.5: Full heat-treatment (FHT): (SR+HIP+SOL+AGE) for all the samples.....	49
Table 3.1: Plate Hardness Results.....	61
Table 3.2: Machine hardness results.....	62
Table 3.3: Elongation % at Fracture, mm/mm.....	64
Table 3.4: Ultimate Tensile Stress, MPa.....	66
Table 3.5: Yield Stress, 0.2% Offset, MPa.....	68
Table 3.6: Machine's Yield Stress.....	70
Table 3.7: Machine's Elongation at Fracture.....	72
Table 3.8: Machine's Ultimate Tensile Stress	73
Table 3.9: Angle Tensile Results.....	75
Table 3.10: Main Effect Plots for EOS M280	77
Table 3.11: Main Effect Plots for EOS M290	81
Table 3.12: Absolute Angle vs Nominal Angle.....	85
Table 3.13: Average Porosity Size.....	98

Table 3.14: Average Grain Size..... 101

List of Figures

Figure 1.1: The distribution of additive manufacturing (AM) in different sectors [3]	2
Figure 1.2: Comparison of production time between classic processing (CNC milling) and AM (PolyJet process) [4].....	3
Figure 1.3: Metal Additive Manufacturing Market in 2020.[5].....	9
Figure 1.4: Schematic of the electron beam melting (EBM) process [30]	11
Figure 1.5: Schematic of the Laser Powder Bed Fusion (LPBF) process [31].....	13
Figure 1.6: Laser power vs scanning velocity graph – how process outcomes vary with parameter choices.....	17
Figure 1.7: SEM micrographs of (a) gas atomized powders showing gas porosity within the powders (b) cross-section showing gas porosity.....	18
Figure 1.8 (a) Cross-section showing lack of fusion porosity of polished build (b) lack of fusion porosity showing un-melted powder particles.	19
Figure 1.9: Melt pool formation mechanisms a) conduction mode b) keyhole mode c) keyhole with porosity [54].....	20
Figure 1.10: Keyhole Porosity [34].....	21
Figure 1.11: Forms of crack formation: (a, d) triple point cracking, (b) grain boundary cracking, (c) tearing at the grain [83].	22
Figure 1.12: Schematic of the correlation between the depression zone and the backward-ejected spatter in LPBF [85].....	23
Figure 1.13: Microscopic image of Balling [88].....	24
Figure 1.14: Powder removal [91].....	27
Figure 1.15: Schematic of a hot isostatic pressing setup [101].....	32

Figure 1.16: shows the specific strength of high-performance materials [70].....	37
Figure 2.1: L-PBF additively manufactured Inconel 718 feature build plate artifact sample.	39
Figure 2.2: Schematic diagram of line scanning strategy [127].	46
Figure 2.3: Schematic diagram of checkered scanning strategy [127].	47
Figure 2.4: Sectioning of angled wall parts	49
Figure 2.5: Fusion CAD of tensile sample layout.....	50
Figure 2.6: Mounted tensile samples.	50
Figure 2.7: Tensile sample holder for SEM imaging (YZ).....	53
Figure 2.8: Schematic View of Tensile Test [120].....	54
Figure 2.9: Ductile vs Brittle Material Stress- Strain Curve [130].	57
Figure 2.10: Typical stress-strain curve and shape deformation of the specimen from start to fracture. [122].....	58
Figure 3.1: Vickers hardness measurement scheme.	59
Figure 3.2: Plate 7 (a) 45 degree build (b) 60 degree build (c) 90 degree build.....	86
Figure 3.3: Plate 9 (a) 45 degree build (b) 60 degree build (c) 90 degree build.....	88
Figure 3.4: Plate 10 (a) 45 degree build (b) 60 degree build (c) 90 degree build.....	90
Figure 3.5: Plate 11 (a) 45-degree build (b) 60-degree build (c) 90-degree build.....	92
Figure 3.6: Plate 15 (a) 45 degree build (b) 60 degree build (c) 90 degree build.....	95
Figure 3.7: Plate 9 polished and porosity analysis (a) 45° (b) 60° (c) 90°	98
Figure 3.8: Plate 9 microstructures, (a) 45° sample at 200 μm (b) 60° sample at 200 μm (c) 90° sample at 200 μm (d) 45° sample at 50 μm (e) 60° sample at 50 μm (f) 60° sample at 50 μm..	100
Figure 3.9: Grain Morphology View	103

Figure 3.10: Inverse pole figure (IPF) colour mappings and the corresponded IPFs of (a) vertically built and (b) horizontally built as-manufactured sample [138]. 104

Figure 3.11: a) schematic illustration of L-PBF process showing overlap of melt pools and remelting of previously deposited layers, b-d) deconvolution of melting and mixing process used in the model [136]. 105

Figure 3.12: As built plate (a) 45° sample at 200 μm (b) 60° sample at 200 μm (c) 90° sample at 200 μm (d) 45° sample at 50 μm (e) 60° sample at 50 μm (f) 60° sample at 50 μm 106

Chapter 1: Literature Review of Metal AM

1.1 ADDITIVE MANUFACTURING

Additive Manufacturing (AM), an innovative technical frontier, has revolutionized the fundamental nature of contemporary industry. This thesis undertakes a complete exploration of additive manufacturing, encompassing its fundamental nature, many applications, the seven various AM technologies, and the complicated process from Computer-Aided Design (CAD) to the physical manifestation of new products. Additive Manufacturing, often known as 3D printing, is a groundbreaking technological advancement in the field of manufacturing. It provides an exceptional level of design freedom and enables the creation of intricate components with remarkable accuracy.

Additive Manufacturing, in its essence, is a paradigm shift that diverges significantly from conventional subtractive manufacturing methods. Rather than employing traditional methods such as carving, drilling, or cutting to remove material from a solid block, Additive Manufacturing functions by constructing three-dimensional things through the gradual accumulation of material layers. The method of constructing layer by layer not only reduces material waste but also opens new possibilities for design innovation and the efficient creation of prototypes. The outcome is a procedure that enables engineers, designers, and producers to actualize their creative concepts, whether it be through the production of aeronautical components [1], construction [2] or complicated medical implants [3].

Analysing the application market for 3D printing

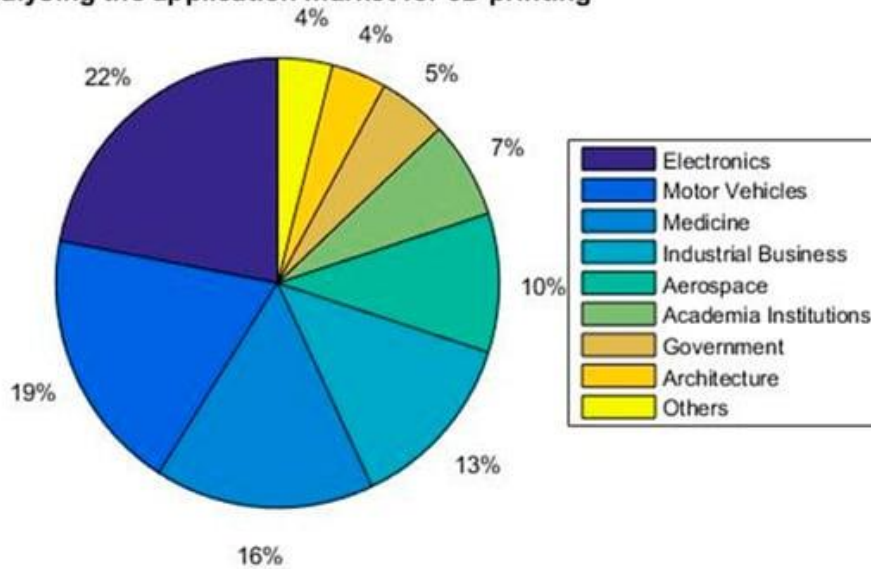


Figure 1.1: The distribution of additive manufacturing (AM) in different sectors [3]

Additive manufacturing, commonly known as 3D printing, expedites the process of quick prototyping and design revisions. Moreover, it has exceptional capabilities in fabricating intricate geometries while maintaining optimal efficiency. Its unparalleled ability to customize and produce on-demand makes it a powerful competitor to the time-consuming and tool-dependent procedures of injection molding and CNC machining.

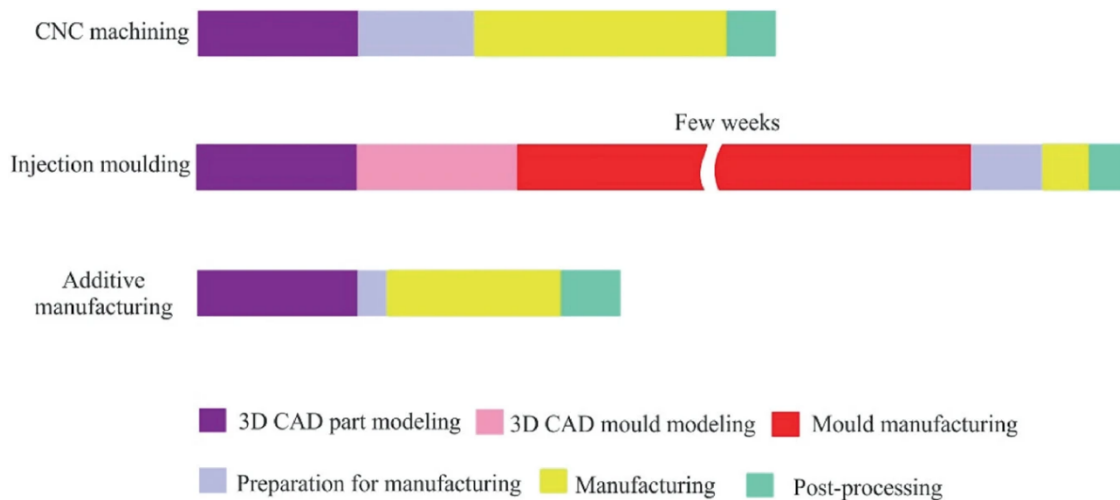


Figure 1.2: Comparison of production time between classic processing (CNC milling) and AM (PolyJet process) [4]

The usefulness of additive manufacturing extends beyond traditional limitations, reaching several sectors. Additive manufacturing (AM) has revolutionized several industries, such as aerospace and healthcare, by enabling the production of lightweight and durable components and the customization of implants for specific patients. This technology has opened up new avenues for innovation and advancement in these sectors. The automobile sector uses additive manufacturing (AM) for the purpose of quick prototyping and the production of intricate components, whereas architects adopt this technology to materialize innovative and cutting-edge buildings. The possibilities of additive manufacturing (AM) have also revitalized the defense and art sectors. Undoubtedly, this technology exhibits remarkable versatility and has the capacity to bring about significant transformations.

In order to have a comprehensive understanding of additive manufacturing (AM), it is necessary to explore the seven unique technologies associated with it. These technologies include Fused Deposition Modeling (FDM), Stereolithography (SLA), Selective Laser Sintering (SLS), Powder Bed Fusion (PBF), Material Jetting, Binder Jetting, and Directed Energy Deposition (DED). Each of these technologies have distinct properties, materials, and applications, rendering them an essential element of the additive manufacturing (AM) domain. The mentioned manufacturing methods have the capability to utilize a diverse range of materials, including polymers, ceramics, and metals. Metallic materials have garnered significant attention from both researchers and companies.

The process of transforming a digital 3D model generated by Computer-Aided Design (CAD) software into a physical product produced through Additive Manufacturing is a

multifaceted and carefully coordinated undertaking. The process involves dividing the digital model into many two-dimensional layers, with each layer serving as a blueprint for the succeeding phases in the manufacturing process. Thin layers of material, often in the form of powder or liquid resin, are deposited and then fused or solidified by the additive manufacturing machine, which is directed by the digital model. The material undergoes a long process of formation, whereby each layer is meticulously included, culminating in the eventual realization of the completed product.

Additive manufacturing methods have the capability to utilize a diverse range of materials, including polymers, ceramics, and metals. Metallic materials have garnered significant attention from both researchers and companies.

1.2 CHALLENGES AND CONSIDERATIONS OF AM TECHNOLOGY

The emergence of Additive Manufacturing technology presents both opportunities and obstacles. The successful integration of additive manufacturing in industry necessitates not only acknowledging its advantages but also addressing the obstacles that hinder its extensive use. This section primarily addresses the fundamental issues associated with the utilization of metal additive manufacturing technology.

Additive manufacturing has several benefits, including the ability to achieve design flexibility, expedite prototype processes, and fabricate intricate geometries. However, there are other factors that need to be taken into consideration, such as quality control, material restrictions, post-processing techniques, cost implications, size constraints, and the requirement for training. It is imperative to effectively tackle these problems in order to fully harness the promise of metal additive manufacturing.

1.2.1 Quality Control

The accuracy requirements in production environments for end-use metal additive manufacturing are significantly greater compared to those in prototype applications. Qualification is a crucial factor that significantly impacts the performance and outcomes within a manufacturing environment. This encompasses the evaluation of the qualifications of additive manufacturing equipment, materials, and personnel, as well as the implementation of quality control methodologies and instruments. Ensuring the precision and consistency of the fabricated goods is crucial throughout the entirety of the printing process, including within individual prints, across successive prints, and between various printer models [6]. The accuracy requirements in production environments for end-use metal additive manufacturing are significantly greater compared to those in prototype applications. Qualification is a crucial factor that significantly impacts the performance and outcomes within a manufacturing environment. This encompasses the evaluation of the qualifications of additive manufacturing equipment, materials, and personnel, as well as the implementation of quality control methodologies and instruments. Ensuring the precision and consistency of the fabricated goods is crucial throughout the entirety of the printing process, including within individual prints, across successive prints, and between various printer models [6,7].

Although metal additive manufacturing has significant advantages during the design phase, it is hindered by a lack of accuracy resulting from fluctuations in mechanical characteristics and distorted part geometry [8]. Several studies have indicated that metal additive manufacturing products exhibit characteristics of anisotropy and heterogeneity in terms of microstructure and mechanical properties [8,9]. It is evident that the material characteristics undergo alterations

subsequent to manufacture, and the behavior of the material is subject to modification when subjected to cyclic thermal loading circumstances [10].

1.2.2 Material Limitations

The field of metal additive manufacturing is demonstrating promising prospects for expansion. The quantity of enterprises engaged in the sale of additive manufacturing systems had a notable increase from 49 in 2014 to 97 in 2016. This growth was observed among the subset of organizations specifically interested in metal AM, constituting around 49% of the total [11].

The quantity of materials available for metal additive manufacturing technologies is on the rise; yet the existing inventory of metals and alloys deemed acceptable for AM remains restricted. In contemporary design practices, designers have the ability to choose from a diverse array of metallic materials, including but not limited to Stainless Steel, Gold, Silver, Inconel, Copper, Titanium alloys, Nickel-based superalloys, tool steels, Aluminum alloys, Platinum, Palladium, and Tantalum [12]. The expansion of materials and the wider use of existing metal additive manufacturing processes are ongoing areas of research and development, driven by the limited quantity of metal materials available for AM systems. Currently, there exists a wide range of material categories, encompassing metals, alloys, ceramics, bioactive glass, polymers, and their respective mixtures.[13]

1.2.3 Metal AM Cost

The evaluation of costs in metal Additive Manufacturing plays a pivotal role in the acceptance and deployment of this technology. Metal additive manufacturing, although its high level of innovation and other advantageous features, nevertheless poses distinctive economic issues that need meticulous management [19]

The selection of metal powders employed in metal additive manufacturing exerts a substantial influence on the total cost. The cost of high-quality powders can be rather high, and the pricing of different materials may exhibit variability. The generation of material waste and the necessity of post-processing procedures might also contribute to the overall expenses associated with materials [19,20]. Numerous metal additive manufacturing components need further processing measures to get the intended surface quality, precision, and mechanical characteristics. Post-processing procedures have the potential to contribute to both temporal and financial expenditures, encompassing factors such as workforce, machinery, and consumable resources [22].

1.2.4 Size Limitations

One of the primary obstacles impeding the use of metal additive manufacturing is the limitation imposed by the maximum build volume, which dictates the largest dimensions achievable for the printed component. Metal additive manufacturing technologies may be categorized into many sub-processes, including Directed Energy Deposition (DED), Electron Beam Melting (EBEAM), among others. However, it should be noted that not all AM systems are capable of effectively creating big parts [23]. Across industry, producers of metal additive manufacturing are consistently developing innovative technologies in order to maintain competitiveness and address the obstacles associated with widespread adoption in industrial settings. Table 1 presents a compilation of contemporary metal additive manufacturing systems that are now accessible in the commercial market for the purpose of fabricating sizable components. It is worth mentioning that the utilization of DED processes is mostly focused on repair applications rather than the manufacturing of complete parts. This is mainly attributed to the

poorer accuracy and minimal feature size of DED processes, which necessitate additional post-processing treatments [24].

Table 1.1: Metal AM machines for fabrication of large products [5]

Machine Name	Manufacturer	Technology Type ¹	Build Size (mm × mm × mm)
Kinetic Fusion	Titomic	DED	9000 × 3000 × 1500
EBAM 300 Series	Sciaky	EBAM	6096 × 1194 × 1524
SonicLayer 7000	Fabrisonic	SL (UAM)	1828 × 1828 × 914
AddCreator	ADIRA	SLM	1000 × 1000 × 500
Lens 850-R	Optomec	LENS	900 × 1500 × 900
MX-1000	InssTek	DED (LMD)	1000 × 800 × 650
ExOne M-Print	ExOne	MJ	800 × 500 × 400
LUMEX Avance-60	Matsuura	SLM	600 × 600 × 500
SLM 500 H	SLM Solutions	SLM	500 × 280 × 365
RMP1	Aurora Labs	DMLM	450 × 450 × 400
MetalFAB1	Additive Industries	SLM	420 × 420 × 400
M400	EOS	DMLS	400 × 400 × 400
Arcam Q20	Arcam	EBM	350 × 380 × 180
LightSPEE3D	SPEE3D	DED (supersonic 3D deposition)	300 × 300 × 300
PAM Series M	Pollen AM	FDM	300 × 300 × 300
Metal X	Markforged	ME	250 × 220 × 200

1.3 INTRODUCTION TO POWDER BED FUSION TECHNOLOGY

Powder Bed Fusion (PBF) is considered one of the oldest and most flexible additive manufacturing techniques. It demonstrates excellent compatibility with polymers and metals, while also exhibiting some capability with ceramics and composites, albeit to a lower degree. The proliferation of machine variations designed for the purpose of fusing powders through the

utilization of diverse energy sources is on the rise. The domain seeing the highest level of development is focused on metal powder bed fusion techniques employing laser technology. Powder Bed Fusion techniques have garnered significant attention in several sectors due to its potential as a direct production method [25].

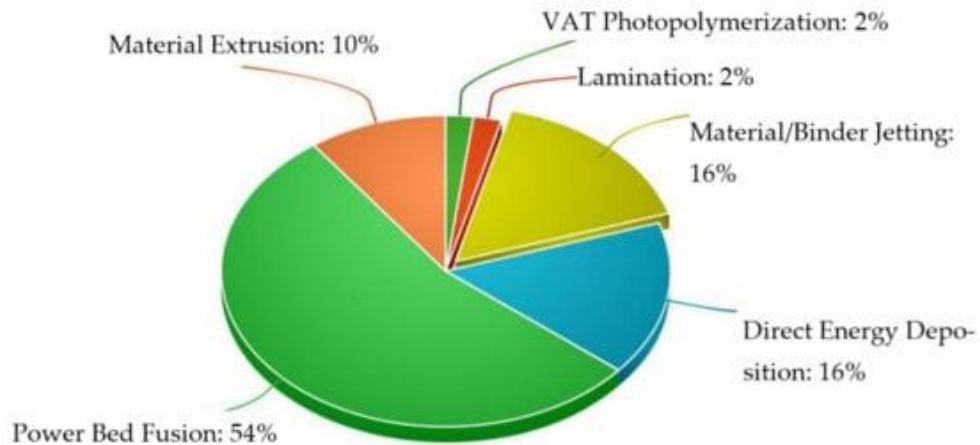


Figure 1.3: Metal Additive Manufacturing Market in 2020.[5]

The powder bed fusion method encompasses two primary printing techniques: electron beam melting (EBM) and Laser Powder Bed Fusion (LPBF). This technique employs either an electron beam or laser to induce the melting or fusion of the constituent powder material. The materials employed in this technique encompass metals, ceramics, polymers, composites, and hybrids [26, 27].

1.3.1 Electron Beam Melting

Electron Beam Melting (EBM) is a unique additive manufacturing process that operates based on its own set of principles and mechanisms. One distinguishing characteristic of EBM is the employment of an electron beam as the primary energy source for the purpose of selectively melting and fusing metal powders. This innovative technique enables the fabrication of highly

complex three-dimensional structures with precision and intricacy. The process is characterized by a sequence of synchronized mechanisms. For optimal performance of the Electron Beam Melting systems, it is recommended to utilize powders that possess a particle distribution ranging from 45 to 105 μm . The powder's morphology must have a spherical shape, exhibit excellent flowability, demonstrate high packing density, and be devoid of any internal porosity [65]. Its basic method of operation is schematically shown in Figure 1.4.

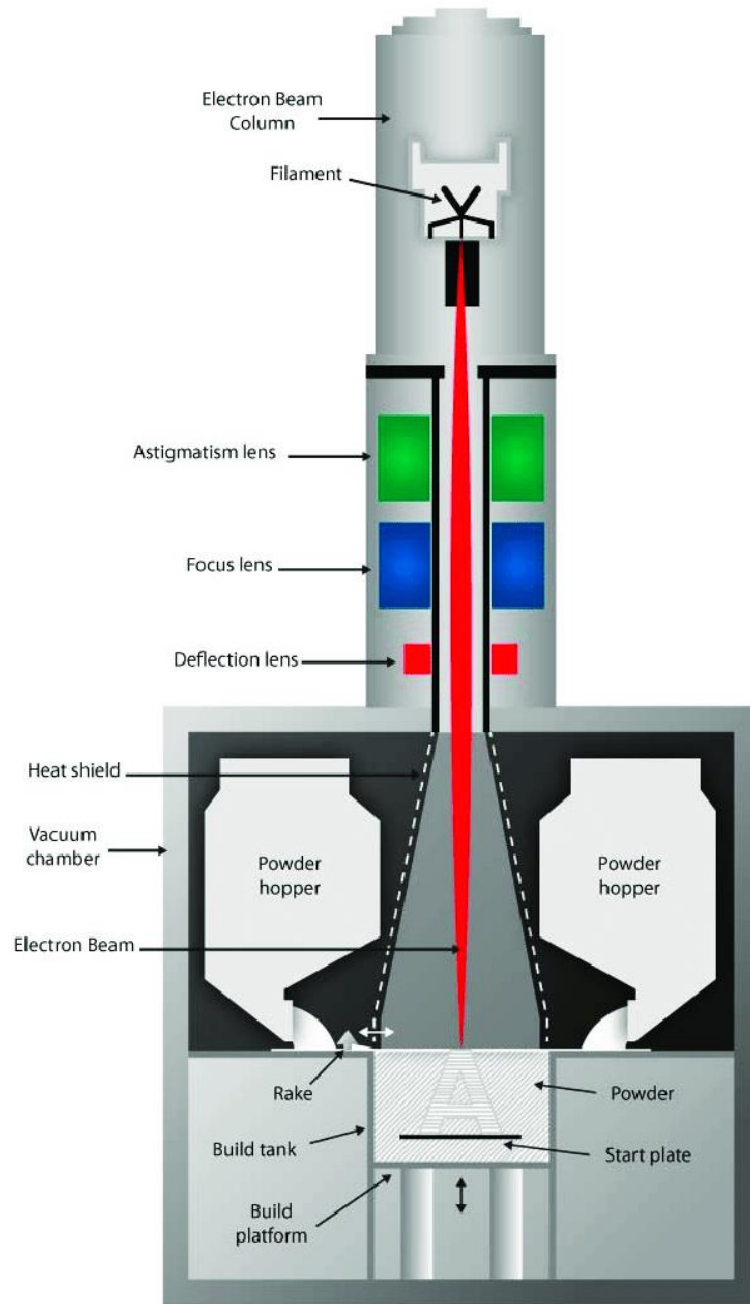


Figure 1.4: Schematic of the electron beam melting (EBM) process [30]

The fundamental process of Electron Beam Melting commences with the creation and precise regulation of the Electron Beam. The electron beam with high energy is effectively controlled by the software of the system, and it assumes a crucial function in the fusion process of

metal powders [61]. In contrast to several additive manufacturing methods, Electron Beam Melting operates under a vacuum environment, which establishes a high or nearly complete absence of air pressure [30]. This controlled setting effectively safeguards against the introduction of impurities and the oxidation of metal particles during the melting procedure.

The method known as "Powder Dispensing and Layer Formation" entails the uniform dispersion of a fine layer of metallic powder on the build platform, often with a thickness of less than 100 microns [60]. Subsequently, the electron beam proceeds to scan the powder layer, employing a discerning approach to selectively induce melting of particles in accordance with the instructions provided by the digital model [63]. This process culminates in the formation of a cohesive and compact layer [62]. The technique involves the utilization of an electron beam to selectively heat and merge metal powder particles, resulting in the formation of a solid layer that exhibits high density and a reduced presence of voids [59].

The Platform Lowering function, analogous to Laser Powder Bed Fusion, facilitates the downward displacement of the build platform subsequent to the finalization of each layer, hence creating space for the subsequent application of the subsequent layer of metal powder [64]. The iterative process persists until the complete component is entirely fabricated. EBM has notable material compatibility with high-temperature materials, particularly titanium and certain nickel-based superalloys. Consequently, it is well-suited for applications that demand robustness and resilience in the face of extreme temperatures. The remarkable characteristic of the technology is in its capacity to manufacture extensive and intricate components, particularly in sectors such as aerospace, where the production of aircraft frames and engine parts necessitates significant dimensions.

Nevertheless, the employment of Electron Beam Melting has the potential to generate residual Stress inside components, hence requiring further heat treatment to alleviate stress and achieve the necessary mechanical characteristics [58]. Furthermore, similar to several additive manufacturing methods, items generated using electron beam melting may need post-processing procedures, such as surface polishing, in order to get the intended surface quality.

1.3.2 Laser Powder Bed Fusion

PBF processes were among the first commercialized AM processes. The method known as Selective Laser Sintering (SLS) was created by Carl Deckard in the year 1987 at the University of Texas at Austin, USA. The SLS technique is a form of 3D printing that exhibits notable attributes such as rapid speed, superior precision, and the ability to achieve diverse surface finishes [26, 27].

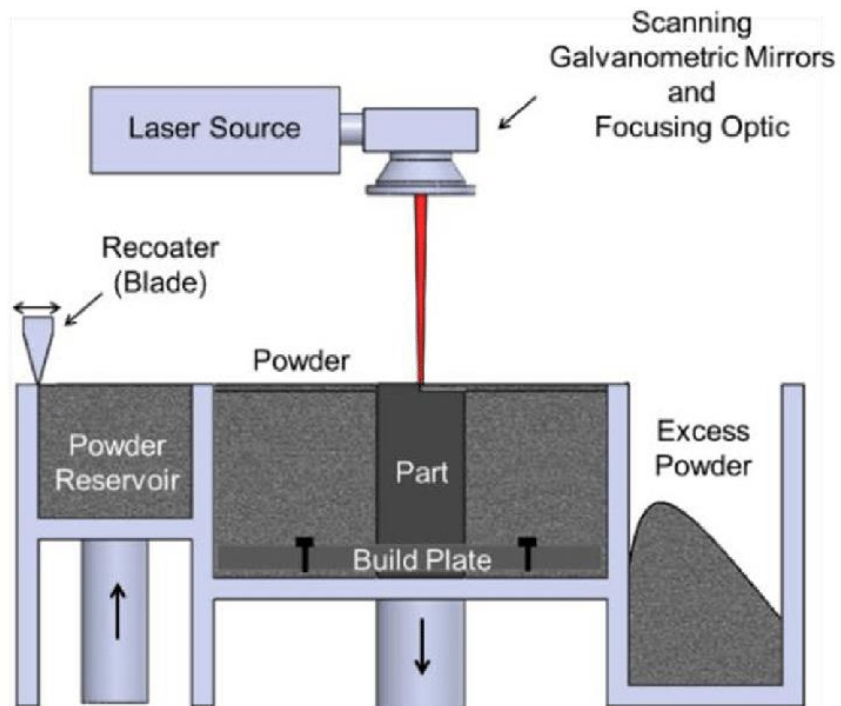


Figure 1.5: Schematic of the Laser Powder Bed Fusion (LPBF) process [31]

Laser Powder Bed Fusion (LPBF) is an influential additive manufacturing technique that stands out due to its ability to fabricate intricate and precise three-dimensional items [29]. The process relies on a set of interconnected mechanisms, with each mechanism playing a role in the creation of final components. For LPBF powders, it is recommended to use powders with 15–45 μm [66]. The desired powder morphology typically consists of particles that are predominantly spherical or nearly spherical in shape, exhibiting a uniform size distribution. Spheroidal powder particles facilitate consistent powder dispersion and efficient energy absorption during the fusion process, leading to the production of superior, compact components.

The Laser Powder Bed Fusion process commences with the Powder Dispensing and Spreading mechanism [67]. A relatively thin deposition of metal powder, generally measuring less than 100 microns in thickness, is evenly distributed throughout the build platform. The achievement of an equal distribution is aided by the implementation of a recoating mechanism, which serves to guarantee an optimal substrate for the additive process.

The third stage involves Layer-by-Layer Digital Scanning. The process starts by utilizing a three-dimensional digital representation of the desired component, which is then divided into cross-sectional layers with a typical thickness ranging from 20 to 100 microns at different laser power and speed combinations [68]. They found layer thickness to be the major influencing factor for melt pool height and a minor influencing factor for melt pool depth, width, and mode, with melt pool mode determining the mechanical properties of parts [28]. The laser with high power is thereafter accurately guided to perform a scanning process on every layer, according to the precise outlines outlined in the digital design.

The fundamental principle of the LPBF method is centered around the Laser Melting mechanism. The system's software painstakingly regulates the operation of a high-power laser,

which is often a fiber laser or a CO2 laser. The process is concentrated on certain regions of the metal powder bed, providing the necessary energy to raise the powder particles to their melting temperature.

The method known as Selective Fusion is employed, whereby the metal powder particles are melted and fused in a targeted manner using a laser, in accordance with the instructions provided by the digital model. The process of fusion results in the formation of a solid layer that exhibits a high density and low presence of voids. These characteristics are attributed to the confined melting and subsequent quick solidification.

The implementation of platform lowering is a crucial aspect of LPBF technology. As the construction of each layer is finalized, the build platform undergoes a steady descent equivalent to the thickness of a solitary layer. The presence of this clearance enables the subsequent deposition of the succeeding layer of metal powder, and this iterative procedure continues until the entire component is completely fabricated.

The LPBF process occurs in a controlled environment, typically with the use of inert gases such as argon or nitrogen. The utilization of an inert gas environment is employed to mitigate metal oxidation in the context of high-temperature processes, hence ensuring the preservation of the ultimate product's quality.

The processes of cooling and solidification occur immediately after localized fusion. The molten metal rapidly undergoes solidification as the laser transitions to the subsequent predetermined region. The process of quick solidification plays a crucial role in attaining refined microstructures and high-density components, hence enhancing the longevity and excellence of the end product.

In situations where it is deemed necessary, LPBF has the potential to include Support Structures. Temporary scaffolds are implemented in order to mitigate the risk of warping or collapse that may occur during the adding process. The generation of these artifacts is often automated by the program and then eliminated at the post-processing stage.

The concluding stage of LPBF is referred to as "post-processing". During this phase, the printed component may undergo supplementary procedures, including heat treatment, surface refinement, and the elimination of support structures. The implementation of these post-processing procedures is essential for attaining the intended standards and ensuring a high level of surface quality [69].

1.4 DEFECTS IN ADDITIVELY MANUFACTURED PARTS

Fusion-based additive manufacturing techniques, such as laser powder bed fusion, employ a heat source, often a laser, to facilitate the fusing of materials. The underlying principles governing this process revolve around the concepts of melting and solidification [32]. The problems seen in the additive manufacturing (AM) process include the presence of pores, cracks, lack of fusion, keyhole formation, laser spattering, balling, poor surface roughness, residual stresses, internal stresses and form distortion [33, 34]. The additive manufacturing (AM) process can be influenced by several underlying factors that contribute to the generation of inaccuracies.

1.4.1 Porosity Formation

Porosity in parts produced via additive manufacturing can be categorized into distinct types: gas porosity lack-of-fusion (LOF) porosity and keyholes [37,38]. A pore within a component can serve as a point of failure initiation, and it is ideal to minimize porosity in a manufactured part.

The central operating window, as depicted on the P-V diagram, Figure 1.6, is the region where the appropriate balance between velocity and power results in the formation of a stable molten pool with the most favorable dimensions [50]. The laser energy is effectively absorbed by the powder, resulting in the formation of a melt pool that achieves a suitable depth for strong fusion with the underlying layer, while minimizing excessive re-melting. Fluctuations in laser temperature, whether exceeding the optimal range or falling below it, can give rise to complications such as lack of fusion or instability in the keyhole during manufacturing operations [51].

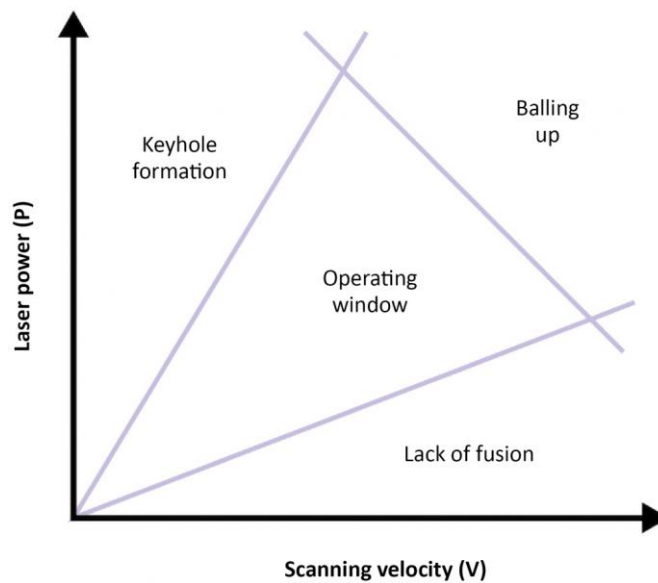


Figure 1.6: Laser power vs scanning velocity graph – how process outcomes vary with parameter choices.

1.4.1.1 Gas Porosity

Gas porosity in builds is typically caused by the presence of trapped gases within the metal powder or in the build environment. During the manufacturing process, when the high-power laser selectively melts and fuses the metal powder, any trapped gases can become released and create voids within the part [53]. This porosity is a result of the entrapment of gas within the molten metal

during its rapid solidification process [9]. The gaseous substance can arise from either the internal regions of the powder particles, related to their porosity or as a result of being introduced during the atomization procedure, or from the surrounding environment encompassing said particles [9, 52].

Trapped gases can compromise the mechanical properties of the final part, reducing its integrity and performance. Effective strategies to mitigate gas porosity include using controlled atmospheres (such as inert gases like argon) in the build chamber, optimizing powder quality, and ensuring proper degassing procedures [52].

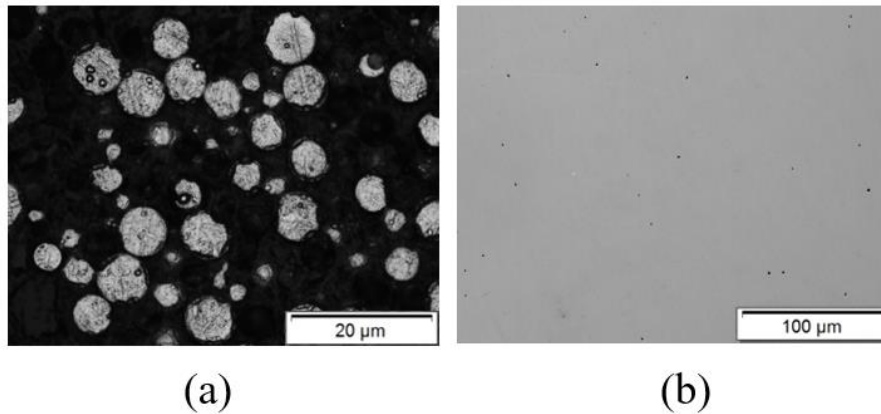


Figure 1.7: SEM micrographs of (a) gas atomized powders showing gas porosity within the powders (b) cross-section showing gas porosity.

1.4.1.2 Lack of Fusion Porosity

Lack of fusion pores arise due to an inadequate supply of energy input to the powder bed during the melting phase. Insufficient input energy or inappropriate scan speeds results in incomplete melting of the metal powder, leading to the formation of voids within the resulting structure. The presence of lack of fusion pores is commonly observed in dimensions that are comparable to the size of the molten pool, exhibiting irregular characteristics [38].

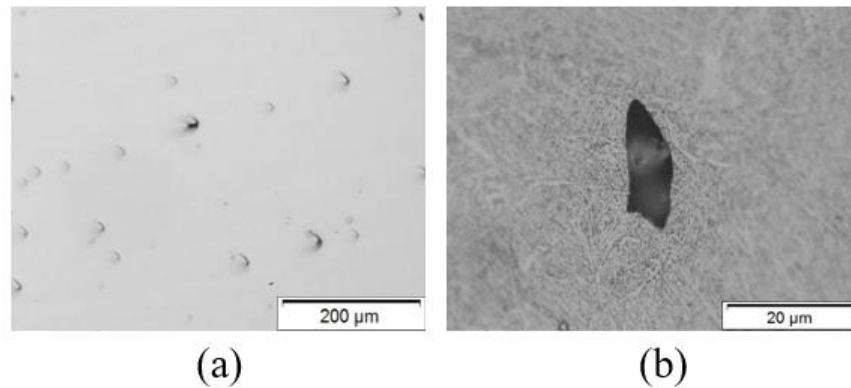


Figure 1.8 (a) Cross-section showing lack of fusion porosity of polished build (b) lack of fusion porosity showing un-melted powder particles.

Recoating, a crucial process that holds significant impact over the development of lack of fusion defects [55]. In the event that the recoating mechanism fails to operate at peak efficiency, it may give rise to a multitude of obstacles culminating in inadequate fusion. The issue of uneven or inconsistent powder distribution is a significant matter of concern. Areas with differing powder thicknesses may appear if the recoating procedure is unable to provide a consistently thick layer of metal powder with each fresh pass [56]. The observed discrepancy has a direct impact on the energy absorption during subsequent laser iterations, thereby introducing the possibility of inadequate melting and fusion. Furthermore, the recoating procedure may inadvertently induce particle segregation within the powder bed, resulting in the uneven distribution of smaller and larger particles [57]. The previously mentioned occurrence has the potential to cause disturbances in the transmission of energy from the laser, consequently leading to the formation of regions exhibiting defects in fusion [55]. The implementation of appropriate equipment maintenance, calibration, and quality control measures is imperative in order to uphold the functionality of a recoating system, guarantee uniform and accurate powder dispersion, and minimize the influence of recoating-related variables on the quality of additive manufacturing builds.

1.4.1.3 Keyhole Formation

The occurrence of keyhole pores can be attributed to an excessive influx of input energy during the melting phase. The surplus of beam power results in an overabundance of metal powder penetration, leading to the formation of a pore in close proximity to the lower region of the molten pool upon solidification [40]. The outcome is a comparatively sizable aperture that typically exhibits a circular shape in the horizontal plane and an elongated configuration in the vertical axis. Keyhole pores may exhibit a top width greater than their bottom width, resembling the shape of a keyhole [38].

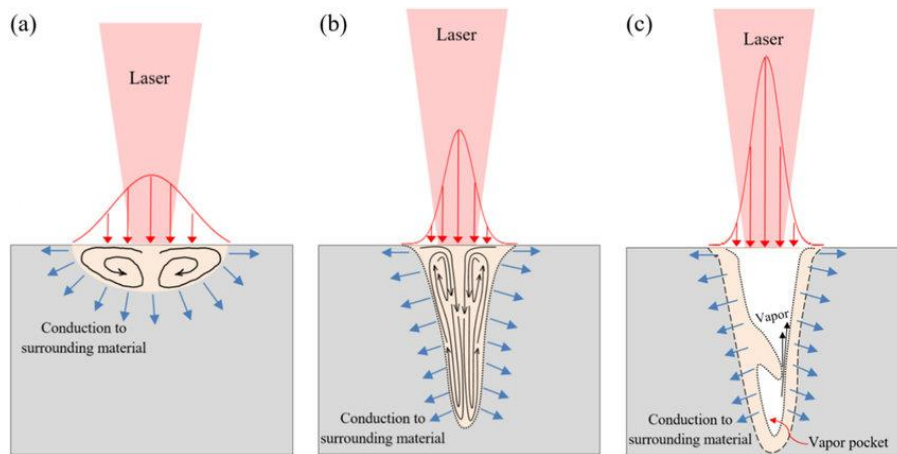


Figure 1.9: Melt pool formation mechanisms a) conduction mode b) keyhole mode c) keyhole with porosity [54].

Upon the traversal of the laser beam, the keyhole will undergo a collapse, thereby facilitating the subsequent flow of molten metal into the designated cavity. Due to the phenomenon of solidification commencing from the lowermost region of the melt-pool, it is frequently observed that an ample duration is available for any entrapped vapor situated near the uppermost region of the melt-pool to ascend and disperse prior to solidification taking place. However, it is important to note that this scenario may not hold true for vapor that becomes trapped in the lowermost region

of the melt-pool. In such instances, the outcome is the formation of sizable, generally spherical voids within the solidified melt-pool, which are commonly referred to as keyhole pores [34].

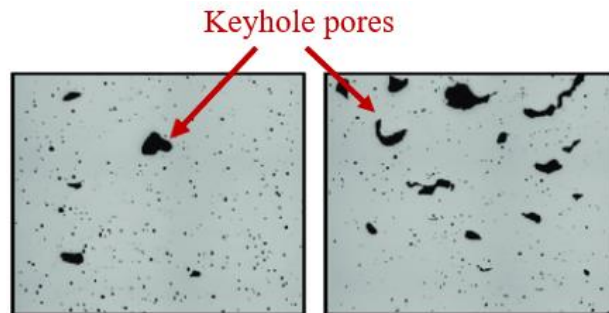


Figure 1.10: Keyhole Porosity [34]

1.4.2 Crack Formation

When it comes to metal additive manufacturing, crack formation is the term used to describe the development of cracks or fissures inside printed components, which can negatively impact the mechanical characteristics and structural integrity of the manufactured parts [78]. Usually, a number of inherent AM process variables result in the formation of these cracks. Thermal gradients, or abrupt cycles of heating and cooling, can produce localized overheating and thermal stress, which can result in microstructural alterations and the start of fractures [79]. Particularly in complicated geometries, residual stresses from the solidification and cooling of each layer can potentially lead to the production of cracks [80]. If not correctly planned or implemented, inadequate support structures—which are crucial for preserving the shape and avoiding deformation of overhanging features—can result in heat distortion and cracking. Furthermore, the printed material's vulnerability to cracking can be influenced by material attributes such as composition and powder shape [81, 82]. The quality and dependability of the produced components are jeopardized by the problem of fracture development in metal AM. A

part's ability to withstand loads, function better overall, and become more prone to early failure are all impacted by cracks in the part's structural integrity [78]. In sectors where the integrity and dependability of produced parts are crucial, including aerospace, healthcare, and automotive, this presents serious difficulties [3].

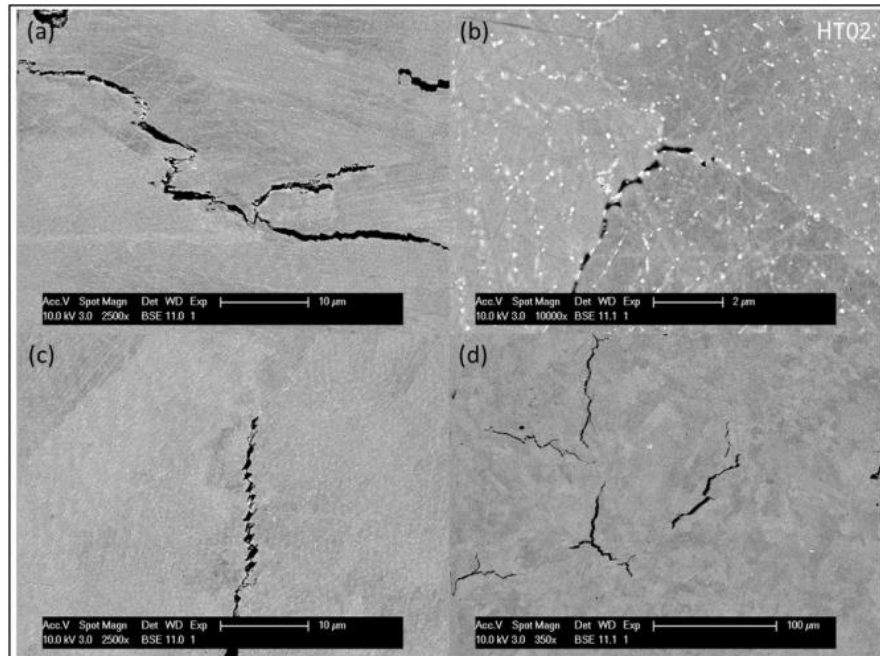


Figure 1.11: Forms of crack formation: (a, d) triple point cracking, (b) grain boundary cracking, (c) tearing at the grain [83].

1.4.3 Laser Spattering

Laser spatter, a frequently observed phenomenon in laser-driven operations, refers to the undesirable expulsion of tiny molten metallic particles from the area [85]. It presents itself as a phenomenon of dispersion that has the potential to impact the integrity and accuracy of laser welding and additive manufacturing processes.

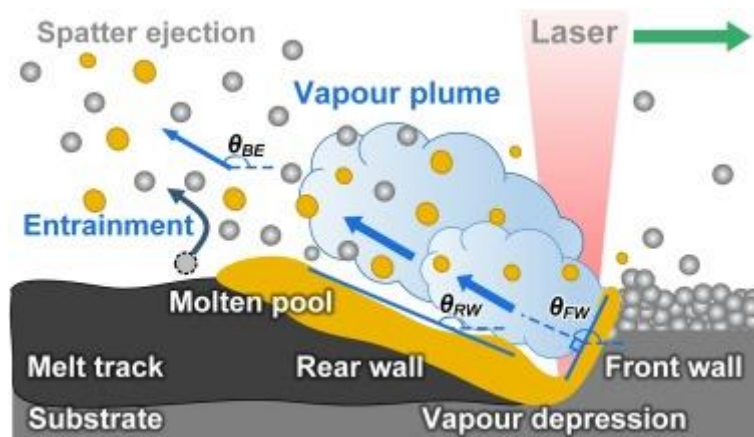


Figure 1.12: Schematic of the correlation between the depression zone and the backward-ejected spatter in LPBF [85].

Laser spatter may arise due to a confluence of factors, encompassing but not limited to, an overabundance of laser power, material characteristics, suboptimal laser focal point, gas atmosphere integrity, and material impurities [86]. The management and reduction of laser spatter is of utmost importance in guaranteeing the dependability and effectiveness of laser-driven manufacturing procedures, thereby facilitating the production of superior components with negligible surface imperfections.

1.4.4 Balling Formation

Balling, a prevalent issue in laser powder bed fusion of metals, is considered a fundamental defect that significantly impacts the performance of 3D printed components. It results in the formation of excessive porosity, thereby compromising the overall quality and functionality of the parts [87]. Balling is characterized by the formation of diminutive, globular metallic droplets during the additive manufacturing procedure, specifically when employing high-energy lasers. These spherical droplets can affect the quality and precision of the printed components. Balling is a phenomenon that arises from the confluence of various factors, including an overabundance of laser energy, the inherent properties of the material, and the distinctive characteristics of the powder [88].

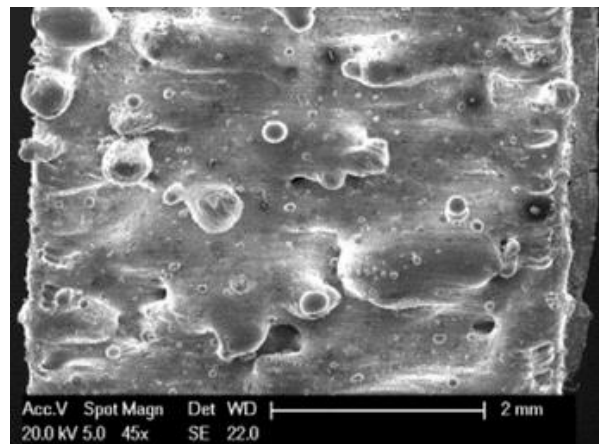


Figure 1.13: Microscopic image of Balling [88].

1.4.5 Residual Stresses

Residual stresses pose a substantial concern in metal additive manufacturing, wherein the intricate interplay among thermal energy, cooling mechanisms, and layer-by-layer deposition creates a dynamic environment [89]. The stresses experienced by 3D-printed metal components are caused by external factors, including rapid changes in temperature, phase transformations, and

thermal gradients occurring during the manufacturing process [35]. These stresses have a significant impact on the structural integrity and performance of the components.

The thermal cycle of metal additive manufacturing exhibits distinctive features: (1) The heating process is accelerated due to the high energy intensity, resulting in steep temperature gradients. (2) The solidification occurs rapidly with high cooling rates, due to the small size of the melt pool. (3) Melt-back occurs, which involves the simultaneous melting of the uppermost powder layer and the re-melting of underlying layers that were previously solidified. The critical concern for fabricated metal parts in additive manufacturing is the presence of residual stress resulting from the distinctive thermal cycle. The steep gradients of residual stress give rise to part distortion, significantly compromising the functionality of the end-use parts [90].

1.4.6 Internal Stresses

The analysis of internal stresses in metal additive manufacturing components is a crucial element of the printing procedure, as it significantly impacts the structural integrity and performance of the manufactured parts. The stresses observed are not exclusively ascribed to external loads, but rather arise from a multitude of intrinsic factors inherent to the material and the additive manufacturing (AM) process.

1.5 POST PROCESSING

Post-processing processes are required subsequent to each print, depending on the specific metal additive manufacturing method employed. The activities encompassed in this context may comprise the removal of powder, stress alleviation, elimination of components and support structures, machining procedures, and the enhancement of part quality through the mitigation or elimination of flaws generated during the printing process, such as lack of fusion and porosity. However, it is important to note that these operations also contribute to an increase in the overall cost of the process [14]. One operation that merits additional consideration among these processes

is the stress relieving operation. This operation is typically necessary for fabricated metal parts produced using most metal additive manufacturing technologies. The reason for this is that the rapid thermal cycles and simultaneous melting of the new layer and re-melting of the previously solidified layers result in residual stresses. The processes encompass a range of techniques employed to mitigate internal flaws, enhance the microstructure, and improve the mechanical characteristics of additive manufacturing components. These operations are deemed essential for the majority of metal AM parts [15].

1.5.1 Powder Removal

The removal of powder is an essential step within the Laser Powder Bed Fusion procedure. This particular step serves a multitude of functions in the manufacturing process of superior metal components [91]. One of its principal functionalities entails the retrieval and recycling of the unmelted metallic powder. In the LPBF process, a portion of the powder is selectively melted and fused to fabricate the component, while the remaining loose powder can be recovered and reintegrated into the system to optimize cost-effectiveness [92]. The reclamation of materials is of utmost importance in the field of mechanical engineering, as the cost of metal powders can be relatively high, and their quality may degrade over time. Through the elimination of loose powder, the procedure facilitates the opportunity for the reutilization of valuable resources, thereby making a significant contribution to the economic feasibility of metal additive manufacturing [94].

Furthermore, the process of powder removal plays a crucial role in guaranteeing the desired surface quality and optimal cleanliness of the printed components. Upon the conclusion of the printing procedure, it is customary for the printed entity to be encased within a layer of unused powder. The removal of this extra powder is necessary in order to reveal the ultimate printed component, free of any lingering particles. This not only optimizes the aesthetic appeal of the part but also simplifies the process of conducting inspections and evaluations on the component's quality.

Additionally, the removal of extra powder from the surface is an essential procedure for carrying out subsequent post-processing tasks. Numerous 3D-printed metallic components require supplementary processing, such as heat treatments or surface finishing, in order to satisfy the prescribed specifications. In order to execute these secondary processes with optimal efficiency, it is of utmost importance that the printed component is easily accessible and free from any unnecessary powder.

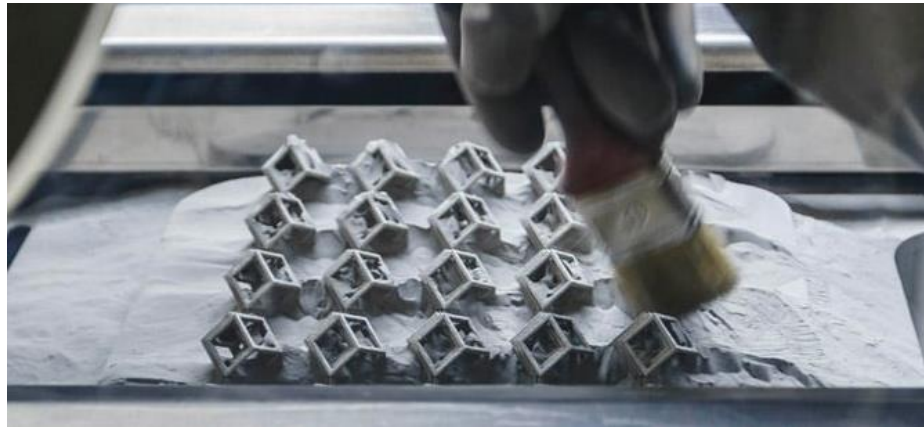


Figure 1.14: Powder removal [91].

Apart from these benefits, safety is also another important factor to take into account while removing powder. The presence of loose metallic powder within the building chamber may give rise to safety concerns, specifically the potential for combustible dust explosions. Reducing these safety issues and preserving a safe working environment for operators are two benefits of the cautious removal of extra powder [93]. The removal of powder can be achieved through a range of methods, such as the manual application of brushes, the forceful expulsion of compressed air, and the employment of dedicated apparatus such as powder recovery systems [94]. The loose powder is carefully gathered, subjected to sieving for the purpose of achieving uniformity, and, in numerous instances, blended with new powder in order to maintain the desired material properties for subsequent printing cycles [92].

1.5.2 Stress Relieving

Stress relieving, a fundamental post-processing procedure within the field of metal additive manufacturing, involves an abundance of crucial factors. The presence of residual stresses within 3D-printed components is a direct result of the rapid heating and cooling cycles that occur during the printing process, which is the fundamental reason for its necessity. If these residual stresses are not addressed, they can result in a multitude of problems, spanning from dimensional instability to degradation of mechanical properties [35]. Stress relieving serves as a corrective action, with the objective of addressing these issues and improving the overall quality and dependability of the manufactured components.

Through the process of stress relieving, the residual stresses are effectively mitigated, thereby playing a crucial role in augmenting the mechanical characteristics of the printed components [35]. The existence of residual stresses may lead to diminished strength, ductility, and fatigue resistance, all of which are vital parameters in assessing the suitability of the printed component for its designated purpose. Stress relieving serves to optimize these properties, thereby enhancing the suitability of the components for enduring mechanical loads and environmental conditions.

Dimensional stability is a crucial aspect of stress relieving, as it ensures the structural integrity and reliability of the system. Residual stresses have the potential to induce form distortions, warping, and deviations from the intended dimensions [36]. The process of stress relieving aids in restoring the part to its designated tolerances and geometric prerequisites, thereby guaranteeing its alignment with the design specifications.

Additionally, the implementation of stress relieving techniques aids in the mitigation of potential cracking occurrences within the printed component [81]. Residual stresses possess the capability to induce microcracks or facilitate the commencement and advancement of cracks, thereby potentially jeopardizing the structural soundness of the build. By subjecting the part to the

stress relieving process, these risks are effectively mitigated, thereby augmenting the part's inherent resistance to crack propagation, and subsequently enhancing its overall durability [83].

Stress relief is usually achieved via a carefully regulated heat treatment procedure. The fundamental stages in this process entail incrementally elevating the temperature of the 3D-printed metallic constituent to a precise degree within a furnace [95]. The temperature and heating rate are precisely regulated to guarantee uniform heating across the component. Upon achieving the target temperature, the component shall be maintained at said level for a certain amount of time. The duration of the holding phase is determined by multiple factors, such as the size of the component, the type of material used, and the magnitude of residual stresses. After the designated holding period, the component undergoes a gradual and consistent cooling process under controlled conditions. The cooling rate is intentionally set to be slower than the rate at which the component was heated [90]. The process attempts to reduce distortions, improve dimensional stability, and enhance the mechanical properties of the build by enabling stress relaxation of the material.

1.5.3 Build Plate Removal

The build plate removal process entails the careful separation of the 3D-printed metallic component from the construction platform on which it was fabricated. The need for the removal of the build plate is emphasized by a multitude of pivotal factors. First, it makes the printed portion accessible, which is safely fused to the build plate throughout the printing procedure. The access in question holds utmost importance for the subsequent post-processing procedures, thorough inspection, and any necessary surface finishing operations.

The mechanical separation procedure is conventionally executed utilizing specialized apparatus, and utmost caution is exercised to prevent any detrimental impact on the printed component. While wire EDM is frequently used to remove parts from the build plate, bandsaws are also commonly utilized in machine shops since they are quicker and component bottoms still need to be finished [96]. Upon successful removal, the part proceeds to undergo additional post-

processing procedures, thereby guaranteeing its readiness for its designated application or subsequent treatments aimed at augmenting its overall quality and performance.

1.5.4 Support Removal

The removal of the support structure is a crucial post-processing procedure in LPBF and other metal additive manufacturing techniques. The necessity for the removal of support structures arises due to the intricate and complex geometries frequently produced utilizing these methods. In the course of the printing process, it is imperative to employ provisional support structures for the purpose of preventing distortion or collapse in the presence of overhanging features, cavities, or fragile structures [99]. The supports are conventionally fabricated utilizing the same material as the component, but at a diminished density, and are tactically engineered to furnish stability throughout the printing process while remaining detachable subsequently. The removal of these supports is of utmost importance in order to gain access to the ultimate printed component, as well as to attain the desired geometry and surface finish. The procedure for support removal generally entails the collaborative use of manual and mechanical techniques, including but not limited to cutting, grinding, or sandblasting [98]. The objective is to carefully disengage the supports while limiting any potential harm to the printed component. The optimization and exactness of support removal play a pivotal role in guaranteeing the operational capability, dimensional precision, and comprehensive excellence of the component, thereby establishing it as an indispensable component of the metal additive manufacturing procedure.

1.5.5 Heat Treatments

Heat treatment involves various processes such as HIP, Annealing, Aging, and Tempering [97]. These processes serve to enhance the microstructure and mechanical characteristics of the components, rendering it an indispensable step for the majority of additive manufacturing parts. In numerous instances, this stage necessitates the utilization of an environmentally regulated

furnace equipped with temperature regulation capabilities and a controlled cool-down schedule. The thermal processing procedure has the potential to influence the dimensional characteristics of the components.

1.5.6.1 Hot Isostatic Pressing (HIP)

Hot Isostatic Pressing (HIP) is an advanced post-processing methodology employed in the field of metal additive manufacturing, specifically devised to improve the overall quality and inherent characteristics of 3D-printed metallic constituents [16]. The procedure initiates by inserting the 3D-printed metallic component into a specifically designed HIP container which guarantees an airtight setting. The canister is subsequently sealed in a tight seal. Following that, the tightly sealed container is strategically placed inside a high-pressure chamber and infused with an inert gas, typically argon. The inert gas performs a dual function: firstly, it applies a substantial amount of pressure on the canister, typically falling within the range of 100 to 2,070 MPa (15,000 to 300,000 psi), and secondly, it guarantees the consistent application of pressure to the component from all orientations [100].

The subsequent stage of the HIP process entails increasing the temperature within the vessel. The temperature is meticulously regulated and upheld below the material's melting point, while also being adequately elevated to facilitate plastic deformation of the metal. Due to the synergistic effects of increased pressure and temperature, the metal powder particles within the 3D-printed component undergo a process of reformation and consolidation [102].

The dwell time, a predetermined duration, is allocated for the purpose of sustaining the designated pressure and temperature. Within this specific time frame, it becomes feasible to execute the extraction of internal voids, the consolidation of particles, and the eradication of residual stresses, thereby facilitating the augmentation of the part's properties [17]. Following this,

the commencement of the cooling phase is imperative, and it is of utmost importance that this particular procedure takes place at a meticulously regulated pace in order to avert the resurgence of any remaining internal strains.

After attaining the designated temperature, the HIP canister is extracted from the vessel, thereby exposing a 3D-printed component that has undergone a substantial metamorphosis. The density has been increased, resulting in enhanced mechanical characteristics and a reduced occurrence of internal voids. HIP is a highly effective technique that effectively eliminates residual stresses in components [102]. This process results in parts that exhibit superior fatigue resistance, enhanced ductility, and overall improved performance [17,18].

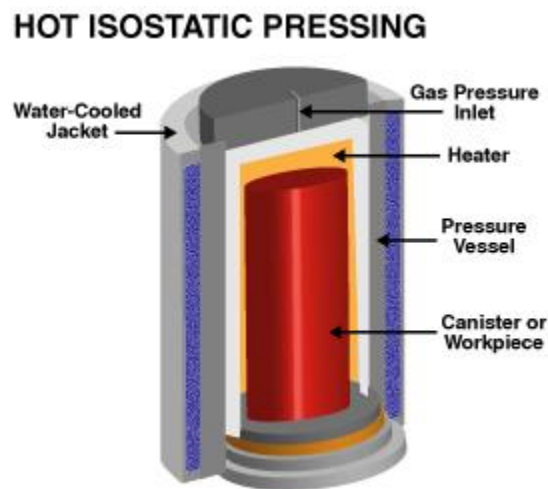


Figure 1.15: Schematic of a hot isostatic pressing setup [101]

1.5.6.2 Annealing

Annealing is a significant procedure that is strategically used to modify the inherent characteristics of a given material, typically resulting in enhanced flexibility, increased ductility, or the reduction of internal stresses [105]. The process entails a series of meticulously regulated procedures, commencing with a gradual application of heat to a precise temperature, determined

from the material's composition and the desired transformations in its properties. The material absorbs thermal energy during heating, which improves atomic or molecular mobility. Heating usually takes place between 300 and 410°C, and heating times vary depending on the size of the workpiece and the type of alloy. The workpiece can take anywhere from 0.5 to 3 hours to complete. The cooling rate of alloys must not exceed 20°C per hour until the temperature reaches 290°C [104]. The subsequent period of holding at the annealing temperature facilitates the achievement of uniformity and stress relief, thereby exerting a profound influence on the ultimate properties. The procedure is finalized through the implementation of regulated cooling, which exerts an influence on the microstructure and material properties. Annealing is a process that effectively mitigates stress, facilitates recrystallization to enhance mechanical properties and minimize defects, and guarantees uniform dispersion of alloying elements or impurities within the material [105].

1.5.6.3 Aging

Aging is intended to improve the mechanical properties of a material, including its toughness, strength, and hardness [106]. There exist two fundamental mechanisms of aging in materials: precipitation hardening and grain boundary strengthening. During the process of precipitation hardening, the material undergoes a series of sequential steps. The process commences with a solution treatment, wherein the material undergoes heating to facilitate the dissolution of alloying elements into a solid solution, thereby enhancing the uniformity of its composition. Following that, the process of rapid quenching effectively induces a rapid decrease in temperature of the material, thereby maintaining the integrity of the supersaturated solid solution. In the course of the aging process, the material undergoes thermal treatment to attain a precise temperature, thereby inducing the precipitation of alloying elements as minute particles within the microstructural framework. The presence of these precipitates acts as an impediment to

the movement of dislocations, consequently enhancing the mechanical strength of the material. The process is finalized through the implementation of controlled cooling, which exerts influence over the size and distribution of the precipitates. Grain boundary strengthening, a technique employed in specific non-ferrous metals, encompasses the alteration of grain boundaries to augment existing material characteristics. The aging processes are diligently customized for specific materials and applications, wherein parameters like temperature, duration, and rate of cooling are precisely regulated to attain the desired properties.

1.5.6.4 Quenching

A crucial heat-treating procedure called quenching involves submerging a hot material—such as a metal or alloy—in a liquid or gas quenching medium in order to quickly cool it down [107]. Controlling the material's microstructure and, hence, its mechanical characteristics, is the main goal of quenching. The material experiences a sharp drop in temperature during the quenching process, which causes the microstructure to solidify quickly. Faster cooling stops bigger, coarser grain structures from forming, which can lead to better mechanical qualities and hardness [108]. The ultimate characteristics of the material are determined by the temperature and time of the quenching process, which makes selection of the quenching medium crucial. Water, oil, and air are common quenching mediums; each has a unique cooling rate and material-specific impact [109]. A crucial stage in the heat treatment of metals, quenching requires precise control in order to provide the required material properties, such as hardness, strength, and toughness.

1.5.6.5 Tempering

Following quenching, usually after a metal or alloy has been hardened, tempering is an important heat treatment procedure. It entails heating an object to a certain, lower temperature and maintaining it there for a specific length of time [110]. Tempering is mostly done to enhance and

change the mechanical characteristics of the material, especially its toughness, strength, and hardness [112]. The material is very hard but brittle upon quenching. This high hardness may be gradually reduced by tempering, increasing the material's durability and reducing its susceptibility to fractures [111]. Reheating starts the process of carbon atoms diffusing through the material, which causes tiny carbide particles to precipitate and strengthen the metal. Since they define the final qualities of the material, the temperature and time of tempering are crucial. Different tempering temperatures can provide different combinations of hardness, strength, and toughness [112].

1.6 INCONEL 718

Inconel is recognized as a "superalloy." An alloy is a combination of several metals that is mixed to provide a super combination of metallic properties, such as strength and resistance to corrosion. Superalloys, often referred to as heat-resistant, high-temperature, or high-performance alloys [70].

1.6.1 Applications of Inconel 718

The well-known nickel-based superalloy with many uses in many different sectors is Inconel 718. It is an essential material for many vital components due to its remarkable qualities, which include strength at high temperatures, resistance to oxidation, and outstanding corrosion resistance. Inconel 718 is used in turbine discs, combustion chambers, thrust reversers, and other aerospace-related applications while building jet engines, rocket engines, and aircraft constructions [71]. In the energy industry, the alloy is similarly important as it is used in gas turbines for propulsion and power production, especially in parts like rotor discs and turbine blades. Because of its radiation resistance, it is a favored material for important nuclear reactor components. Inconel 718 is also preferred in the oil and gas sector for downhole tools, wellhead

parts, and valves because of its ability to withstand corrosion and fit for high-pressure settings [72]. Inconel 718 is an important component of modern engineering and production because of its remarkable qualities, which promote innovation and dependability in a wide range of applications, including chemical processing, the automotive sector, medical implants, and additive manufacturing [73].

1.6.2 Mechanical Properties of Inconel 718

A unique mix of qualities that make Inconel 718 very desired for a wide variety of applications are provided by its carefully developed chemical composition. Iron, nickel, chromium, and other alloying elements make up the majority of the alloy [71].

Table 1.2: Chemical composition of Inconel 718 [71].

Composition Range of Alloy 718 (wt%)	
Nickel	50.00–55.00
Chromium	17.00–21.00
Iron	Balance
Columbium	4.75–5.50
Molybdenum	2.80–3.30
Aluminum	0.20–0.80
Titanium	0.65–1.15
Manganese	0.35 max.
Silicon	0.35 max.
Boron	0.006 max.
Carbon	0.08 max.
Sulphur	0.15 max.
Magnesium	Residual

Chromium improves the alloy's resistance to oxidation and corrosion, particularly under high-temperature conditions, while nickel contributes to the alloy's remarkable strength and

resistance to corrosion at high temperatures [74]. Structural stability is provided by iron [75]. Furthermore, the alloy's strength at high temperatures, creep resistance, and solid-solution strengthening are enhanced by alloying elements such as molybdenum [76] and niobium [77]. The material created by combining these components has exceptional mechanical qualities, such as high yield and tensile strengths and superior resistance to thermal fatigue [74]. The ability of Inconel 718 to retain strength and integrity at high temperatures is largely due to its special chemical makeup, which makes it the perfect material for use in gas turbines, aircraft, and other industries where durability and high-temperature performance are essential [72].

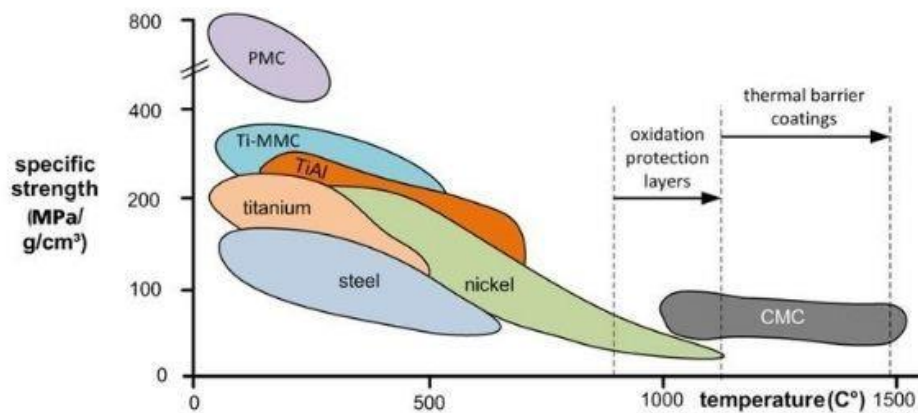


Figure 1.16: shows the specific strength of high-performance materials [70]

1.6.2 Microstructure Phases of Inconel 718

Table 1.3 provides an overview of the stages commonly observed in Inconel 718, including solidification stages of gamma, laves, and MC carbides, which are commonly niobium carbides (NbC). The precipitation phase includes the δ phase and the enhanced precipitates γ' and γ'' . Depending on their dimensions, structure, and arrangement, the solidified phase exhibits

advantageous properties, such as those observed in MC carbides, or unfavorable properties, such as those observed in the Laves phase, to control grain size and structure. As shown in table 1.3, niobium (Nb) plays an important role in the solidification phase and subsequent development of δ , γ' , and γ'' phases [113].

Table 1.3: Inconel 718 Phase Summary [113]

Phase	Crystal Structure	Chemical Formula	Volume Fraction	Nb Content wt. %
γ	FCC	Ni	Bal	
γ'	FCC (L1 ₂)	Ni ₃ (Al,Ti,Nb)	4%	<4%
γ''	BCT (DO ₂₂)	Ni ₃ Nb	16%	4%
δ	Orthorhombic (DO _a)	Ni ₃ (Nb,Ti)	5%	6–8%
Carbide	Cubic	(Nb,Ti)C		
Laves	HCP (TCP)	(Ni,Cr,Fe) ₂ (Nb,Mo,Ti)		10–12%

Chapter 2: Materials and Methods

2.1 BUILD PLATE DESCRIPTION

Sixteen L-PBF AM Inconel 718 build plate artifacts were received fully heat-treated condition (FHT): SR + HIP + Solution +Aged (SOL, AGE) conditions. Table 2.5 shows the heat treatments and times. The build plates and geometric features underwent stress relieving in accordance with ASTM F3055-14a. The HIP was completed per standard ASTM 3301-18a, and the solution and 2-step aging per AMS 5664. The nominal dimensions of the feature build plate were 140 mm in X-orientation, 140 mm in Y-orientation, and 32 mm in Z-height (5.5 in x5.5 in x 1.25 in). The feature build plate volume was 143 cm³, associated with a surface area of 722 cm² and a mass of 1.34 kg. The geometric features include varying angle walls; X- and Y- distances; horizontal holes; and vertical features, including round holes, concentric hollow cylinders, protruding cylinders, varying thin wall thickness, square channels, freeform surface, and varying slot widths.

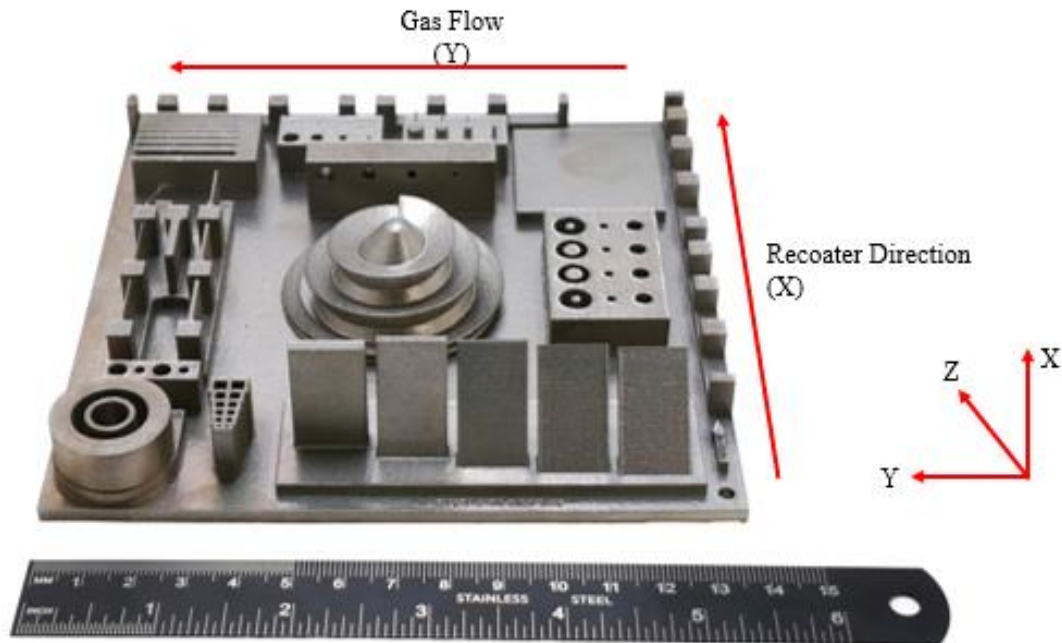


Figure 2.1: L-PBF additively manufactured Inconel 718 feature build plate artifact sample.

2.2 CHEMISTRY OF PLATES

ICP-AES, also known as Inductively Coupled Plasma Atomic Emission Spectroscopy, is a technique employed to ascertain the elemental composition of both metallic and non-metallic materials. The test results yield quantifications of concentrations ranging from trace to major compositional elements.

An ICP Test is conducted utilizing an Inductively Coupled Plasma Spectrometer. The specimen and solution blend is atomized in an argon gas environment and introduced to a plasma that has been heated. The plasma flame's emission of light wavelengths is monitored.

The ICP analysis provides insights into the elemental composition of a given sample, allowing for the identification and quantification of various elements present. The existence of impurities, the existence of supplementary substances, and the categorization of the material based on its elemental composition. ICP test applications encompass the meticulous examination of properties and characteristics, such as its chemical composition, physical properties, and biological content, using scientific methods and techniques.

The ICP analysis is executed in accordance with the ASTM standards, such as ASTM E3061, ASTM E 1019, ASTM E2371, ASTM D1976, and CAP-017 [119].

Table 1.4: Chemistry of plates 1-4

Element	1	2	3	4	Specification
Al	0.45	0.47	0.53	0.41	0.20 - 0.80
B	<0.005	<0.005	<0.005	<0.005	0.006 Maximum
C ¹	0.06	0.05	0.03	0.05	0.08 Maximum
Cb	5.31	5.24	5.25	5.17	4.75 - 5.50
Co	0.13	0.03	0.16	0.23	1.00 Maximum
Cr	18.67	18.85	19.34	19.02	17.0 - 21.0
Cu	0.03	0.03	0.05	0.04	0.30 Maximum
Fe	17.52	17.96	18.28	17.17	Remainder
Mn	0.05	0.07	0.07	0.06	0.35 Maximum
Mo	3.33*	3.13	3.18	3.64*	2.80 - 3.30
Ni ²	53.32	53.15	51.99	53.11	50.0 - 55.0
P	0.008	0.014	0.015	0.011	0.015 Maximum
S ¹	0.002	0.002	0.001	0.001	0.015 Maximum
Si	0.05	0.02	0.06	0.07	0.35 Maximum
Ti	1.00	0.94	0.95	0.92	0.65 - 1.15
N ³	0.02	0.02	0.01	0.03	---
O ³	0.01	0.01	0.02	0.02	---
V	0.02	0.01	0.02	0.02	---
W	0.02	<0.01	0.04	0.03	---

¹ Determined by combustion-infrared absorbance.

² Determined by difference.

³ Determined by inert gas fusion.

* Fails to meet specification

Other elements tested (<0.01%): As, Au, Be, Bi, Ca, Hf, La, Li, Mg, Se, Sn, Ta, Zn & Zr

Results in weight percent unless otherwise indicated.

Method(s): CAP-017S (ICP-AES) and ASTM E 1019-18 (Comb/IGF)

Table 2.1: Chemistry of plates 5-8

Element	5	6	7	8	Specification
Al	0.49	0.50	0.48	0.49	0.20 - 0.80
B	<0.005	<0.005	<0.005	<0.005	0.006 Maximum
C ¹	0.03	0.03	0.03	0.03	0.08 Maximum
Cb	5.20	5.26	5.25	5.13	4.75 - 5.50
Co	0.08	0.43	<0.01	0.02	1.00 Maximum
Cr	19.62	19.02	18.32	19.28	17.0 - 21.0
Cu	0.02	0.01	0.01	0.01	0.30 Maximum
Fe	18.18	18.25	18.18	18.67	Remainder
Mn	0.02	<0.01	0.05	<0.01	0.35 Maximum
Mo	3.14	3.12	3.15	3.07	2.80 - 3.30
Ni ²	52.14	52.34	53.48	52.26	50.0 - 55.0
P	0.013	0.010	0.013	0.011	0.015 Maximum
S ¹	0.001	0.002	0.002	0.001	0.015 Maximum
Si	0.03	0.03	0.03	0.01	0.35 Maximum
Ti	0.97	0.95	0.97	0.99	0.65 - 1.15
N ³	0.01	0.02	0.01	0.01	---
O ³	0.03	0.01	0.01	0.01	---
V	0.02	0.01	0.01	0.01	---
W	0.01	0.01	<0.01	<0.01	---

¹ Determined by combustion-infrared absorbance.

² Determined by difference.

³ Determined by inert gas fusion.

* Fails to meet specification

Other elements tested (<0.01%): As, Au, Be, Bi, Ca, Hf, La, Li, Mg, Se, Sn, Ta, Zn & Zr

Results in weight percent unless otherwise indicated.

Method(s): CAP-017S (ICP-AES) and ASTM E 1019-18 (Comb/IGF)

Table 2.2: Chemistry of plates 9-12

Element	9	10	11	12	Specification
Al	0.48	0.49	0.35	0.48	0.20 - 0.80
B	<0.005	<0.005	<0.005	<0.005	0.006 Maximum
C ¹	0.03	0.03	0.03	0.05	0.08 Maximum
Cb	5.34	5.39	5.27	5.33	4.75 - 5.50
Co	0.11	0.03	0.19	0.03	1.00 Maximum
Cr	18.57	18.98	18.44	18.75	17.0 - 21.0
Cu	0.04	0.01	0.04	0.02	0.30 Maximum
Fe	18.07	18.07	17.75	17.95	Remainder
Mn	0.03	<0.01	0.05	0.07	0.35 Maximum
Mo	3.09	3.20	3.20	3.19	2.80 - 3.30
Ni ²	53.14	52.73	53.57	53.08	50.0 - 55.0
P	0.014	0.011	0.012	0.014	0.015 Maximum
S ¹	0.001	0.001	0.001	0.002	0.015 Maximum
Si	0.04	0.04	0.07	0.02	0.35 Maximum
Ti	0.97	0.98	0.94	0.96	0.65 - 1.15
N ³	0.02	0.01	0.02	0.02	---
O ³	0.02	0.01	0.02	0.02	---
V	0.02	0.01	0.02	0.01	---
W	0.02	0.01	0.03	<0.01	---

¹ Determined by combustion-infrared absorbance.

² Determined by difference.

³ Determined by inert gas fusion.

* Fails to meet specification

Other elements tested (<0.01%): As, Au, Be, Bi, Ca, Hf, La, Li, Mg, Se, Sn, Ta, Zn & Zr

Results in weight percent unless otherwise indicated.

Method(s): CAP-017S (ICP-AES) and ASTM E 1019-18 (Comb/IGF)

Table 2.3: Chemistry of plates 13-16

Element	13	14	15	16	Specification
Al	0.50	0.51	0.50	0.55	0.20 - 0.80
B	<0.005	<0.005	<0.005	<0.005	0.006 Maximum
C ¹	0.04	0.03	0.03	0.03	0.08 Maximum
Cb	5.11	5.04	5.06	5.15	4.75 - 5.50
Co	0.02	0.02	0.05	0.17	1.00 Maximum
Cr	19.17	18.96	18.98	19.12	17.0 - 21.0
Cu	0.01	0.01	0.02	0.04	0.30 Maximum
Fe	18.59	18.39	18.60	17.52	Remainder
Mn	<0.01	<0.01	0.01	0.03	0.35 Maximum
Mo	3.04	3.03	3.09	3.04	2.80 - 3.30
Ni ²	52.48	53.00	52.60	53.22	50.0 - 55.0
P	0.012	<0.005	0.012	0.014	0.015 Maximum
S ¹	0.002	0.002	0.001	0.002	0.015 Maximum
Si	0.01	0.01	0.02	0.07	0.35 Maximum
Ti	0.98	0.97	0.99	0.98	0.65 - 1.15
N ³	0.01	0.01	0.01	0.01	---
O ³	0.02	0.01	0.01	0.01	---
V	0.01	0.01	0.01	0.02	---
W	<0.01	<0.01	0.01	0.02	---

¹ Determined by combustion-infrared absorbance.

² Determined by difference.

³ Determined by inert gas fusion.

* Fails to meet specification

Other elements tested (<0.01%): As, Au, Be, Bi, Ca, Hf, La, Li, Mg, Se, Sn, Ta, Zn & Zr

Results in weight percent unless otherwise indicated.

Method(s): CAP-017S (ICP-AES) and ASTM E 1019-18 (Comb/IGF)

Sixteen samples were received for chemical analysis. Samples 1 and 4 fail to meet the chemical requirements of UNS-N-07718 for a nickel-chromium alloy precipitation hardenable (Inconel 718). The remaining samples meet the chemical requirements of UNS-N-07718 for a nickel-chromium alloy precipitation hardenable (Inconel 718).

2.3 LASER POWDER BED SYSTEMS AND PARAMETERS

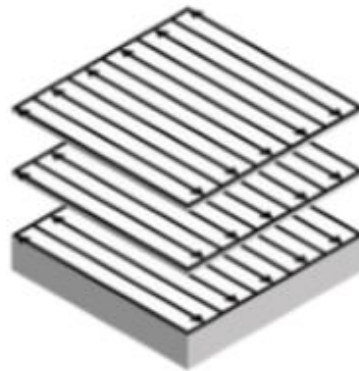
ID	Machine Model Type	Layer Height (µm)	Recoater Type	Power (W)	Scan Speed (mm/s)	Energy Density (J/mm ³)	Core Scan Strategy
1	EOS M400	40	Rubber	285	960	74.2	Stripes
2	EOS M280	40	Steel	-	-	-	Stripes
3	EOS M280	40	-	-	-	-	-
4	EOS M290	40	Carbide Knife	285	960	74.2	Stripes
5	EOS M280	40	Brush	285	960	74.2	Stripes
6	EOS M280	40	Soft Recoater	285	960	74.2	Stripes
7	Concept M2	30	Rubber	180	600	95.2	Checkered
8	EOS M280	40	High-Speed Steel	285	960	74.2	Stripes
9	EOS M290	40	EOS Steel	285	900	-	Stripes
10	SLM280	30	Silicone	200	900	61.7	Stripes
11	SLM280 Dual	30	Silicone	200	900	61.7	Stripes
12	Velo Sapphire	50	Non-Contact	-	-	-	Checkered
13	EOS M290	40	Carbon	285	960	74.2	Stripes
14	EOS M290	40	Steel	285	960	74.2	Stripes
15	EOS M280	40	Carbon Fiber Brush	285	960	74.2	Stripes
16	EOS M290	40	Carbon Fiber Brush	285	960	74.2	Stripes

Table 2.4: Machine overview from shared information of vendor build parameters.

2.3.2 Laser Scan Strategies

The selection of a scanning strategy holds paramount importance as it exerts a substantial impact on the microstructure and mechanical characteristics of the ultimate component. Two frequently utilized scanning strategies in the field are the "line" and "checkerboard" patterns.

The line scanning strategy entails the laser executing a continuous trajectory along a linear path across the powder bed. This methodology is known for its exceptional efficiency and fast processing ability. Nevertheless, a noteworthy attribute is the possible occurrence of columnar grains that are oriented in alignment with the scanning direction. The presence of anisotropy within the microstructure can result in consequential disparities in both the strength and ductility characteristics along distinct orientations within the component.

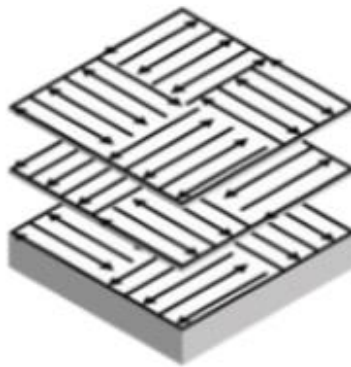


Line Scanning

Figure 2.2: Schematic diagram of line scanning strategy [127].

Checkerboard scanning is a technique commonly used in mechanical engineering to systematically inspect or analyze a surface or object. This method involves dividing the area of interest.

On the contrary, the checkerboard scanning strategy entails the alternating of the laser trajectory between adjacent layers. Through the implementation of laser direction changes for every layer, the proposed pattern attempts to alleviate the anisotropic phenomena encountered during line scanning. The objective is to attain a microstructure that exhibits isotropic characteristics, thereby improving the overall mechanical properties of the component and ensuring uniformity across various orientations.



Checkerboard Scanning

Figure 2.3: Schematic diagram of checkerboard scanning strategy [127].

The choice of a scanning strategy has a direct influence on the mechanical properties and operational efficiency of the manufactured component. Line scanning has the potential to yield anisotropic properties, which may be deemed acceptable or even desirable in certain applications. In contrast, the implementation of checkerboard scanning is devised with the intention of mitigating anisotropy, thereby providing a more homogeneous microstructure, and enhancing the overall mechanical robustness of the component.

2.3.3 Recoater Materials

The recoater blade type has a direct effect on the powder packing density in the LPBF technique out of all the process factors that affect the components produced by additive

manufacturing [113]. The recoater blade exerts a force in the direction of building to compress the powder particles, resulting in a compacted layer of powder [115].

When a compliant blade (e.g., a carbon fiber brush) is utilized for the purpose of depositing powder particles, the particles undergo a gentle spreading process devoid of any externally applied pressure. Snow et al. [116] demonstrated that the utilization of both soft and hard recoater blades exerted a discernible influence on the spreadability of the powder across the build plate. Nevertheless, it has been observed that the spreadability of the powder is highly susceptible to its flowability [114]. In a separate investigation carried out by Dana et al. [117], it was observed that the hard recoater blade exhibited vibrations when in contact with the support structure. This led to irregular powder distribution and, consequently, the formation of voids.

2.3.4 Build Preparation

2.4 HEAT TREATMENTS

The heat treatment schedules shown in Table 2.5 represent relatively standard post-processing treatments for both conventional and additively manufactured Inconel 718 over several decades [118]. Varying angled walls were subjected to stress relief (SR) at $1066 \pm 14^{\circ}\text{C}$ ($1950 \pm 25^{\circ}\text{F}$) for 1.5 hrs. following ASTM3055-14a standard which at a temperature of 1066°C initiated recrystallization of the as-built microstructures. vacuum, hot isostatic pressure (HIP) at 1163°C (2125°F) for 3-4 hours at 103 MPa (15 ksi). HIP provided both continued recrystallization and grain growth. These treatments solubilized existing precipitates and second-phase particles and provided a homogenized grain structure. Solution treated at $1066 \pm 14^{\circ}\text{C}$ ($1950 \pm 25^{\circ}\text{F}$) for 1 hr., cooling at a rate of air cooling or faster and aged at $760 \pm 8^{\circ}\text{C}$ for $10 \text{ h} \pm 0.5 \text{ h}$, furnace cool to $649 \pm 8^{\circ}\text{C}$ until a total aging heat treatment time of 20 hours ($1400^{\circ}\text{F} \pm$

15°F for 10 h ± 0.5 h, furnace cool to 1200°F ± 15°F, hold at 1200°F ± 15°F until a total aging heat treatment time of 20 hours) while attached to build plate. The stress relief performed on varying angles followed ASTM 3055-14a, hot isostatic pressure treatment followed ASTM 3301, solution and 2-step aging was conducted using AMS 5664.

Table 2.5: Full heat-treatment (FHT): (SR+HIP+SOL+AGE) for all the samples

Stress Relief	1066 °C for 1.5 hrs. in vacuum (ASTM 3055-14a)
HIP	1163 °C for 3-4 hours at 15ksi (ASTM 3301)
Solution	1065 ± 3 °C for 1h, cooling at a rate of air cooling or faster (AMS 5664)
Aging	760 ± 9°C for 10 h ± 0.5 h, furnace cool to 649 ± 9°C, hold at 649 ± 9°C until a total aging heat treatment time of 20 hours (AMS 5664)

2.5 METALLOGRAPHIC PREPARATION

From the received plates, shown in figure 2.4, the angled wall section was sectioned off using wire electrical discharge machining (EDM).

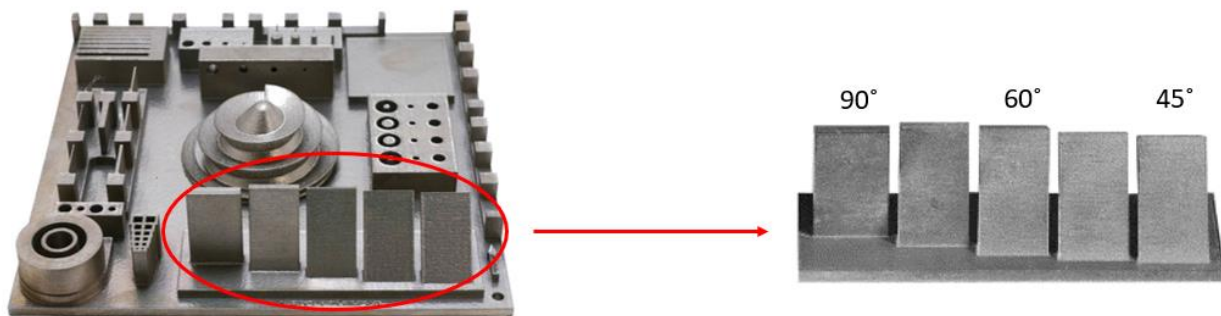


Figure 2.4: Sectioning of angled wall parts

Following, using Autodesk Fusion software, four “dog bone” tensile samples were designed in accordance with ASTM E8 sub-size [139] to be extracted from angles 45,60, and 90 using wire EDM. Once the samples underwent tensile testing, they were mounted.

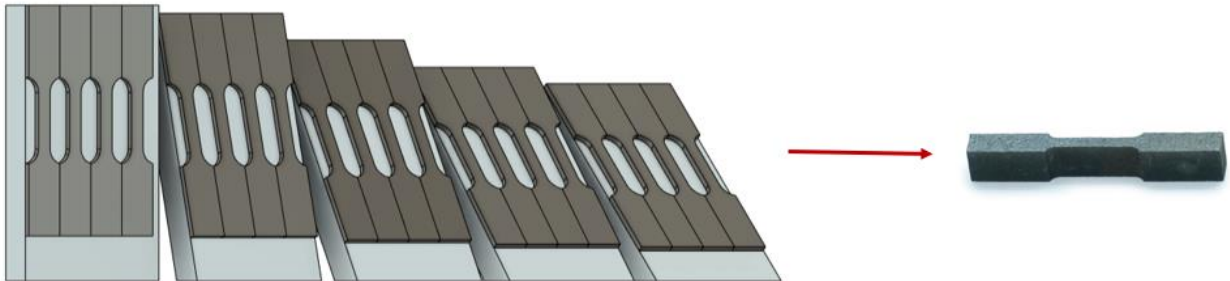


Figure 2.5: Fusion CAD of tensile sample layout

The development of metallographic samples involved the utilization of a blend comprising powdered epoxy and phenolic acid, alongside the application of a hot mounting press sourced from ATM OPAL (Haan, Germany). After the samples were mounted in the ZY direction, they were polished and ground to create a surface mirror like surface.



Figure 2.6: Mounted tensile samples.

The grinding and polishing operations were executed utilizing an ATM SAPHIR 530 semiautomatic system. The grinding procedure started with a 320-grit coarse Si-C (Silicon carbide)

grinding paper, followed by grits 600 and 800 each was spun at 200 RPM with a force of 25N for 2 minutes using water as a lubricant. The polishing operation was executed at a rotational speed of 150 revolutions per minute (RPM) and an applied force of 25 Newtons (N) for a duration of 3 minutes. It is worth noting that distinct nylon disks were employed for each stage of the polishing procedure, utilizing diamond slurries with particle sizes of 6 micrometers (μm), 3 μm , and 1 μm , respectively. The specimens underwent ultrasonic treatment prior to the polishing process and after each subsequent polishing step in order to mitigate any potential cross-contamination.

The etching process involved the utilization of Kalling's No. 2 Reagent, which consists of 2 grams of Copper Chloride (CuCl_2), 40 milliliters of Hydrogen Chloride (HCl), and 40 to 80 milliliters of ethanol. This reagent was employed to etch the polished samples. The etching procedure employed in this investigation involved the utilization of a cotton ball saturated with the etching solution for a duration of 45 to 90 seconds to swab the specimen. The optical micrographs utilized in this study were acquired using an Olympus GX53 inverted optical microscope, manufactured by Olympus Inc. in Tokyo, Japan.

2.5.1 Fractography Preparation

In tensile testing, fractography is a method that entails a thorough analysis of a material's fractured surface after a tensile test. This methodology offers significant insights into the mechanical response of materials subjected to distinct loading conditions, thereby facilitating understanding of failure mechanisms.

Ductile fracture is a notable aspect that can be observed via fractography. In instances of ductile failure, the material experiences localized deformation and necking prior to reaching its ultimate failure point. The fracture surface that ensues frequently exhibits discernible characteristics, such as cavities resembling cups and cones. These observed patterns serve as

indicators of localized regions where the material experienced plastic deformation and subsequently absorbed energy throughout the course of the process. Microvoids are produced during ductile fracture as a result of material separation at the fracture surface. During the ultimate phases of failure, these voids undergo separation at the fracture surface and experience substantial necking, resulting in the development of a distinctive dimpled texture. Equiaxed microvoids, commonly referred to as round dimples, are observed to have undergone separation perpendicular to the fracture plane. In the presence of shear stresses, the coalesced microvoids shall undergo elongation along the shear direction [128].

On the contrary, brittle fractures manifest distinct characteristics. The observed fracture surface exhibits a distinct abruptness, displaying a smooth and devoid of any notable features, while showcasing minimal indications of plastic deformation. This fracture phenomenon manifests itself in the absence of substantial localized thinning, leading to a distinct and sudden detachment of the material. In specific circumstances, materials have the potential to exhibit a fracture mode that combines characteristics of both ductile and brittle fractures. This observation suggests the occurrence of a synergistic effect involving localized plastic deformation and the subsequent manifestation of sudden, more brittle properties.

For the analysis of the fractured surfaces following a tensile test, a custom sample holder (Figure) was designed, and 3D printed. Copper tape was applied to the underside of the tensile samples to establish a stable base, preventing any unintended movement. The sample holder is structured with outer edges for 45-degree samples, a middle section for 60-degree samples, and an inner circle for 90-degree samples. This design allows for systematic organization and examination of samples with varying orientations for SEM imaging.

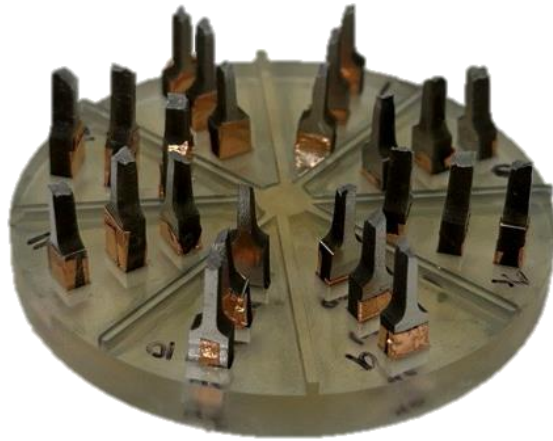


Figure 2.7: Tensile sample holder for SEM imaging (YZ)

2.6 SPECIMEN TESTING

2.7.1 Tensile Testing

Tensile testing, an essential mechanical assessment technique, assumes a critical role in comprehending and characterizing the mechanical characteristics of materials. This commonly utilized test entails subjecting a material specimen to gradual axial forces until it attains a state of failure or notable deformation. The outcomes derived from the process of conducting tensile testing offer valuable insights into the mechanical response of the material when subjected to tension. Parameters such as Ultimate Tensile Strength (UTS), Yield Strength, Elongation at Break, Young's Modulus, and Strain are essential metrics that provide valuable insights into the material's mechanical properties, including its strength, ductility, and elasticity. Performing tensile testing in accordance with internationally recognized standards such as ISO 527-4, ISO 527-5, ASTM D 638, ASTM D 3039, and ASTM C 297 [121]. These tests facilitate the generation of stress-strain diagrams, which are subsequently employed for the determination of the tensile modulus.

Tensile tests were performed at Touchstone Testing Lab (TTL) (Triadelphia, WV) using a specialized extensometer “Epsilon, 4mm GL, Model# 3442-004M-020M-LHT. Load Cell tested on the calibrated range of 2.5kip, MTS Model# 661.21A-01. Test Frame was MTS Model 312.21 and LVDT -- +/- 3.0” range, MTS Model 244.12. The calipers used were Mitutoyo Model CD-6 CX. Test Fixture, with Smooth Grip Wedges, was a TTL Built custom design with custom L’s for specimen alignment during testing. The initial test speed was 0.015 in/in/min, and the secondary test speed was performed at 0.010 in/min. Testing performed resulted in data points collected for 0.2% Offset Yield, 4mm GL and calculated elongation based on fitback marks / measured after fracture.

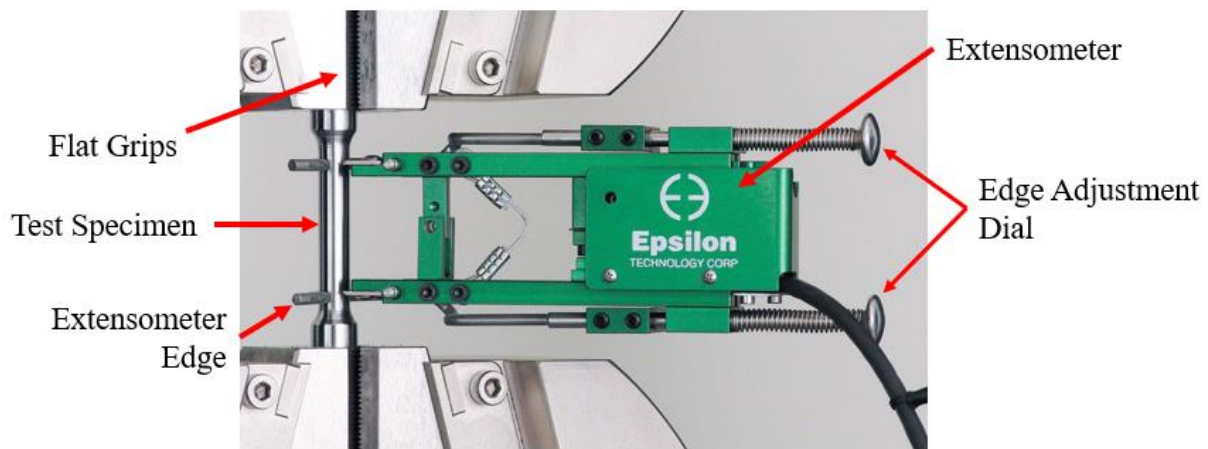


Figure 2.8: Schematic View of Tensile Test [120].

2.7.1.1 Elongation

When a material is exposed to a tensile load, elongation is a measurement of the deformation that takes place prior to the material breaking. Upon the application of a tensile load, the material undergoes elongation in length and experiences a consistent reduction in cross-sectional area, all the while ensuring that the volume remains constant.

A tensile test usually starts with the specimen placed without a load. Upon the commencement of the load, one can observe uniform elongation and a decrease in the cross-sectional area. This process persists until the maximum load capacity is attained. Subsequently, the phenomenon of necking transpires, resulting in the manifestation of non-uniform deformation solely within the region of the neck. The local true stress exhibits a persistent rise as the cross-sectional area of the neck diminishes, eventually resulting in fracture [122].

During tensile testing, the following formula may be used to calculate elongation at any length L:

$$\delta = L - L_0$$

where, δ = elongation, (in or mm), L_0 = initial gauge length between marks, (in or mm), L = length between marks at any point during uniform elongation, (in or mm).

In a tensile test, percent elongation is a mechanical parameter that quantifies how much a material can stretch or deform before breaking. The expression is quantified as a dimensionless ratio, denoted as a percentage, and is determined through the utilization of the following formula where L_f = final specimen length, (in or mm), L_0 = original specimen length, (in or mm) [122].

$$\% \delta = \frac{(L_f - L_0)}{L_0} \cdot 100$$

Percent elongation serves as a measure to quantify the extent of elongation or stretching exhibited by a material, expressed as a percentage of its initial length prior to experiencing failure. Materials exhibiting higher percentages of elongation are typically regarded as possessing superior ductility, thereby enabling them to endure more substantial deformation prior to experiencing failure [123].

2.7.1.2 Ultimate Tensile Stress

The ultimate tensile strength (UTS) is a vital material characteristic that signifies the utmost load a material can withstand prior to experiencing failure. Utilizing the method of tensile testing, a machine exerts a unidirectional force upon a test specimen until its structural integrity is compromised, resulting in fracture. The elongation rate and applied force are essential parameters for determining various mechanical properties. The ultimate tensile strength (UTS) is calculated by dividing the applied force required to fracture the material by its initial cross-sectional area. It denotes the critical juncture wherein a substance experiences structural failure, thereby indicating its capacity to withstand an externally imposed force. Materials initially experience elastic deformation, during which they exhibit a reversible response to applied forces. Subsequently, they undergo plastic deformation, wherein their response becomes irreversible as seen in figure 2.9. This deformation process continues until the material reaches its ultimate tensile strength which represents the maximum force it can endure before fracturing [124].

2.7.1.3 Yield Stress

One metric that is utilized in materials testing, particularly when figuring out a material's yield strength, is the yield stress offset. The yield strength, also known as the elastic limit, is the critical stress level at which a material initiates the onset of plastic deformation. This signifies the point at which the material experiences irreversible deformation, without any further escalation in the externally applied stress. The offset method is a widely utilized technique for ascertaining the yield strength [125].

The ability of a material to stretch under tension is known as ductility. More than brittle material, ductile material will extend during deformation. Before fracture, ductile materials exhibit significant deformation, plastic distortion, or necking. ductile fracture, is preferable to brittle

fracture due to its slow propagation and high energy absorption prior to fracture. Because of the additional strains on the metals in high-temperature and high-pressure applications in reactor plants, ductility is desirable. In these applications, high ductility aids in preventing brittle fracture.

Brittle materials fracture under stress conditions with minimal elastic deformation and minimal plastic deformation. Even materials with high strengths can become brittle by absorbing relatively little energy before breaking. When there is a brittle fracture, cracks spread quickly and there is no visible plastic deformation prior to fracture [130].

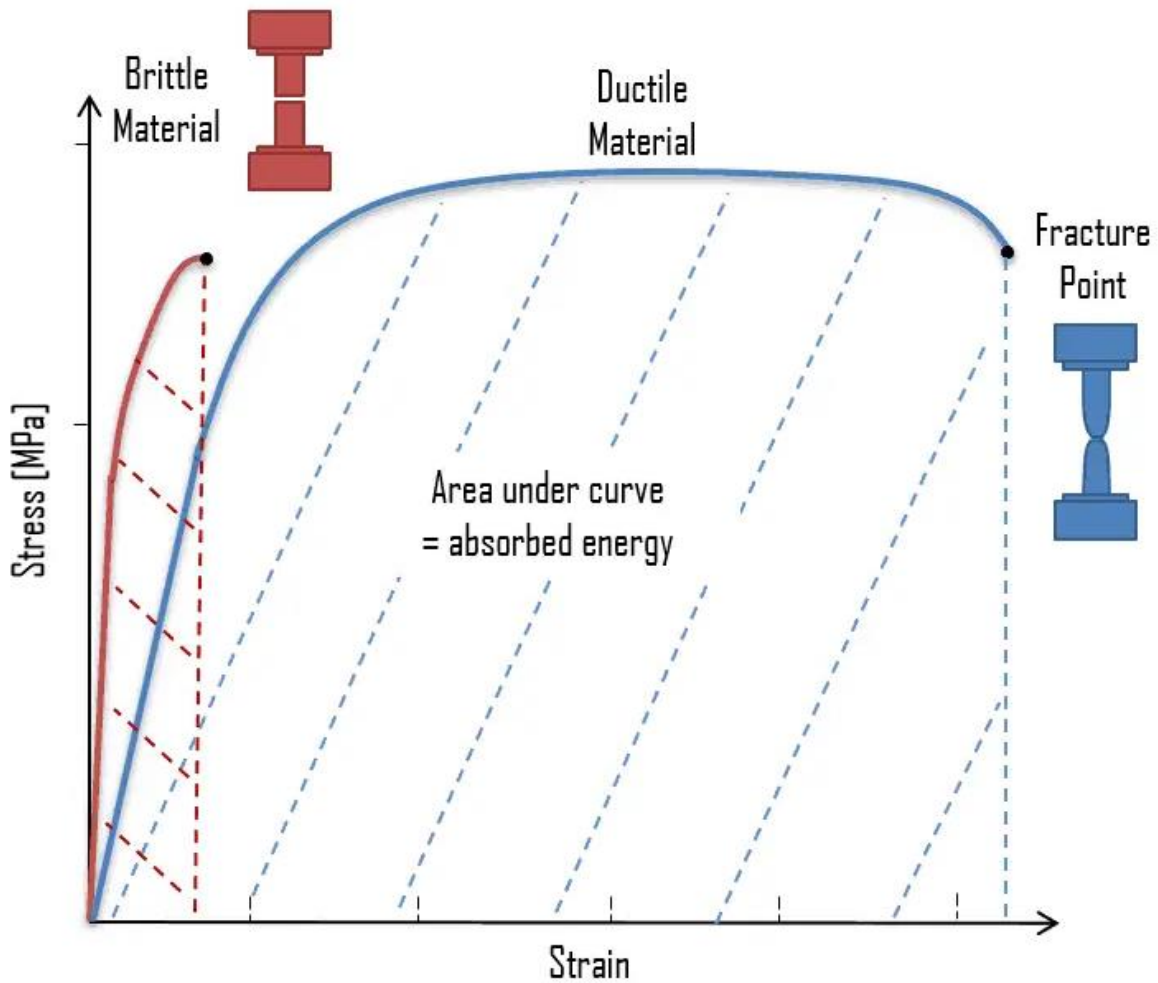


Figure 2.9: Ductile vs Brittle Material Stress- Strain Curve [130].

The process of determining the yield strength entails the application of an offset to the stress-strain curve, commonly referred to as the yield stress offset. The stress-strain curve conventionally exhibits a segment of linear elasticity succeeded by a segment of non-linear plasticity. The yield stress offset is commonly represented as a proportion of strain or deformation relative to the elastic region. The stress value at 0.2% corresponds to the point on the stress-strain curve where plastic deformation initiates, and it is located at a strain offset of 0.2% from the elastic region. The yield stress offset method offers a standardized approach for determining the yield strength, especially for materials lacking a clearly defined yield point on their stress-strain curve [126].

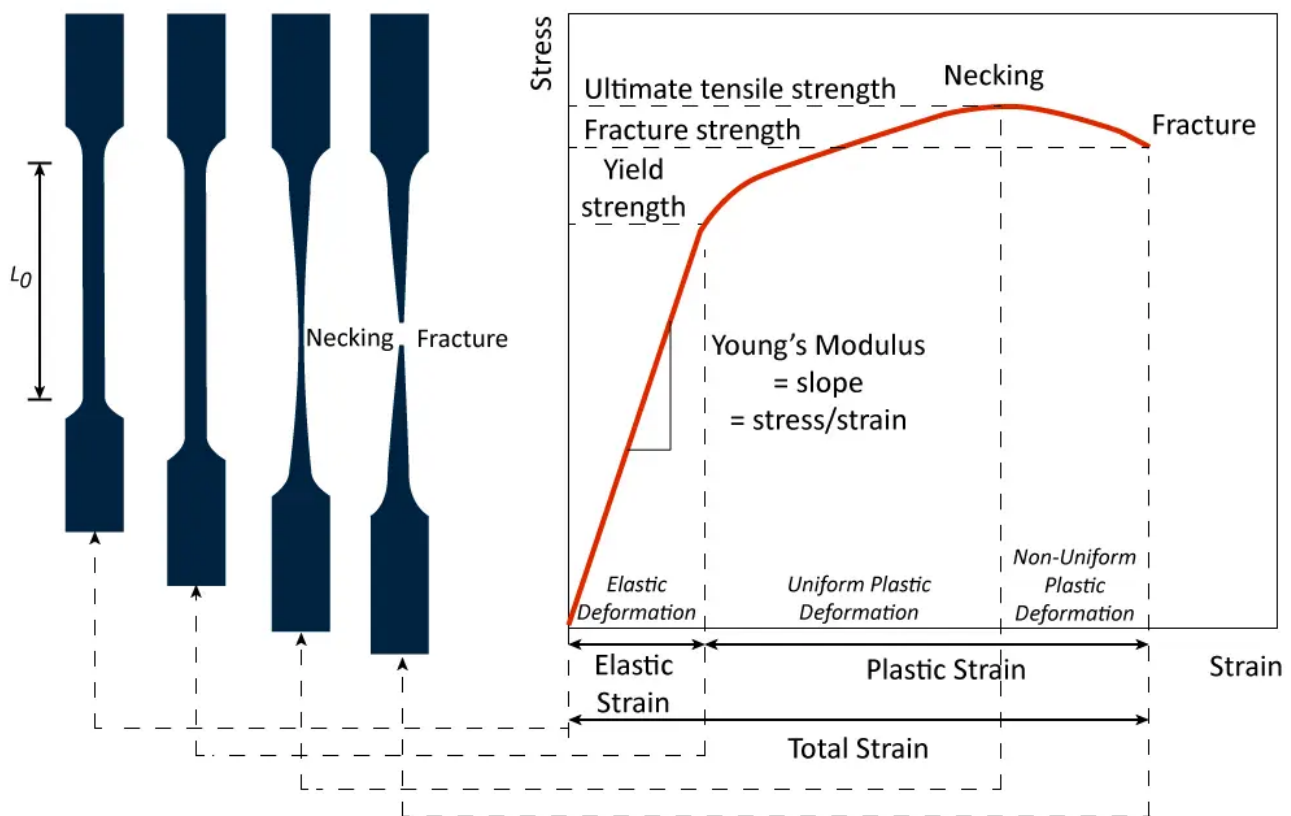


Figure 2.10: Typical stress-strain curve and shape deformation of the specimen from start to fracture. [122].

Chapter 3: Results and Discussion

3.1 SPECIMEN TESTING RESULTS

3.1.1 Hardness Testing

The Vickers hardness testing technique is a widely employed method for the purpose of quantifying the hardness of various materials, with a particular focus on metals and alloys. The process entails applying a predetermined force to the material's surface by means of a diamond indenter, typically in the form of a pyramid. The dimensions of the indentation, resulting from the applied force by the indenter, are subsequently assessed using a microscope. The determination of the hardness value is derived from the precise evaluation of the indentation area in conjunction with the magnitude of the applied force. This test is deemed advantageous due to its ability to furnish a continuous scale of hardness values, rendering it suitable for application across a variety of materials, covering those of significant hardness. Additionally, it exhibits a relatively minimal sensitivity to the dimensions of the specimen, thereby rendering it highly adaptable for a diverse range of applications [133]. The QATM CHD Master+ micro hardness tester was employed for testing.

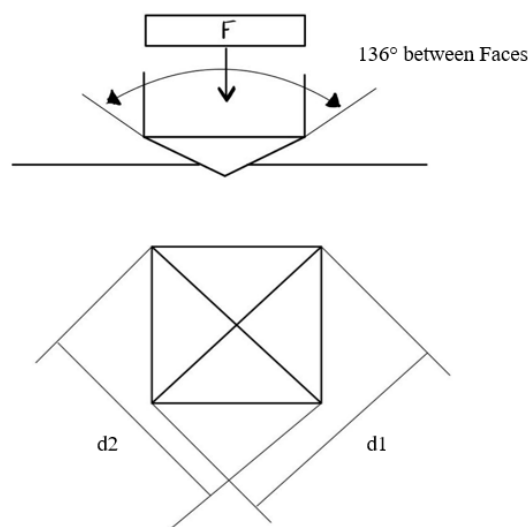
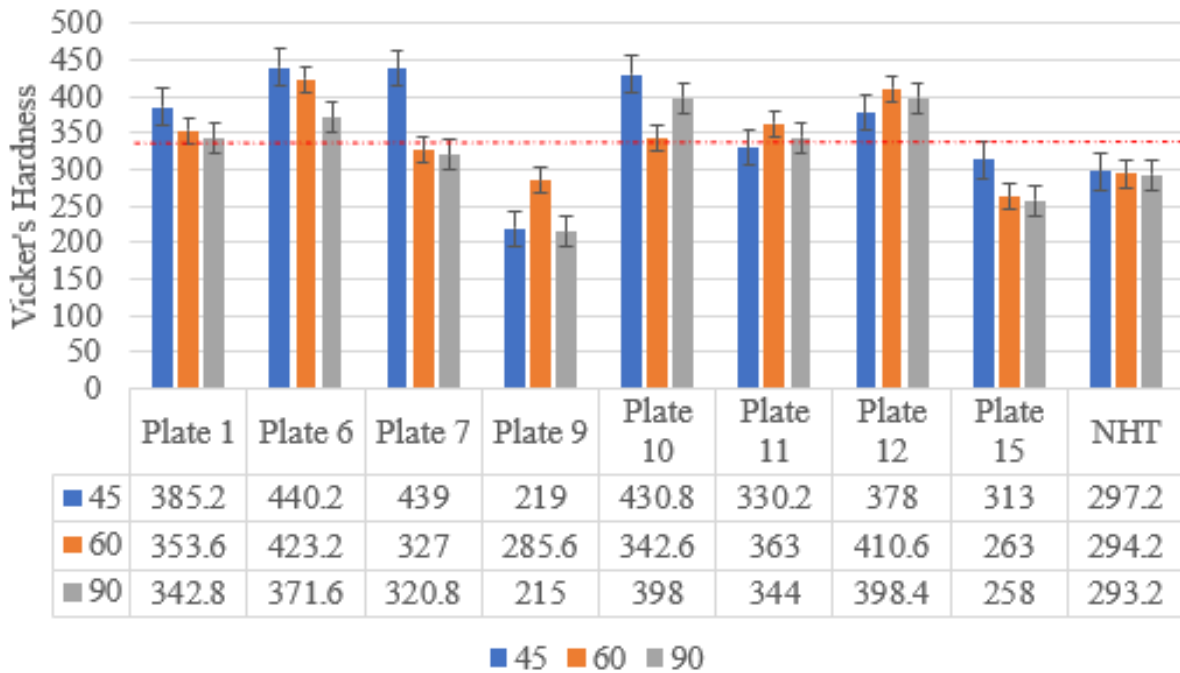


Figure 3.1: Vickers hardness measurement scheme.

According to data from the scientific literature, post-heat treatments—like solution annealing and aging—are frequently employed to change the mechanical characteristics of Inconel 718 produced by laser powder bed fusion, including its hardness. These treatments can substantially enhance the material's hardness. Although precise values regarding the hardness post-heat treatment are not directly available, it is commonly acknowledged that these procedures can elevate the hardness of Inconel 718 to enhanced hardness. The hardness of AMS 5662 material exhibits a range of approximately 20-25 Hardness Rockwell C (HRC) in its as-received state. However, it is worth noting that the hardness can be enhanced through the process of aging, resulting in a potential increase to approximately 36-44 HRC. It is important to acknowledge that the precise value within this range is contingent upon the specific parameters employed during the heat treatment process, encompassing factors such as temperature, duration, and cooling rate [140]. In accordance with the AMS 5662 - UNS N07718 standards, fully heat-treated Inconel 718 is expected to have a minimum hardness level of 36 HRC, 342 Vickers (VH) [131, 132]. The examination of the samples revealed that most samples surpass this specified minimum threshold, however some are below.

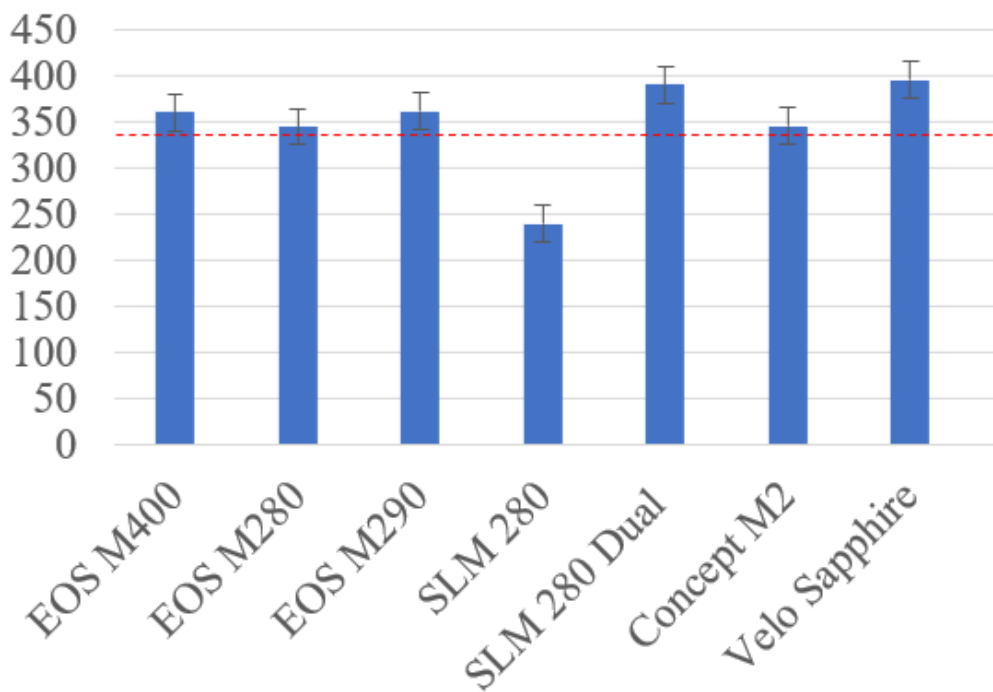
Table 3.1: Plate Hardness Results



The hardness testing results shown in table 3.1 demonstrate varied performance in Vickers Hardness (VH) across different plates and angles. The established minimum required hardness level is 342 VH, as delineated by the red dotted line. For Plate 1, samples tested at 45 and 60 degrees both exceed the minimum hardness requirement, with values of 385.2 VH and 353.6 VH respectively. The sample at 90 degrees hovers just at the minimum with a hardness of 342.8 VH. Plate 6 and Plate 12 show exceptional hardness, with all tested angles comfortably surpassing the minimum requirement. Plate 7 exhibits variability in hardness; the 45-degree angle sample notably exceeds the threshold with a hardness of 439 VH, while the 60 and 90-degree angle samples fall short, with values of 327 VH and 320.8 VH respectively. Plate 9 and Plate 15 do not meet the minimum hardness requirements at any angle. The No Heat Treatment (NHT) does not meet the minimum hardness requirements at any angle but meets the minimum for untreated Inconel 718 standing at an average of 294 surpassing the minimum of 230. Plate 10 meets the required hardness levels across all angles, but the 60-degree angle sample is just over the line with a hardness of 342.6 VH, making it marginally compliant. Plate 11 presents a range of results; the 60-degree

angle sample surpasses the minimum with a hardness of 363 VH, the 90-degree angle is just over the threshold at 344 VH, while the 45-degree angle does not meet the minimum with a hardness of 330.2 VH. Notably, samples at the 45-degree build orientation tend to exhibit the highest hardness values, indicating that this angle may be optimal for achieving superior hardness characteristics.

Table 3.2: Machine hardness results



The average Vickers Hardness values, derived from a variety of machines and computed by averaging the data points from the previous graph, shown in table 3.2, for samples fabricated at orientations of 45, 60, and 90 degrees, exhibit a visible efficacy in meeting the set minimum hardness threshold of 342 VH. The EOS M400, EOS M280, EOS M290, SLM 280 Dual, Concept M2 and Velo Sapphire machines have all generated samples that are successfully above the threshold, demonstrating a processing capacity that can be relied upon to achieve the appropriate levels of hardness. The compiled data indicates a deviation in machine performance, wherein the

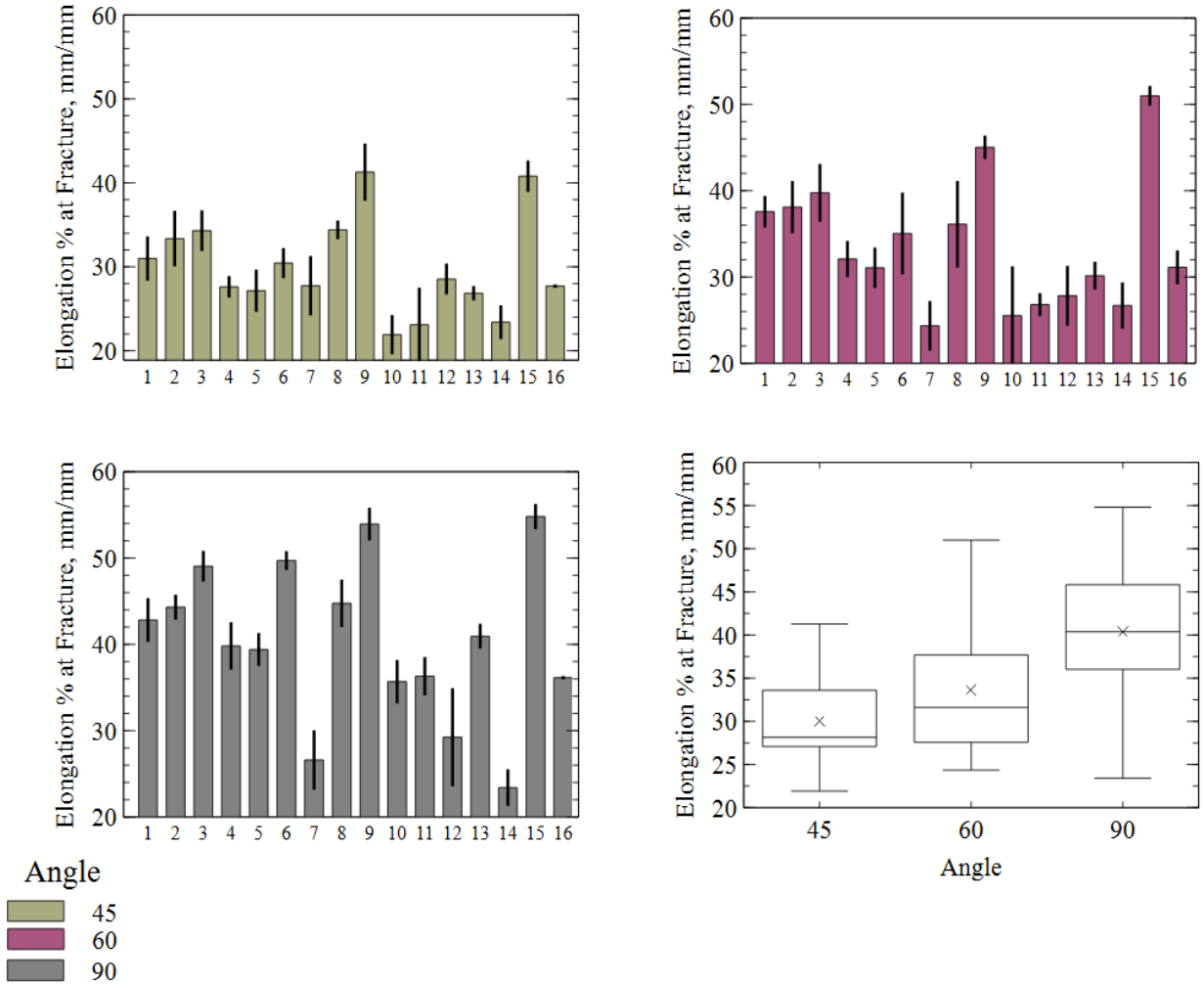
majority of machines demonstrate the ability to meet or surpass the industry-established hardness standard. However, one particular machine has been identified as underperforming, highlighting the significance of meticulous machine selection in additive manufacturing procedures to attain desired material properties.

3.1.2 Tensile Testing

The results of the tensile testing, as presented below, provide critical insights into the mechanical properties of the tested material. These outcomes not only reflect the material's ultimate tensile strength, yield stress, and elongation at break, but also offer valuable data for evaluating its suitability for specific build orientation. The data aligns with the anticipated behavior of the material under stress, revealing its practical capabilities and limitations. This information is essential for making informed decisions regarding machine and orientation selection.

3.1.2.1 Elongation

Table 3.3: Elongation % at Fracture, mm/mm



The tensile test results samples pulled at a 45-degree orientation show the lowest elongation percentages at fracture. This suggests that the material has the least ductility when the force is applied at this angle. The variability in elongation across the samples, as indicated by the error bars, could reflect inconsistencies in the material's microstructure or experimental error during testing. Such low ductility at this orientation could be a result of the material's anisotropic properties, which means that its mechanical properties vary with direction.

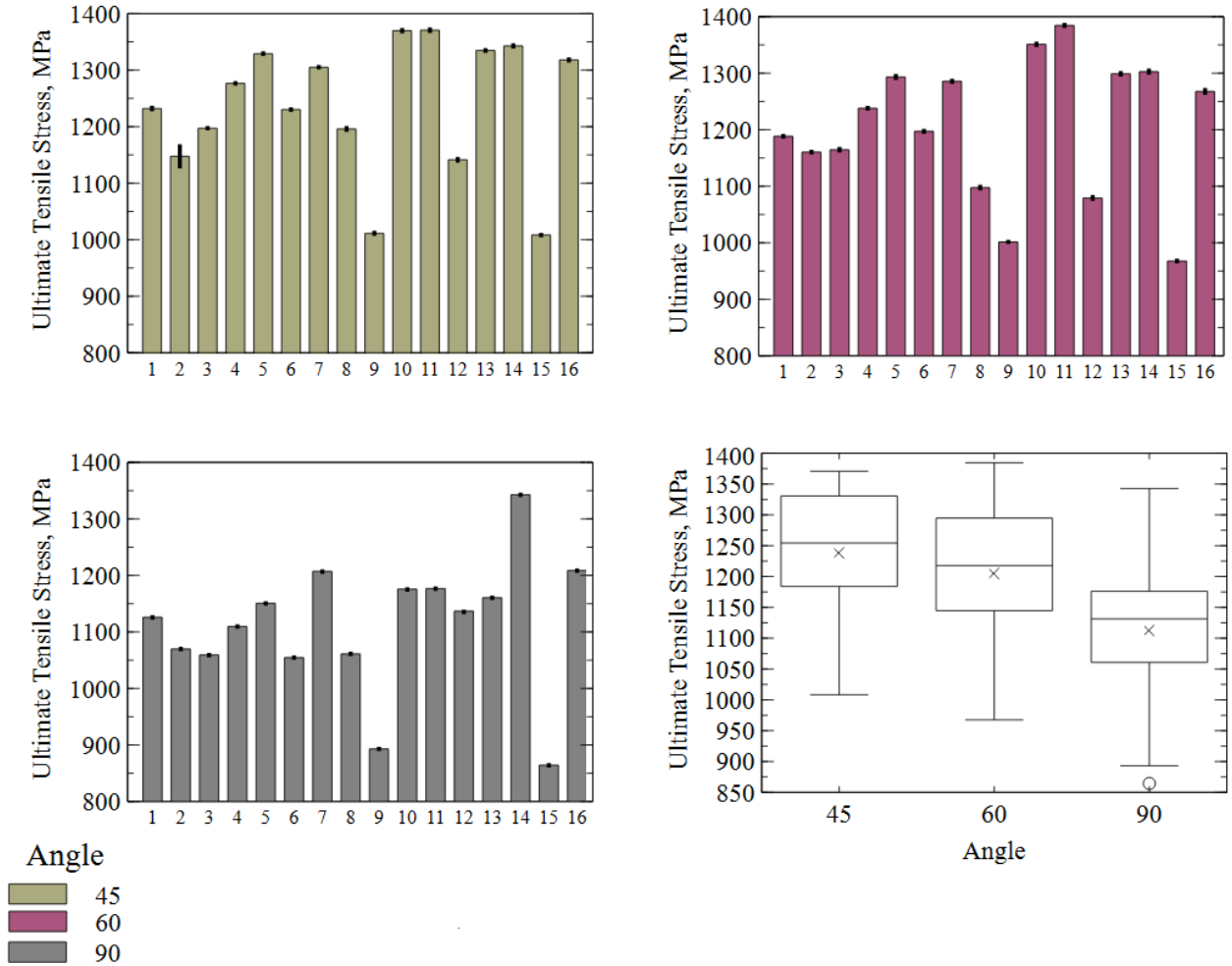
For the samples tested at a 60-degree orientation, there is a noticeable increase in elongation percentages compared to the 45-degree orientation. While there is still a fair amount of variation among the samples, the overall trend indicates improved ductility at this angle. This could be attributed to the directional nature of the material's grain structure, which may be more favorably aligned to accommodate deformation when stress is applied at 60 degrees.

The highest elongation percentages are observed in the samples tested at a 90-degree orientation. This implies that the material exhibits its greatest ductility when the tensile force is aligned perpendicular to the direction used in the 45-degree tests.

The box plot provides a clear statistical overview of the three sets of data. It highlights that the median elongation at fracture is lowest for the 45-degree orientation and increases for the 60-degree samples, reaching the highest values for the 90-degree orientation. From the lowest elongation, 45, to the highest, 90, there was an average increase of 35% in sample's elongation.

3.1.2.2 Ultimate Tensile Stress

Table 3.4: Ultimate Tensile Stress, MPa



Based on the observed attributes of the samples in Table 3.4, it can be inferred that:

The samples at a 45-Degree Angle exhibit a high Ultimate Tensile Strength while displaying a low elongation characteristic. This indicates the presence of a strong material that effectively withstands stress yet exhibits limited deformation prior to fracture. Optimal for scenarios necessitating high structural integrity, with minimal tolerance for deformation.

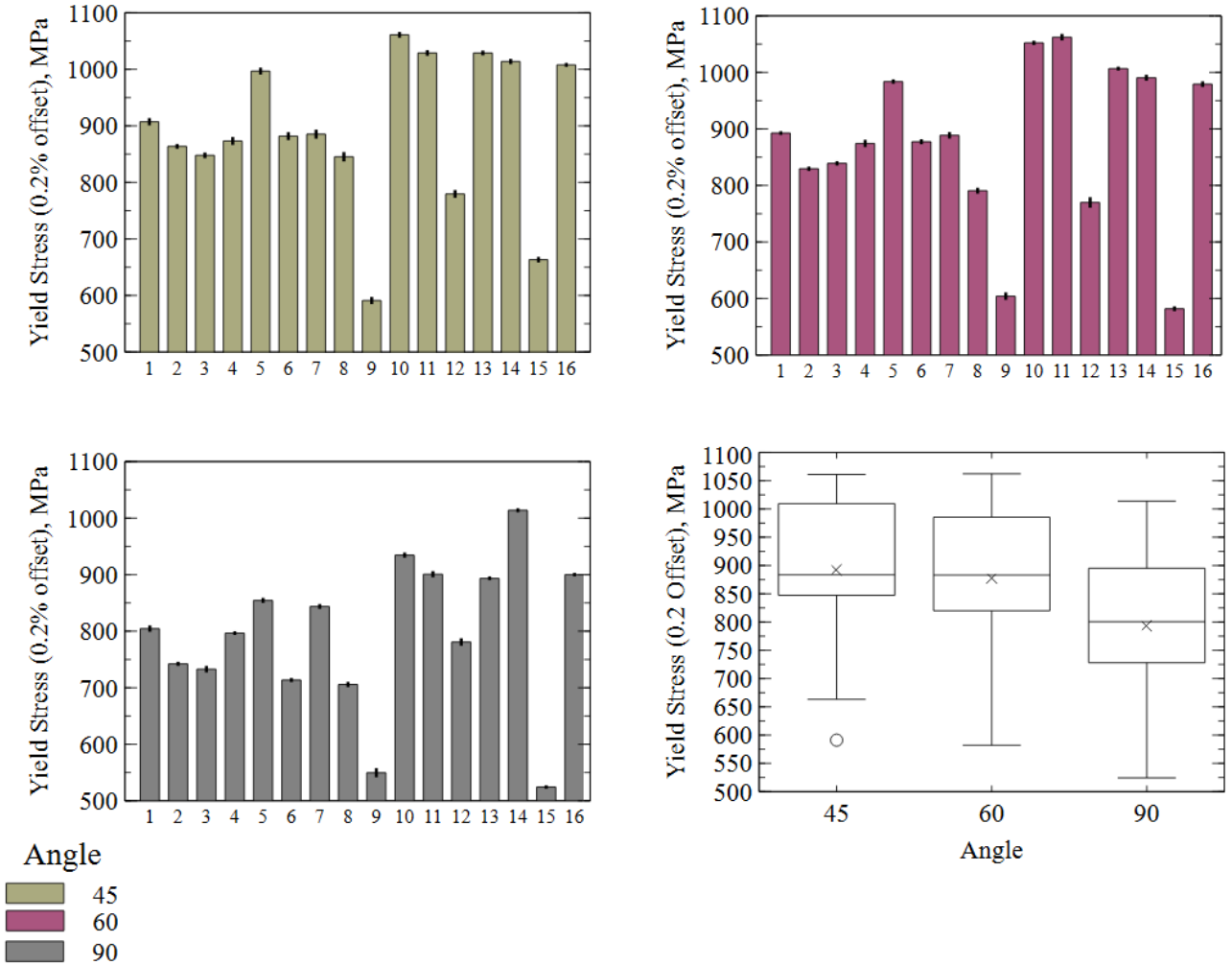
The Samples at a 90-degree angle observed decrease in ultimate tensile strength accompanied by an increase in elongation indicates a material with reduced strength yet enhanced ductility. This characteristic enables the material to undergo greater deformation and absorb a higher amount of energy. Optimal for use cases wherein the prioritization lies in the prominence of flexibility and ductility over attaining the utmost strength.

The samples at a 60-degree angle exhibit intermediate Ultimate Tensile Strength and elongation, suggesting a harmonious equilibrium between structural integrity and malleability. These may be favored in situations where an optimal trade-off is required.

The superiority of an angle is not intrinsically determined; rather, it is contingent upon the specific demands of the application. Materials with high tensile strength and low elongation are employed in applications where the utmost emphasis is placed on strength and stiffness, whereas materials with high elongation are utilized in scenarios where the absorption of energy and ductility are of greater significance. Materials exhibiting a harmonious combination of properties are highly suitable for applications necessitating a judicious blend of adequate strength and ductility.

3.1.2.3 Yield Stress

Table 3.5: Yield Stress, 0.2% Offset, MPa



The 45-degree samples point to a ductile, highly deformable material because of their high yield stress and elongation and low ultimate tensile strength. The samples exhibit a notable resistance to deformation under significant applied force yet possess a relatively limited ability to withstand extreme loads prior to experiencing structural failure. Hence, although this material exhibits high deformability, it does not possess optimal strength when subjected to maximum stress conditions.

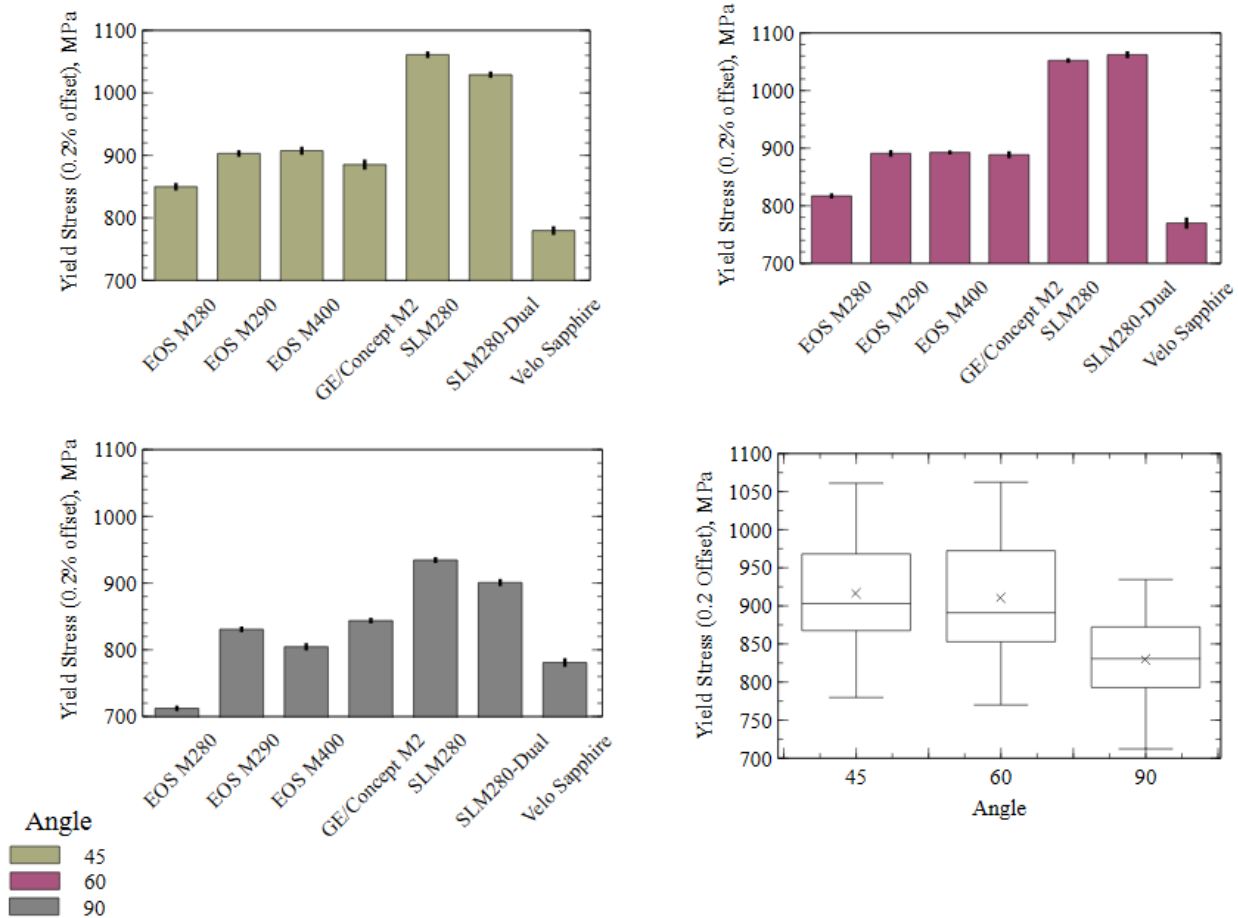
The samples at a 60-degree angle exhibit a well-balanced profile, showcasing intermediate values for elongation, ultimate tensile strength, and yield stress. This implies a harmonious trade-off between structural integrity and malleability, rendering it adaptable for implementations necessitating an equilibrium between said characteristics.

In contrast, the samples at a 90-degree angle exhibit notable traits such as reduced elongation, elevated ultimate tensile strength, and diminished yield stress. These characteristics suggest the samples possess robustness and the ability to endure substantial peak loads, but with limited deformation capacity prior to fracture. The material exhibits a reduced susceptibility to permanent deformation, while simultaneously demonstrating an enhanced resistance to fracture resulting from its elevated ultimate tensile strength (UTS).

Given that UTS is the greatest stress a material can withstand before breaking under tensile stress, samples with 45 degrees of stress would normally fail first. However, it is important to note that this analysis does not consider variables such as loading rate or the existence of defects, both of which can significantly impact the likelihood of failure. The samples with a 90-degree orientation, despite exhibiting a relatively low yield stress, are expected to exhibit superior resistance to failure owing to their elevated ultimate tensile strength. The samples with a 60-degree angle would demonstrate failure characteristics that are intermediate in nature, occurring subsequent to the failure of the samples with a 45-degree angle but preceding the failure of the samples with a 90-degree angle.

3.1.3 Machine Results

Table 3.6: Machine's Yield Stress



The graphs shown in table 3.6 show a comprehensive summary of the yield stress data obtained from 16 distinct samples, each produced by different machines operating at varying build angles. The results play a crucial role in comprehending the performance and dependability of the manufacturing procedures employed by each machine.

In the build angle of 45 degrees, the order of yield stress from highest to lowest is as follows: SLM, Dual, EOS M400, EOS M290, Concept, EOS M280, Velo. Based on the analysis, it can be inferred that the SLM and Dual machines exhibit enhanced proficiency in fabricating materials with superior strength characteristics at the specified orientation. The comparatively

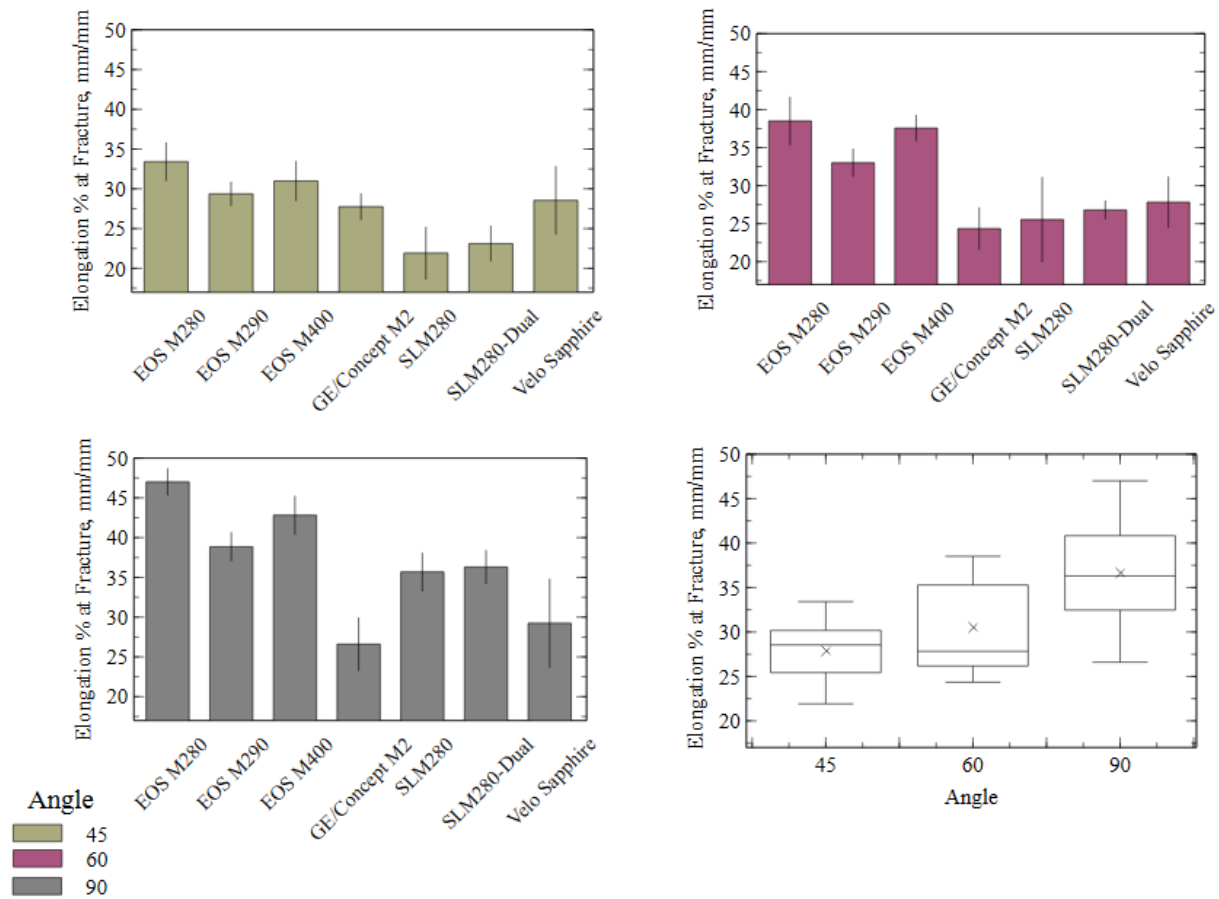
inferior performance of the Velo and EOS M280 machines may potentially suggest suboptimal process efficiency or material utilization during the construction process at a 45-degree orientation.

The order of strongest to weakest in the 60-degree build angle is as follows: Dual, SLM, EOS M400, EOS M290, Concept M2, EOS M280, Velo. The Dual machine exhibits exceptional performance in this orientation, showcasing its specific ability in fabricating materials with superior strength at a 60-degree inclination. The SLM machine consistently upholds a superior position in terms of performance, whereas the Velo machine consistently exhibits a lower yield stress. This observation further supports the claim that the Velo machine's manufacturing process may not possess the same level of robustness as the other machines, particularly when considering these specific build angles.

Lastly, the results of the 90-degree build in order of highest to lowest yield stress: SLM 280, SLM 280-Dual, Concept, EOS M290, EOS M400, Velo, and EOS M280. The SLM 280 and SLM 280-Dual machines consistently exhibit the best performance across all angles, demonstrating their dependability and sophisticated capacity to produce materials with high yield stress. Interestingly, the Concept machine exhibits a notable enhancement at this specific inclination, potentially indicating that its manufacturing procedure is finely tuned for vertical constructions. On the contrary, the performance of the EOS M280 machine is comparatively suboptimal.

The data obtained from the provided graphs demonstrate that the manufacturing angle exerts a noteworthy influence on the material properties of the manufactured articles. The SLM and Dual machines exhibit commendable performance consistently at different angles, suggesting a higher level of dependability and a more precise manufacturing process for producing materials with higher yields stress. However, it is worth noting that the EOS M280 machine exhibits a decrease in yield stress regardless of the build angle, indicating possible constraints in its manufacturing capabilities or the materials used.

Table 3.7: Machine's Elongation at Fracture



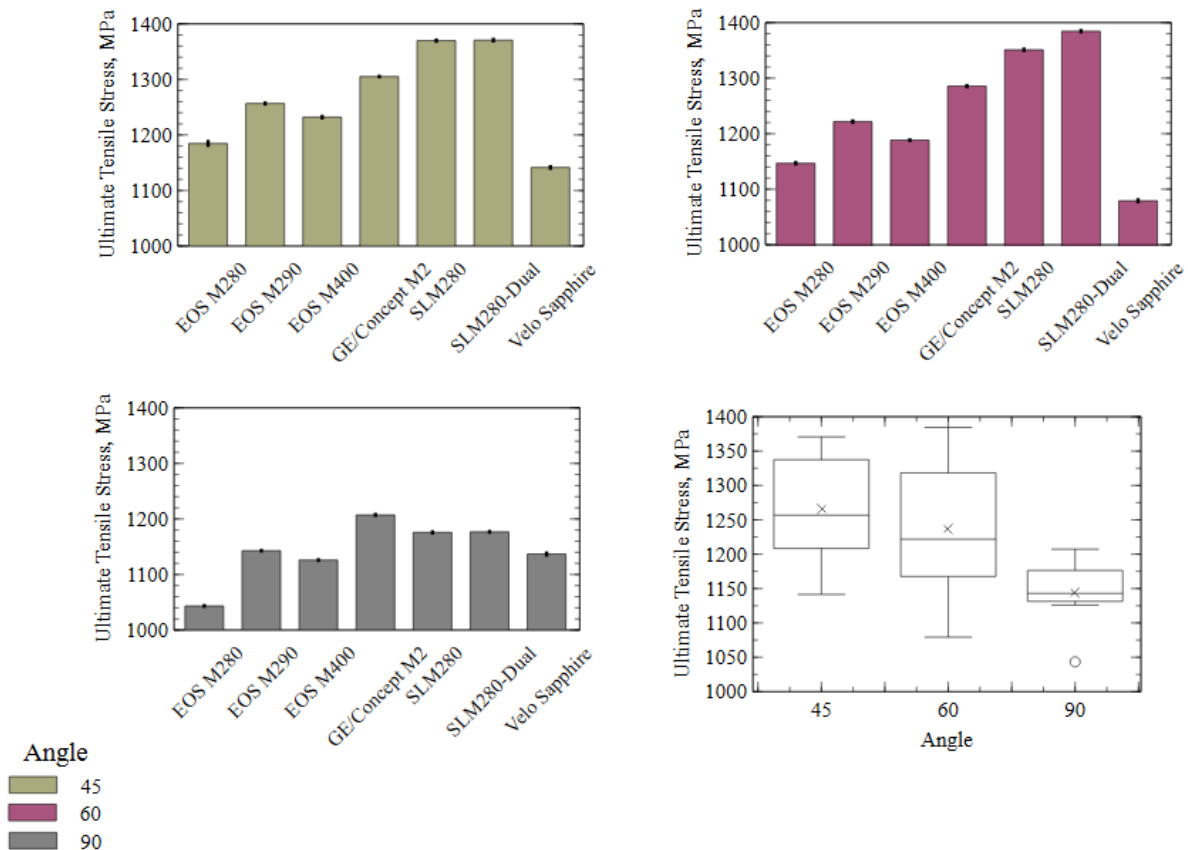
The graphs illustrate the percentage of elongation at fracture for samples fabricated at different angles, providing valuable insights into the ductility characteristics of the materials produced by distinct machinery. Ductility, a fundamental characteristic in the field of materials science, signifies the inherent capacity of a material to undergo deformation when subjected to tensile stress.

At the 45-degree samples, it is observed that the EOS series machines (M280, M400, M290) exhibit superior elongation characteristics, indicating their exceptional performance in fabricating ductile materials in this specific alignment. The Velo and Concept machines exhibit a level of ductility that can be classified as moderate, whereas the Dual and SLM machines

demonstrate a comparatively lower level of ductility. This implies that, in scenarios necessitating the utilization of pliable or less fragile substances at a 45-degree construction inclination, the EOS machines would be deemed more advantageous.

Moving to the 60-degree angle, the EOS machines continue to exhibit superior ductility, but with slight reordering of their respective rankings. The consistent performance of the EOS machines at various angles highlights their robustness in manufacturing ductile materials, regardless of the chosen build orientation. Similar trends to the results at 60 degrees may be seen at 90 degrees. The EOS machines once again demonstrate their superior performance, further validating their suitability for applications requiring high ductility, irrespective of the build angle.

Table 3.8: Machine’s Ultimate Tensile Stress



The set of graphs shown in table shows the ultimate tensile stress values of samples made at construction angles of 45, 60, and 90 degrees using different machines. The ultimate tensile strength serves as a pivotal parameter in assessing the mechanical strength of a material. It signifies the utmost stress that a material can withstand under tension before experiencing failure.

In accordance with the 45-degree build angle, the UTS ranking, arranged in descending order, is as follows: Dual, SLM, Concept, EOS M290, EOS M400, EOS M280, Velo. The aforementioned statement suggests that the Dual and SLM machines exhibit notable effectiveness in fabricating builds that possess excellent tensile strength in this specific orientation. Consequently, these machines are deemed suitable for applications that strong tensile properties hold highest priority. The EOS series exhibits moderate tensile strengths, with the Velo machine positioned towards the lower range. This implies that it may not be the optimal selection for applications requiring high-strength performance in this scenario.

At the 60-degree builds, the ranking remains consistent with the outcomes observed at the 45-degree angle, wherein Dual, SLM, and Concept retain their prominent positions. The consistent performance observed in the Dual and SLM machines at these specific angles indicates their commendable reliability in fabricating materials capable of enduring substantial tensile stress. The Concept machine showcases a noteworthy ultimate tensile strength, whereas the Velo machine consistently exhibits inferior tensile strength values.

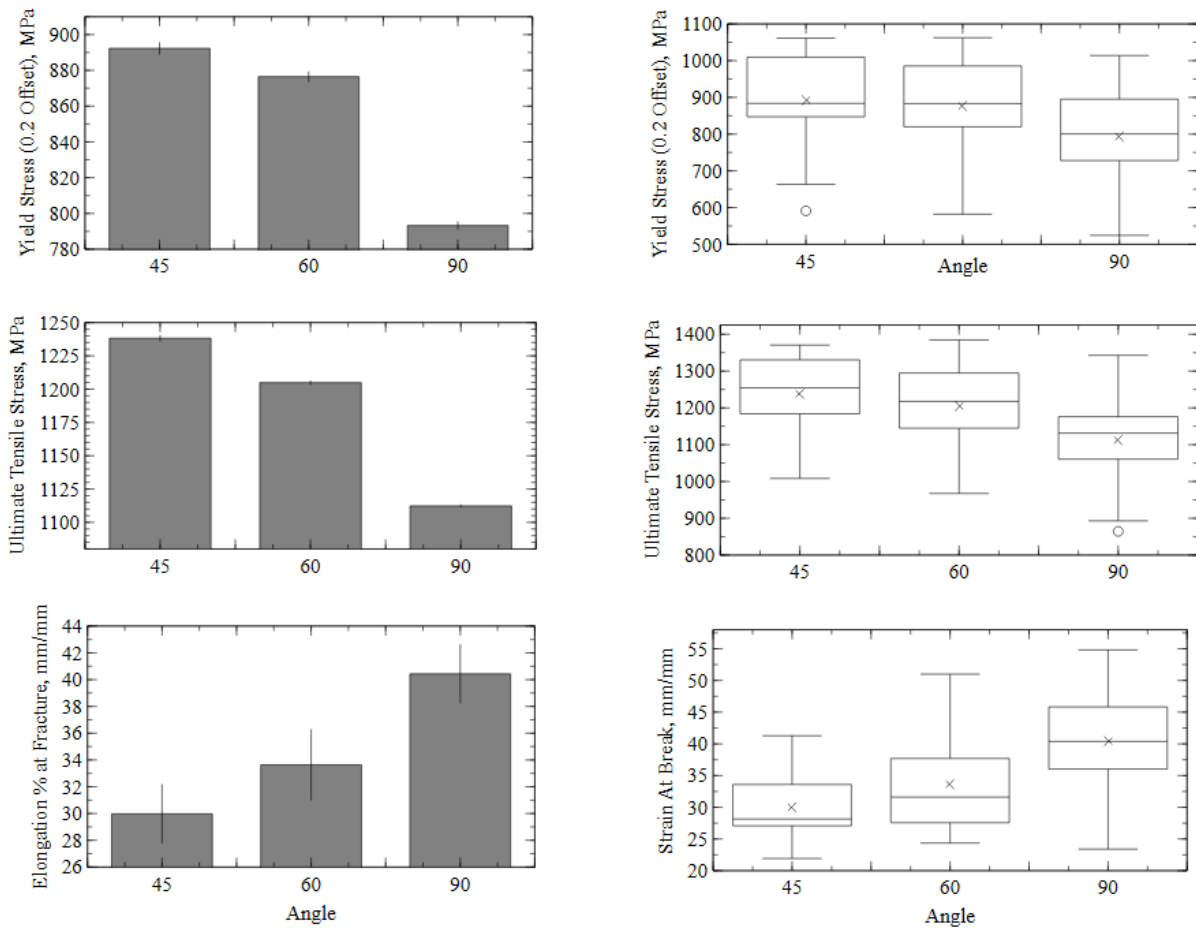
The observed phenomenon of a 90-degree angle exhibits a noteworthy transition, wherein the Concept machine takes the lead, followed by Dual, SLM, EOS M290, Velo, EOS M400, and EOS M280. However, it should be noted that the EOS M400 and M280 machines exhibit reduced capacity in generating builds with elevated tensile strength at this specific angle, potentially posing a significant consideration for specific applications.

Based on the available data, it appears that the Dual and SLM machines exhibit characteristics that make them potentially favorable options for the aforementioned applications, especially when considering angles of 45 and 60 degrees. When considering components

fabricated with a 90-degree orientation, the Concept machine emerges as a potentially superior alternative.

3.1.4 Angle Results

Table 3.9: Angle Tensile Results



The ideal sample—45, 60, or 90 degrees—depends on the particular strength and ductility requirements of the application. Based on the requirement for optimal yield and tensile strength, along with minimal elongation prior to failure, it can be concluded that the 45-degree sample exhibits superior characteristics. This characteristic renders it highly suitable for use in scenarios

where the material requires the ability to withstand deformation when subjected to substantial stress levels. In situations where a trade-off between robustness and adaptability is required, the 60-degree specimen exhibits favorable attributes. It exhibits a satisfactory combination of yield and ultimate tensile strength, while also permitting greater elongation compared to the 45-degree specimen. On the contrary, in the event that the application necessitates utmost ductility, where the material must withstand substantial elongation prior to fracture, the 90-degree specimen emerges as the optimal selection, regardless of its inferior strength characteristics. Hence, the determination of the optimal sample is dependent on the particular performance characteristics that are given priority for the material's intended application.

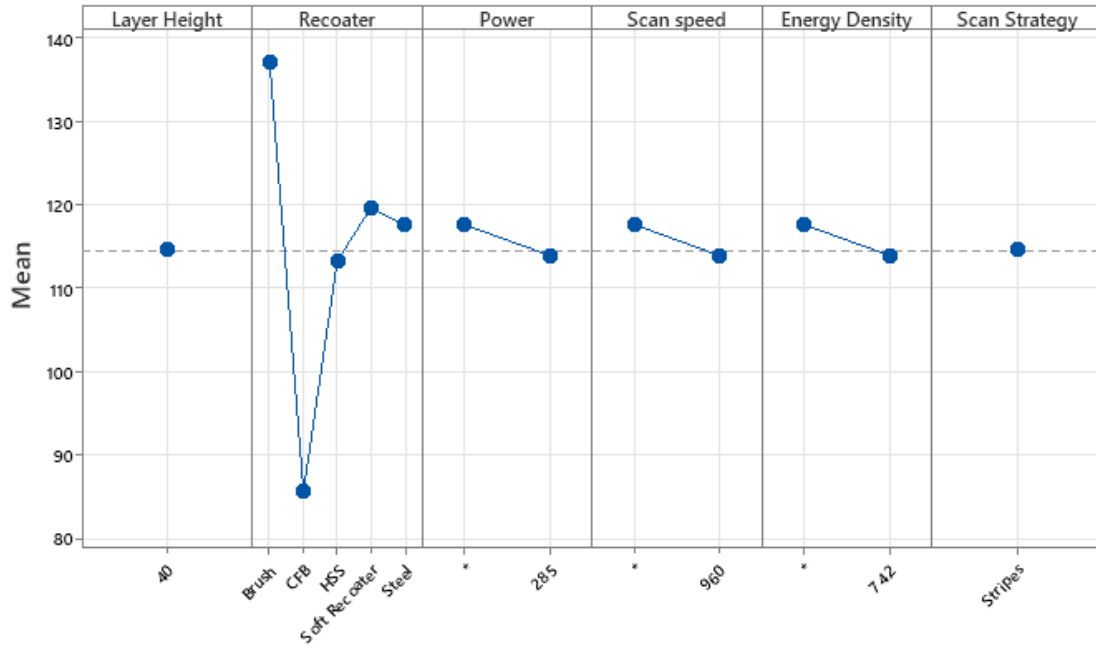
3.1.5 Statistical Analysis

In this study, Minitab, a specialized software designed for statistical analysis, is used to examine the impact of different printing parameters on the mechanical characteristics of the printed object. The focus of the analysis is directed towards the EOS M280 and M290 models, which have been selected based on the supply of extensive testing data that involve various operating parameters. This establishes a solid basis for a comprehensive analysis of the relationship and influence of various factors on the results obtained from these particular printers. The ANOVA main effect plot is utilized in conjunction with various other analytical methods. The plot serves as a valuable instrument for visualizing the primary effects of factors in the analysis, providing lucid insights into the contribution of each variable to the observed changes in the mechanical properties of the builds.

Table 3.10: Main Effect Plots for EOS M280

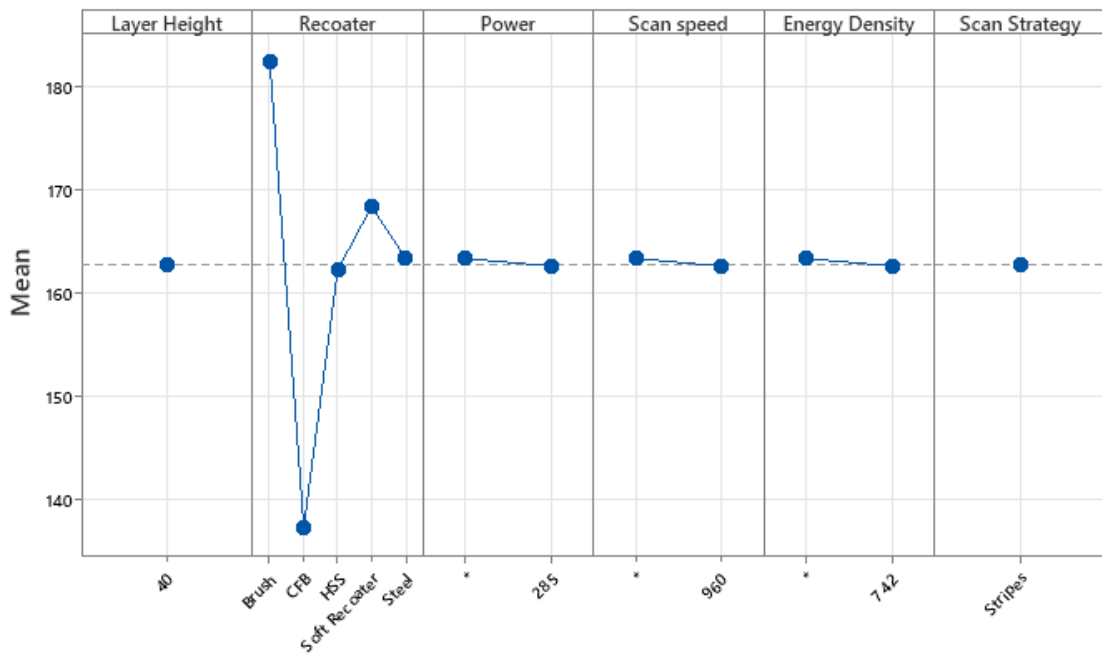
Main Effects Plot for Stress At 0.2% Offset Yield

Data Means

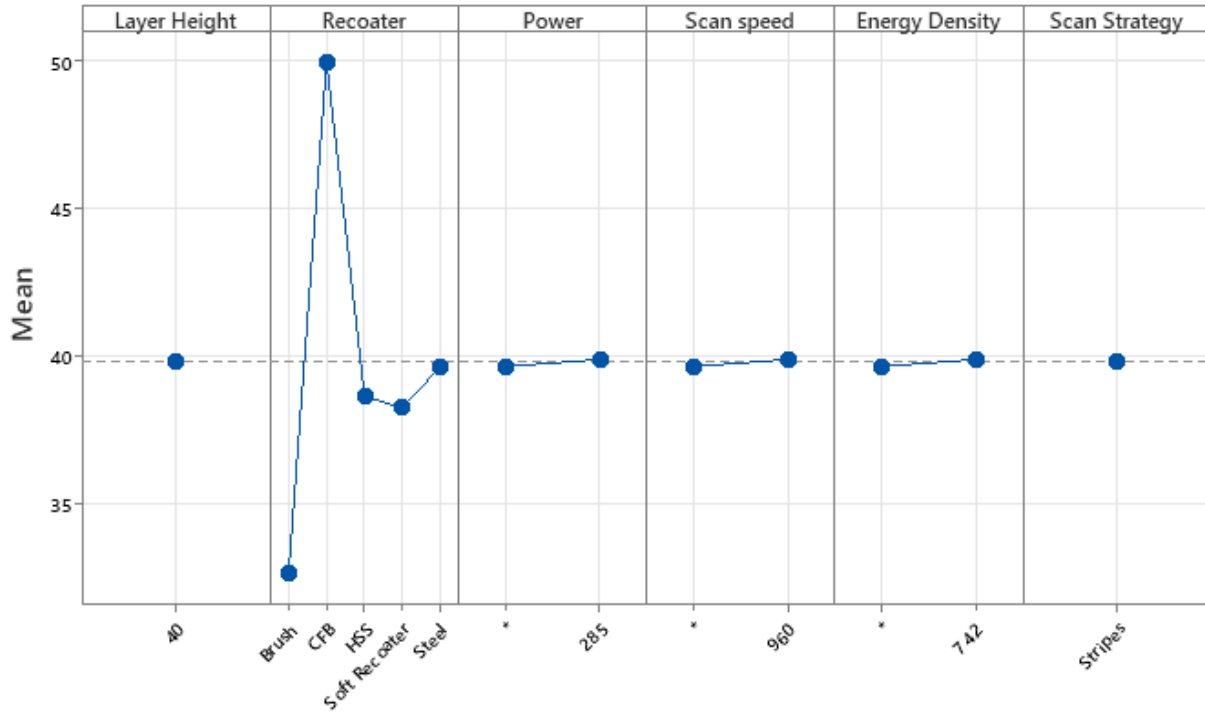


Main Effects Plot for Ultimate Tensile Stress

Data Means



Main Effects Plot for Elongation % at Fracture
Data Means



In the Main Effects Plot for Stress at 0.2% Offset Yield for EOS M280, it can be observed that the Carbon Fiber Brush (CFB) recoater setting exhibits a relationship with an increased average stress level. This suggests that specimens manufactured using the 'CFB' recoater generally exhibit a diminished yield stress. Contrarily, the 'Brush' recoater demonstrates the utmost average stress level, implying its contribution towards an elevated yield stress in the manufactured materials. The previously mentioned variations highlight the recoater category as a significant factor impacting the material's yield strength.

Similarly, it is worth noting that the 'CFB' recoater setting exhibits a correlation with reduced mean stress levels for Ultimate Tensile Stress. Conversely, the 'Brush' recoater setting is associated with elevated mean stress levels. Based on the observed trend, it can be inferred that opting for the 'Brush' recoater setting may be deemed more beneficial in the pursuit of attaining materials exhibiting enhanced tensile strength.

The Main Effects Plot for Elongation % at Fracture indicates that the 'Brush' recoater exhibits the minimum average elongation, implying that the 'Brush' recoater may yield materials with reduced ductility. On the contrary, the 'CFB' recoater exhibits the utmost average elongation, thereby signifying an augmented ductility of the materials fabricated using this configuration. This discovery holds significant importance in scenarios where enhanced ductility and the capacity to undergo deformation without experiencing fracture are sought after.

Based on the analysis of the Main Effects Plots it can be observed that the choice of recoater employed during the manufacturing process exerts a substantial impact on the mechanical properties of the material. The 'CFB' recoater exhibits a tendency to yield lower yields and tensile stresses, while concurrently improving ductility, as indicated by elevated elongation percentages. However, the 'Brush' recoater exhibits favorable characteristics for the production of materials with increased yield and tensile strength, albeit at the expense of reduced ductility. After running the main effect plots, Test for equal variances were employed to understand the average spread of data then used the one-way ANOVA test to look at how the different recoaters impact the results.

The statistical analysis, test for equal variances found in Appendix A, analyzed the stress at a 0.2% offset yield for various recoater types indicates that there is no significant distinction observed among the groups. This conclusion is further supported by the results of the statistical tests. The p-values are 0.509 for the multiple comparisons test and 0.951 for Levene's test, which are both well above the 0.05 threshold, indicating a lack of evidence to reject the null hypothesis of equal variances. The Bonferroni confidence intervals for standard deviations also appear to overlap among the different recoater types, which visually supports the statistical tests' findings. Therefore, the data suggests that the type of recoater does not have a statistically significant impact on the variability of stress at 0.2% offset yield for the EOS M280 model. The one-way ANOVA results show a significant effect of recoater type on stress at 0.2% offset yield, as indicated by a p-value of 0.000. The F-value of 43.30 points to a considerable difference in mean stress values among the groups. With an R-squared value of 76.23%, a substantial portion of the variation in

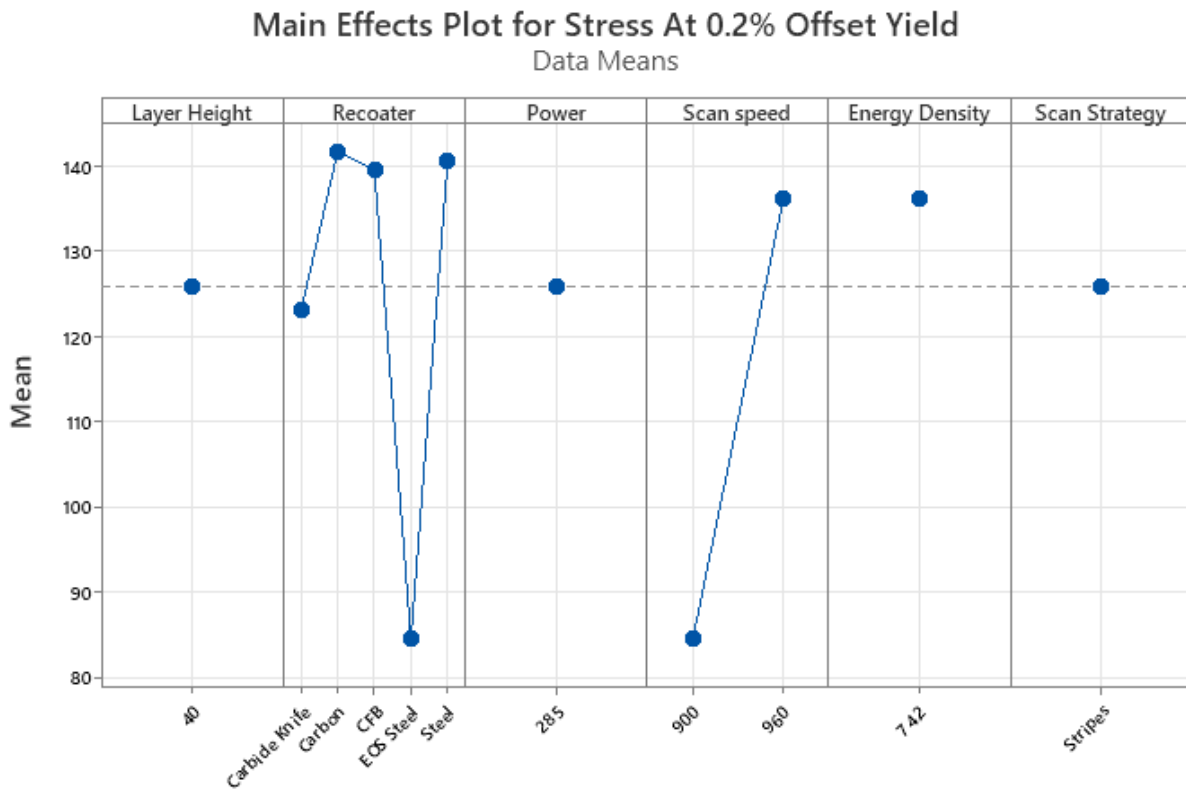
yield stress is explained by the recoater type. The interval plot reinforces these results, displaying varying mean stress levels with distinct confidence intervals for each recoater category.

For ultimate tensile stress variability, the test for equal variances indicates no significant differences between recoater types at a scan speed of 960 mm/s. The multiple comparisons test yields a p-value of 0.728, and Levene's test results in a p-value of 0.938, both of which are much higher than the standard alpha level of 0.05. These high p-values suggest that the null hypothesis—that all variances are equal—cannot be rejected. The 95% Bonferroni confidence intervals for standard deviations, which are meant to provide a more stringent test due to multiple comparisons, also support this conclusion, showing overlap between the intervals for different recoater types. This overlapping indicates that there is no statistically significant difference in the variability of the ultimate tensile stress due to the recoater type under the conditions tested. The one-way ANOVA indicates a significant difference in ultimate tensile stress among the recoater types, with a p-value of 0.000, suggesting the differences are statistically significant. The F-value is 28.91, which is quite high, and shows strong between-group variability in tensile stress. The R-squared value of 67.77% means that over half of the variability in tensile stress can be attributed to the type of recoater used. The interval plot visualizes these differences, with non-overlapping confidence intervals indicating distinct mean stress values for different recoaters.

Test for Equal Variances: Elongation % at Fracture vs Recoater, Scan Speed can be found in appendix A. The statistical analysis examines the variances in elongation percentage at fracture across various recoater types at a consistent scan speed of 960 mm/s, except for the steel recoater with an unknown scanning speed. The p-value for the multiple comparisons test is 0.020, which is below the typical alpha level of 0.05, indicating a statistically significant difference in variance for at least one recoater type. However, Levene's test, with a p-value of 0.118, does not indicate a significant difference in variances. This discrepancy suggests that while one test points to a difference, the overall evidence might not be strong enough to conclusively state that the recoater type affects the variability in elongation at fracture for the EOS M280 model, especially considering the conservative nature of Levene's test. Additionally, the graph showing Bonferroni

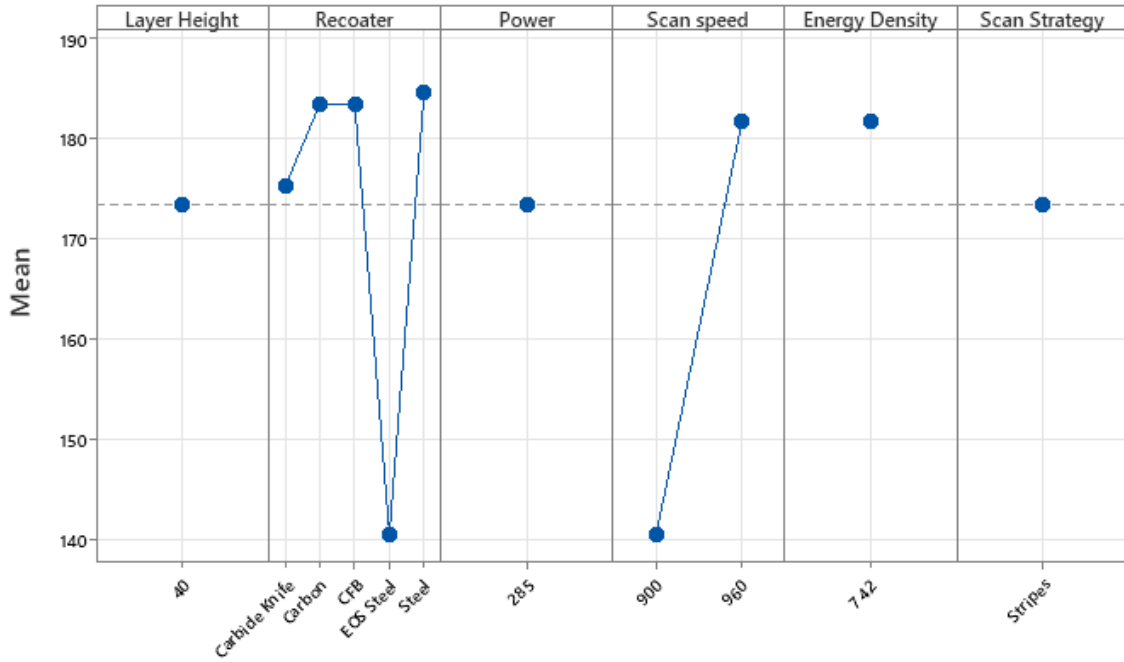
confidence intervals for standard deviations provides a visual representation where overlapping intervals suggest no significant difference, and non-overlapping intervals indicate significant differences between the recoater types of variances. The one-way ANOVA analysis, found in appendix a, revealed significant differences in the elongation at fracture percentages among different recoater types. With a p-value of less than 0.000, the null hypothesis that suggests equal means across groups was rejected. The F-value of 10.95 indicated a substantial variation between the means of the groups. Furthermore, the R-squared value was 44.79%, indicating that nearly half of the variation in elongation percentages could be explained by the choice of recoater. These results underscore the impact of recoater type on material performance.

Table 3.11: Main Effect Plots for EOS M290



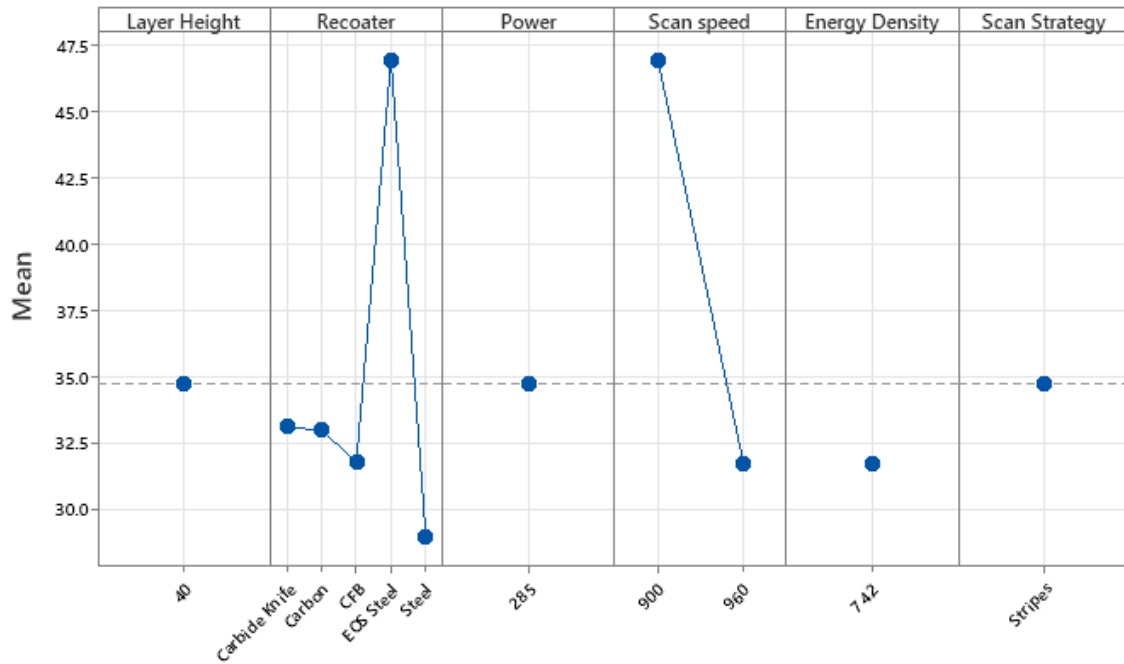
Main Effects Plot for Ultimate Tensile Stress

Data Means



Main Effects Plot for Elongation % at Fracture

Data Means



The recoater types 'CFB', 'Carbon', and 'Steel', as well as the scan speeds of 285 and 960, exhibit higher mean stress levels in relation to the 0.2% Offset Yield Stress. This observation suggests that the mentioned configurations could be optimized to augment the yield strength of the material. On the other hand, the 'EOS Steel' recoater, specifically when operated at a scan speed of 900, exhibits the most minimal average stress level, indicating that it might not be as favorable for attaining elevated yield strength.

In relation to the Ultimate Tensile Stress, the recoaters labeled as 'Carbon', 'CFB', and 'Steel' exhibit a strong correlation with the highest average tensile stress, particularly when operating at scan speeds of 960. This trend suggests that these conditions are favorable to the production of materials exhibiting exceptional tensile strength. On the contrary, the recoater named 'EOS Steel' operating at a scan speed of 900 exhibits the minimum average tensile stress, suggesting that it might be the least optimal configuration for achieving maximum tensile strength.

The plot depicting the Elongation % at Fracture demonstrates that the recoater made of 'EOS Steel' exhibits the most notable average elongation, specifically when operating at a scan speed of 900. This observation implies that this combination is optimal for enhancing ductility. The elevated elongation percentage signifies the material's inherent ability to undergo deformation prior to experiencing fracture, thereby exhibiting a commendable characteristic in numerous applications.

The findings emphasize that the strength properties of the material are influenced favorably by certain recoater types, namely 'CFB', 'Carbon', and 'Steel', as well as the scan speeds. The 'EOS Steel' recoater, however, exhibits lower strength results overall, except in terms of ductility, where it demonstrates exceptional performance.

Test for equal variances for Yield stress, UTS, and elongation can be found in appendix A. The statistical analysis for stress at 0.2% offset yield indicates that there are no significant differences in variances between different recoater types and scanning speeds used in the study. This conclusion is supported by the p-values obtained from both the multiple comparisons test ($p = 0.273$) and the Levene test ($p = 0.719$), both of which are substantially higher than the

conventional significance level of 0.05. Consequently, the data does not provide sufficient evidence to reject the null hypothesis that all variances are equal, suggesting that recoater type and scanning speed do not significantly affect the standard deviation of the stress at 0.2% offset yield. The one-way ANOVA analysis highlights a significant difference in stress at 0.2% offset yield across the different recoater types, as evidenced by a p-value of 0.000. The F-value of 141.11 strongly suggest that the type of recoater significantly affects stress at 0.2% offset yield. This high F-value indicates very pronounced differences among the mean stress levels for the different recoaters. R-squared value is 91.12%, shows that recoater type is a major factor influencing the yield stress.

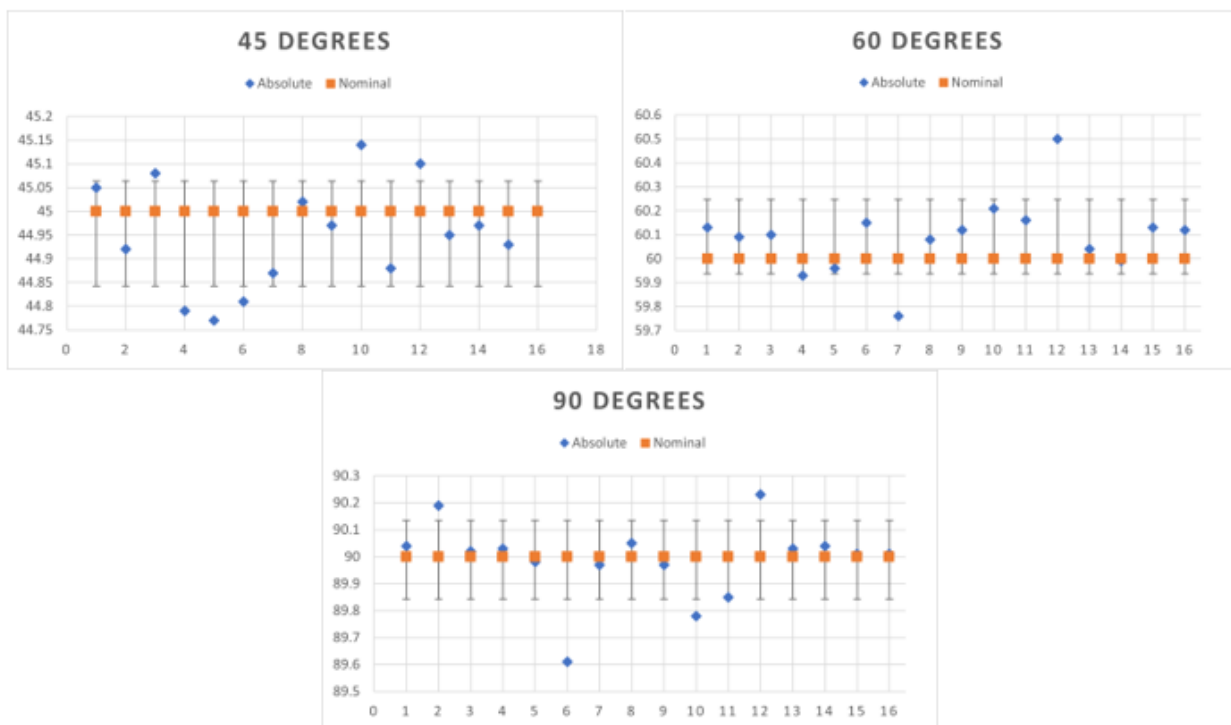
The statistical results for the test on ultimate tensile stress vs recoater type and scan speed, found in appendix A, show that variances across different recoater types are not significantly different. The analysis, which includes both multiple comparisons and Levene's test, yields p-values of 0.260 and 0.734 respectively, both well above the alpha level of 0.05. These results indicate that there is no statistical evidence to suggest that the recoater type and scanning speed have a significant impact on the variability of ultimate tensile stress in the materials tested. The one-way ANOVA test results show a significant variation in ultimate tensile stress among the recoater types with a p-value of 0.000, which is indicative of statistically significant differences. The F-value is 43.50, confirming that the differences between the means are substantial. The R-squared value stands at 75.98%, meaning a large proportion of the variability in tensile stress is attributed to the type of recoater.

The statistical analysis relates to the variability of elongation percentages at fracture across different recoater types and scan speeds. With p-values of 0.384 for the multiple comparisons test and 0.795 for Levene's test, the data does not show any significant differences in variances. Since both p-values are well above the 0.05 threshold, we conclude that there's no statistically significant variance in elongation at fracture attributable to recoater type or scan speed within the parameters tested. The ANOVA results indicate a significant difference in the percentage of elongation at fracture for the various recoater types, with a p-value of 0.000. The F-value is 19.57, which implies

significant differences among the group means. The R-squared value is 58.73%, indicating that this percentage of the variation in elongation at fracture is explained by the different recoater types. The interval plot shows distinct confidence intervals for each recoater, with some not overlapping, suggesting that certain recoater types lead to significantly different elongation percentages.

3.1.6 Comparison of Build Nominal Angle to Measured Absolute Angle

Table 3.12: Absolute Angle vs Nominal Angle



The given dataset presents measurements for a total of 16 samples, encompassing three distinct nominal angles, namely 90 degrees, 60 degrees, and 45 degrees. Within each grouping, the physical (absolute) dimensions exhibit minor deviations from the designated nominal values.

In the case of the 90-degree samples, the observed deviations exhibit a relatively minor magnitude. The maximum positive deviation observed is 0.23 degrees, whereas the maximum negative deviation is -0.39 degrees, suggesting that the fluctuations fall within a comparatively narrow spectrum.

Within the sample set of 60 degrees, the deviations exhibit a relatively negligible magnitude. The most prominent positive deviation amounts to 0.5 degrees, while the most substantial negative deviation stands at -0.24 degrees. Significantly, the specimen exhibiting a 0.5-degree positive deviation emerges as the most prominent singular disparity.

Finally, the samples at 45-degree angle exhibit variations spanning from a reduction of 0.23 degrees to an augmentation of 0.14 degrees. In this case, the deviations exhibit a higher level of precision when compared to the 60-degree set, with the maximum deviation amounting to a mere 0.23 degrees below the designated nominal value. In general, the data suggests a consistent and precise measurement procedure, with all variations falling within a half-degree range of the expected values.

3.1.7 Fractography

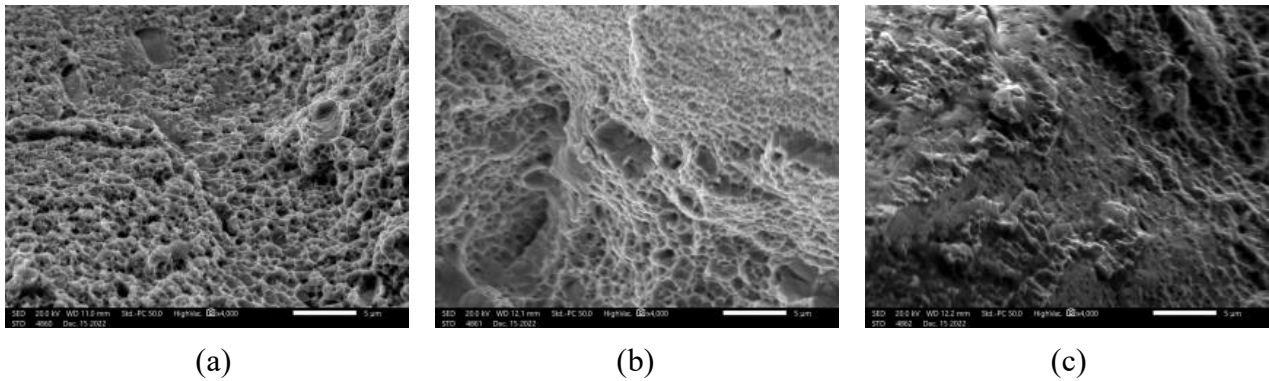


Figure 3.2: Plate 7 (a) 45-degree build (b) 60-degree build (c) 90-degree build

ID	Machine Model Type	Layer Height (μm)	Recoater Type	Power (W)	Scan Speed (mm/s)	Energy Density (J/mm ³)	Core Scan Strategy
7	Concept M2	30	Rubber	180	600	95.2	Checked

Low

45 Elongation % at Fracture	60 Elongation % at Fracture	90 Elongation % at Fracture
27.8125	24.5625	27

High:

45 UTS, MPA	60 UTS, MPA	90 UTS, MPA
1305.133929	1285.604408	1207.245006

High:

45 Yield Stress (0.2% offset), MPA	60 Yield Stress (0.2% offset), MPA	90 Yield Stress (0.2% offset), MPA
885.29232	888.670772	843.768387

At the angle of 45 degrees (a), shown in figure 3.2, the sample exhibits a moderate elongation and displays the highest Ultimate Tensile Strength. The presence of characteristics of ductile fracture, such as the formation of dimples, suggests that the material underwent plastic deformation prior to failure.

The sample at a 60-degree angle (b) demonstrates a low elongation percentage and a slightly reduced ultimate tensile strength (UTS) compared to the sample at a 45-degree angle. The fractographic analysis reveals a reduced number of ductile characteristics compared to the 45-degree sample. Instead, it exhibits a more brittle visual aspect, characterized by flat fracture surfaces and signs of cleavage planes.

At a 90-degree angle (c), the elongation percentage is comparable to that of the 45-degree sample, but with the lowest ultimate tensile strength (UTS). Consequently, the scanning electron microscope (SEM) images may exhibit a combination of ductile and brittle characteristics. The existence of voids and certain planar regions may suggest the occurrence of a fracture involving a combination of modes.

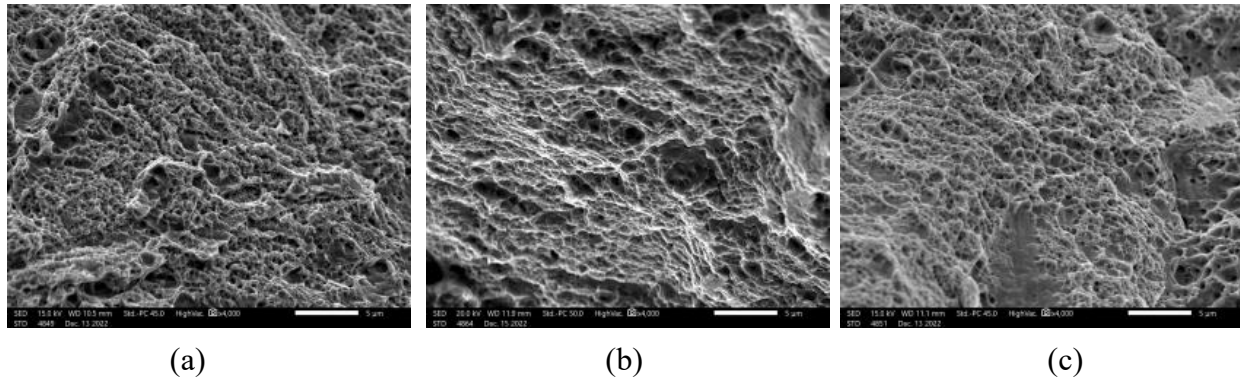


Figure 3.3: Plate 9 (a) 45-degree build (b) 60-degree build (c) 90-degree build

ID	Machine Model Type	Layer Height (μm)	Recoater Type	Power (W)	Scan Speed (mm/s)	Energy Density (J/mm^3)	Core Scan Strategy
9	EOS M290	40	EOS Steel	285	900	-	Stripes

Highest:

45 Elongation % at Fracture	60 Elongation % at Fracture	90 Elongation % at Fracture
41.25	45.13	54.44

Lowest:

45 UTS, MPA	60 UTS, MPA	90 UTS, MPA
1011.35	1001.50	893.03

Lowest:

45 Yield Stress (0.2% offset), MPA	60 Yield Stress (0.2% offset), MPA	90 Yield Stress (0.2% offset), MPA

591.10	604.24	549.65
--------	--------	--------

The fractograph under examination displays features that are indicative of a material experiencing ductile failure. The observed well-defined dimple patterns and the high elongation percentage at fracture indicate that the material experienced substantial plastic deformation prior to reaching its failure point. This observed pattern is characteristic of materials possessing the ability to absorb significant amounts of energy and demonstrate substantial elongation prior to reaching the point of ultimate failure.

In relation to the low values of ultimate tensile stress and yield stress, the fractograph exhibits a deficiency in characteristics commonly associated with brittle or high-energy failure modes. These characteristics would typically manifest as a more granular or faceted appearance, with less observable evidence of plastic deformation. On the contrary, the fracture surface is predominantly characterized by dimple rupture, thereby validating the occurrence of failure subsequent to the material attaining its comparably diminished ultimate tensile strength and yield strength, subsequent to extensive plastic deformation.

The observed low ultimate tensile strength and yield strength values of this Inconel 718 sample indicate that the material is prone to initiating plastic deformation at relatively lower stress levels. This behavior aligns with the extensive and uniformly distributed dimple patterns observed on the fractograph. The fracture surface might not display the rough or jagged features typically observed in materials with greater strength, which is indicative of the reduced energy release during the fracture mechanism.

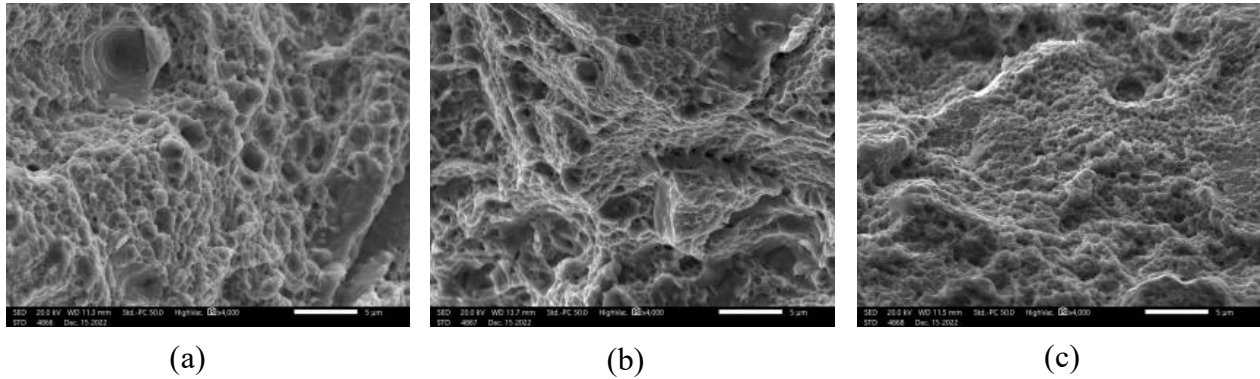


Figure 3.4: Plate 10 (a) 45-degree build (b) 60-degree build (c) 90-degree build

ID	Machine Model Type	Layer Height (μm)	Recoater Type	Power (W)	Scan Speed (mm/s)	Energy Density (J/mm ³)	Core Scan Strategy
10	SLM 280	30	Silicone	200	900	61.7	Stripes

Low:

45 Elongation % at Fracture	60 Elongation % at Fracture	90 Elongation % at Fracture
21.9375	25.875	35.625

High:

45 UTS, MPA	60 UTS, MPA	90 UTS, MPA
1369.789916	1351.03606	1175.770244

High:

45 Yield Stress (0.2% offset), MPA	60 Yield Stress (0.2% offset), MPA	90 Yield Stress (0.2% offset), MPA
1061.058009	1052.249902	934.555666

Figure (a) from plate 11 shows a dimpled pattern on the fracture surface suggests ductile failure. The sample shows high yield stress and high UTS while having a low elongation %,

suggesting that the material is robust and may tolerate a lot of stress before yielding and eventually collapsing. The low elongation indicates that the material cracked soon after yielding, yet the dimples show some plastic deformation. The material's high strength may be attributed to the existence of a fine grain structure.

From figure (b), plate 11, the longer dimples in this sample indicate that it experienced greater plastic deformation prior to failure, which is consistent with the higher elongation %. In comparison to sample (a) at 45 degrees, the yield stress and UTS were lower, suggesting that the material started to deform at lower stresses and could not support as much load before collapsing. The orientation of microstructural elements such as inclusions or grains may have lined up during deformation to produce the elongated dimples.

Figure (c) experienced the greatest plastic deformation, as indicated by the highest elongation %, due to its comparatively smooth fracture surface with fewer identifiable characteristics. The material yielded and deformed more readily than samples (a) and (b), as evidenced by the lower UTS and yield stress. A more ductile phase may have contributed to the smoother texture by giving the material more time to deform plastically and show necking before breaking.

Sample (a), at 45 degrees shows the least amount of plastic deformation prior to fracture (low elongation), but it is the strongest in terms of resistance to deformation (high yield stress and UTS). Sample (b) at 60 degrees experienced greater plastic deformation prior to breaking than sample a meaning a higher elongation, but it is weaker than with a lower yield stress and UTS.

Out of the three, sample (c) at 90 degrees has the highest ductility and can withstand the greatest plastic deformation (maximum elongation); yet it possesses the lowest strength (lowest yield stress and UTS).

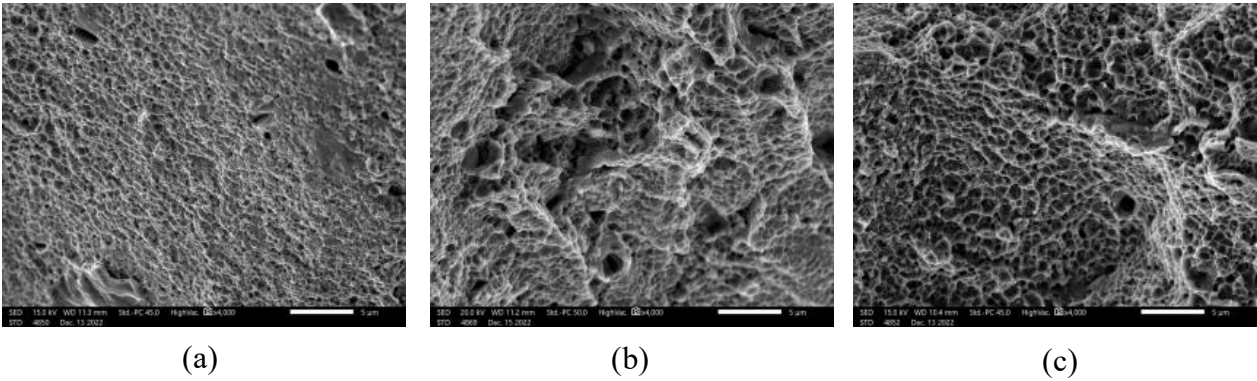


Figure 3.5: Plate 11 (a) 45-degree build (b) 60-degree build (c) 90-degree build

ID	Machine Model Type	Layer Height (μm)	Recoater Type	Power (W)	Scan Speed (mm/s)	Energy Density (J/mm ³)	Core Scan Strategy
11	SLM 280-Dual	30	Silicone	200	900	61.7	Stripes

Low:

45 Elongation % at Fracture	60 Elongation % at Fracture	90 Elongation % at Fracture
23.19	26.88	36.31

High:

45 UTS, MPA	60 UTS, MPA	90 UTS, MPA
1370.65	1385.49	1176.82

High:

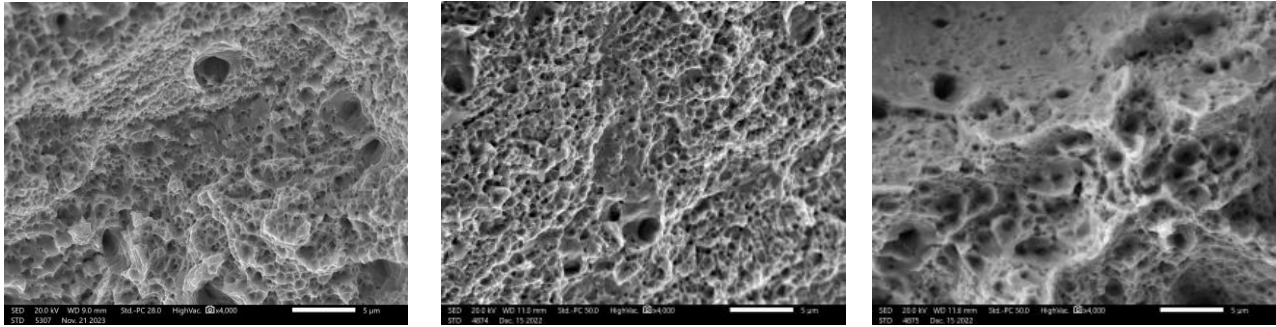
45 Yield Stress (0.2% offset), MPA	60 Yield Stress (0.2% offset), MPA	90 Yield Stress (0.2% offset), MPA
1029	1062.30	900.82

The fractograph (a) exhibits a surface that is relatively smooth, displaying a certain level of granularity. This characteristic is typically observed in materials with low elongation, suggesting their ductile nature. Nevertheless, the material's notable UTS and yield stress properties indicate its capacity to endure substantial stress prior to failure. Additionally, the sleek appearance of the fractograph may imply that the fracture transpired in a relatively brittle manner, regardless of its high strength. This form of a fracture surface is frequently attributed to the quick propagation of cracks, accompanied by limited plastic deformation at the microscopic scale. The existence of small voids and pores may arise from material imperfections or serve as nucleation sites for crack initiation. The presence of a generally uniform surface with granular characteristics suggests that the material experienced a certain level of plastic deformation. This is supported by the observation of localized microvoid coalescence. However, the extent of plastic deformation appears to be limited, as the material ultimately failed in a brittle manner. This behavior is somewhat unusual for materials that possess high elongation properties.

Fractograph (b) exhibits a fractograph characterized by a significantly irregular and coarse surface, which is commonly observed in the case of a ductile fracture. The key attributes involve the presence of dimpled rupture characteristics, wherein the round, elongated dimples serve as indicators of substantial plastic deformation before the fracture. The observed morphology frequently manifests in materials subjected to significant stress and strain, facilitating the initiation, expansion, and merging of voids. This aligns with the characteristics of a material that has undergone substantial elongation. The observed dimples exhibit variations in both size and depth, indicating potential discrepancies in the local microstructure or stress distribution throughout the fracture event. The overall surface characteristics exhibit a rough and uneven texture, devoid of any smooth or uniform regions, thereby emphasizing the ductile behavior observed during the

material's structural failure. The intricacy and depth of the indentations may serve as an indication of the material's toughness, as a fracture of this nature is capable of absorbing a greater amount of energy prior to experiencing failure.

Much like sample (b), the fractograph of (c) showcases a densely packed and non-uniform texture, characterized by small-scale features that indicate a fracture occurrence with restricted plastic deformation. The surface exhibits the presence of diminutive depressions and cavities, which are indicative of micro void coalescence. Nevertheless, the observed dimples exhibit a relatively shallow and densely distributed morphology, suggesting a limited extent of plastic deformation prior to the occurrence of structural failure. The lack of larger dimples or extensive stretching and necking on the surface suggests that the material exhibits relatively low ductility. The observed fracture surface lacks the typical rough and fibrous texture typically found in materials with high ductility, and it also does not exhibit the smooth and flat planes commonly associated with brittle fracture. This implies that the material exhibits properties that lie between the two fracture modes, or that the material's ductile phase was of relatively short duration prior to fracture initiation.



(a)

(b)

(c)

Figure 3.6: Plate 15 (a) 45-degree build (b) 60-degree build (c) 90-degree build

ID	Machine Model Type	Layer Height (μm)	Recoater Type	Power (W)	Scan Speed (mm/s)	Energy Density (J/mm ³)	Core Scan Strategy
15	EOS M280	40	Carbon Fiber Brush	285	960	74.2	Stripes

High:

45 Elongation % at Fracture	60 Elongation % at Fracture	90 Elongation % at Fracture
41.69	50.88	57.38

Low:

45 UTS, MPA	60 UTS, MPA	90 UTS, MPA
1008.31	967.63	864.38

Low:

45 Yield Stress (0.2% offset), MPA	60 Yield Stress (0.2% offset), MPA	90 Yield Stress (0.2% offset), MPA
663.30	581.99	524.35

Sample (a) exhibited notable elongation at a 45-degree angle, as indicated by the presence of dimples, which signifies substantial plastic deformation. Indicating that the specimen exhibits great toughness and possesses the capacity to absorb a large amount of energy prior to experiencing failure, as is common for materials displaying ductile characteristics. The observed low UTS and yield strength of the sample indicate that it possesses a relatively low resistance to

deformation and failure, requiring only a minimal stress level to initiate such processes. The observed fractograph exhibits a lack of brittle characteristics such as cleavage planes, typically prevalent in materials possessing elevated yield strength and ultimate tensile strength, yet diminished elongation properties. The existence of multiple, precisely defined depressions suggests that the material underwent significant plastic deformation. The formation of dimples can be attributed to the phenomenon of micro void coalescence [134], which involves the growth and merging of voids within the material during the process of material elongation. Certain micro voids exhibit varying dimensions, indicating potential disparities in the stress distribution or the existence of inclusions serving as stress amplifiers.

Sample (b) at 60 degrees, in accordance with the material's characteristics of high elongation and low UTS and yield stress, the fractograph shows a prominent ductile fracture pattern with numerous dimples, indicating extensive plastic deformation prior to failure. The presence of different dimple sizes displays a dimpled surface appearance created by micro void coalescence [135] under tensile stress, thereby validating the material's ability to effectively absorb significant energy by means of plastic deformation. The observed behavior indicates a higher ductility in comparison to the previous specimen, supporting the material's reduced yield and fracture strength, as well as its increased elongation prior to reaching the point of failure.

The fractograph (c) at 90 degrees, exhibits a prominently dimpled surface topography, suggesting the sample possesses exceptional elongation characteristics. Furthermore, it is evident that the sample has experienced substantial plastic deformation prior to reaching its ultimate failure point. The presence of significant and deep dimples implies that the material exhibited notable capacity for elongation, aligning with its characteristic of high elongation. The analysis of the fractograph indicates the presence of a concentrated group of dimples, which serves as an indication of the location experiencing the highest levels of stress and strain. This particular region is highly likely to be the site where necking occurred. This phenomenon is distinguished by the progression of micro voids undergoing a transformation into larger voids that subsequently merge together. Certain dimples display an elongated configuration, reflecting the directional strain

encountered during necking as the material undergoes uniaxial stretching. The surface characteristics of the dimples indicate the manifestation of plastic deformation commonly observed in necking, wherein the material undergoes elongation and reduction in thickness until failure occurs. The observed fractograph, particularly when taking into account the sample's features of notable increased elongation and decreased ultimate tensile stress and yield stress in comparison to prior samples, validates the occurrence of substantial plastic deformation accompanied by prominent necking prior to failure. This distinctive characteristic is commonly observed in highly ductile metals subjected to tensile loading.

3.1.8 Metallographic Analysis

As previously stated, Plate 9 demonstrates a notable characteristic by showcasing one of the most elevated elongation percentages in walls inclined at angles of 45, 60, and 90 degrees. Nevertheless, it is imperative to acknowledge that this particular specimen exhibits the most inferior values in terms of ultimate tensile strength and yield stress when compared to the other specimens subjected to testing. The observed contrast highlights a distinctive mechanical property behavior exhibited by the samples in its reaction to varying stress orientations. Figure 3.7 shows the polished samples for plate 9 along with the highlighted porosity for each angle.

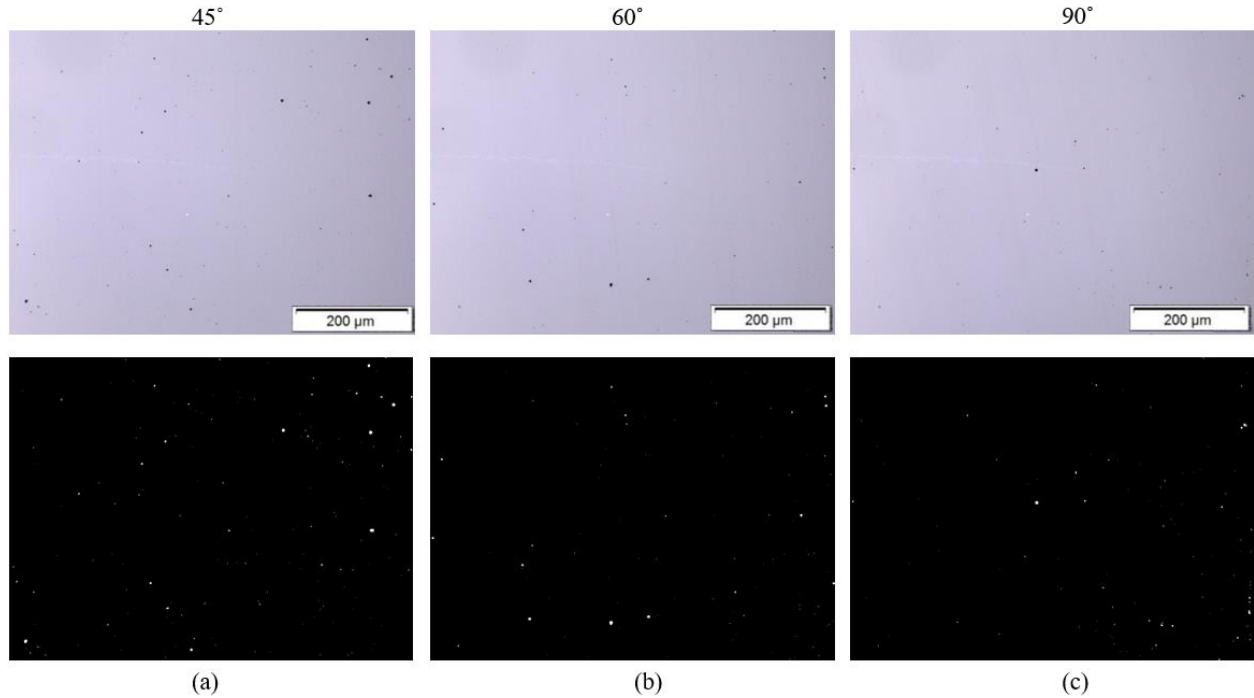


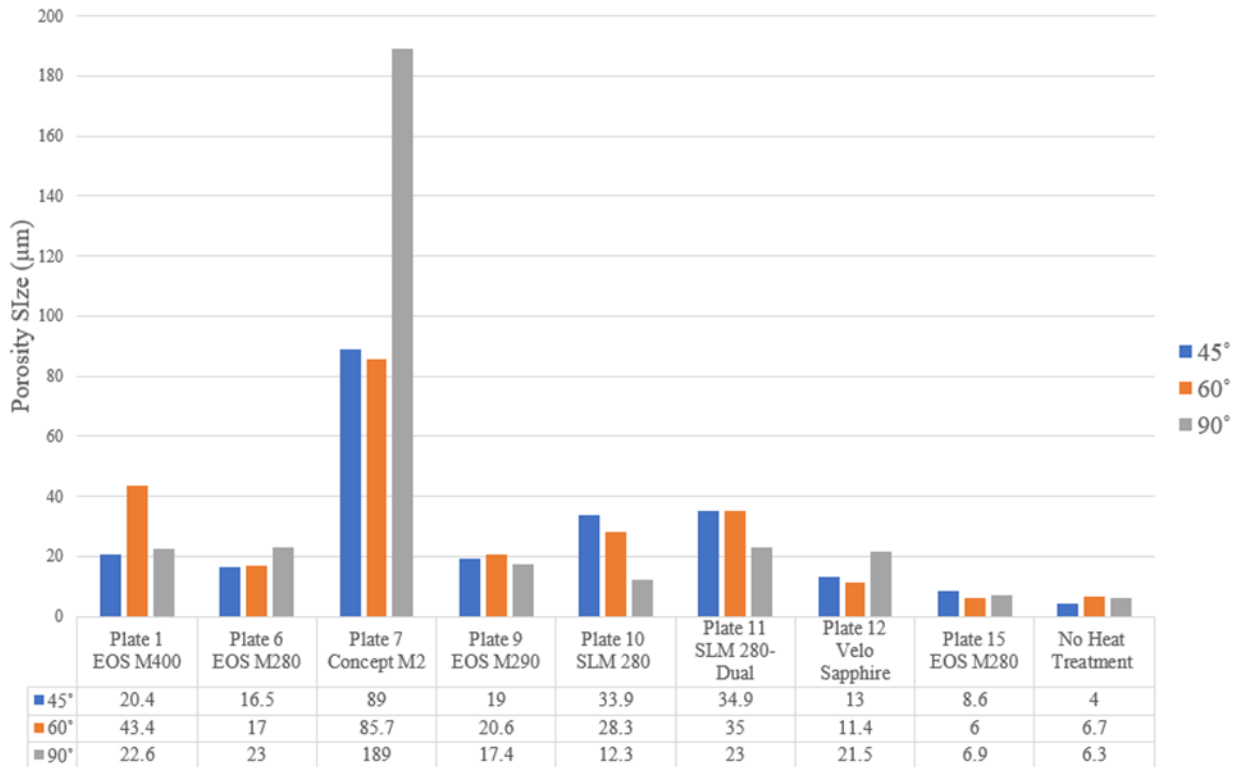
Figure 3.7: Plate 9 polished and porosity analysis (a) 45° (b) 60° (c) 90°

The analysis of porosity percentage area was performed utilizing the ImageJ software, an advanced tool designed for image analysis. The examination findings indicate that the investigated area demonstrates a porosity of approximately .11%. The porosity under consideration exhibits pores with an average diameter of approximately 19 micrometers for sample at 45 degrees (a).

In the sample examined of 60 degrees (b), the porosity size exhibited a consistent behavior, maintaining an average value of approximately 20 microns throughout the entire area. Nevertheless, a reduction in the porous area was observed, exhibiting a decline to a value of .06%.

The analysis of the sample of 90 degrees (c), indicated a reduction in the size of porosity to 17 microns, accompanied by a decrease in the porosity percentage within the area to .068%. This signifies a decrease in porosity by .05% when compared to the 45-degree sample. Appendix B includes images of polished samples and porosity measurements.

Table 3.13: Average Porosity Size



Based on table 3.14, it is evident that Plate 7, produced by the Concept M2 machine, has the highest porosity size among all the plates and machines shown, particularly at the 90° build angle, where the porosity size reaches 189 µm. This value is significantly higher than any other porosity size reported on the chart for any build angle or equipment type. Variations in porosity sizes for the plates produced by different machines at different build angles (45°, 60°, and 90°) are observed. It is important to note that the porosity sizes for each machine and build angle do not display a clear pattern that would indicate a direct correlation between the build angle and the porosity size. Plate 15 with EOS M280 and the 'No Heat Treatment' category show similar porosity sizes across all three angles, suggesting little to no influence of the build angle on porosity size in these cases.

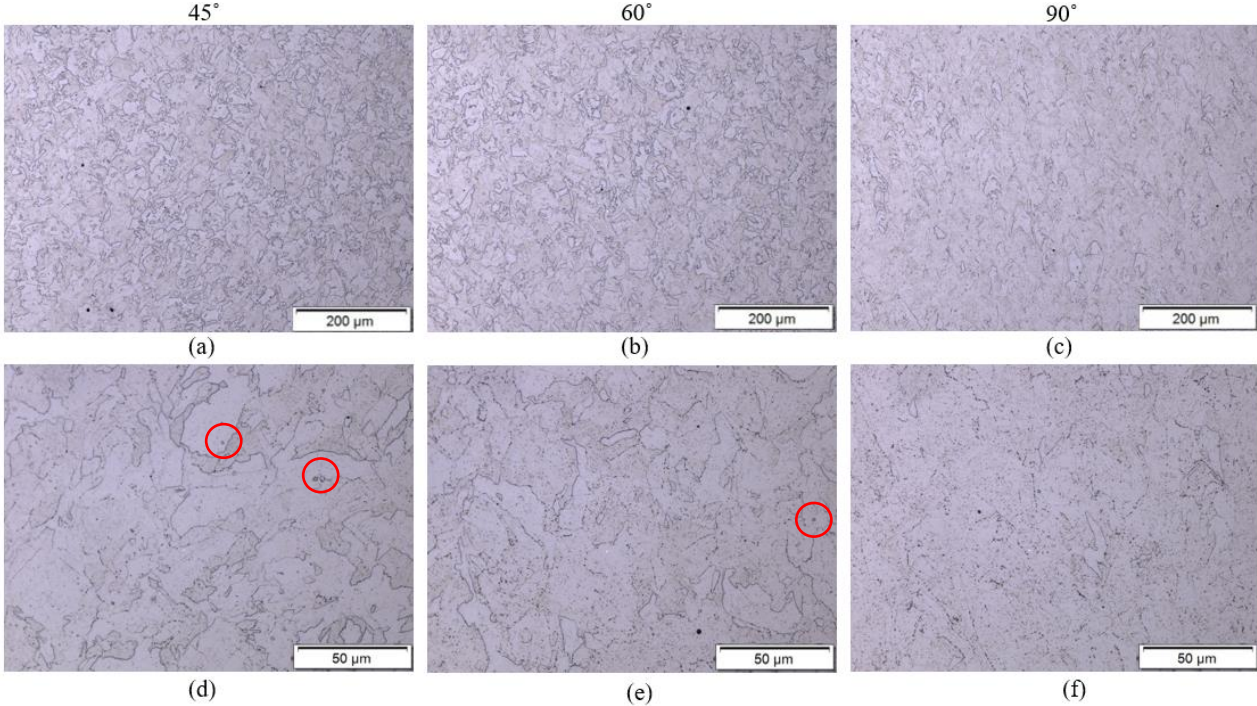


Figure 3.8: Plate 9 microstructures, (a) 45° sample at 200 μm (b) 60° sample at 200 μm (c) 90° sample at 200 μm (d) 45° sample at 50 μm (e) 60° sample at 50 μm (f) 60° sample at 50 μm

The line intercept method was used to determine the grain count inside the designated region using the ASTM E112-13 [137] guidelines. Plate 9, sample 45 (d) underwent the implementation of this method utilizing ImageJ software, which facilitated the determination of an average grain size measuring 29 microns. The sample's etched microstructure, in 45 degrees orientation shown in Figure (a), shows equiaxed grains with well-defined carbides in the circled areas. These carbides are rich in nickel (Ni) and titanium (Ti), exhibiting gray and pink colors, respectively.

Following, the analysis of the sample at a 60-degrees, as depicted in figure (b), demonstrates a visible augmentation in the size of the grains. The analysis has verified an

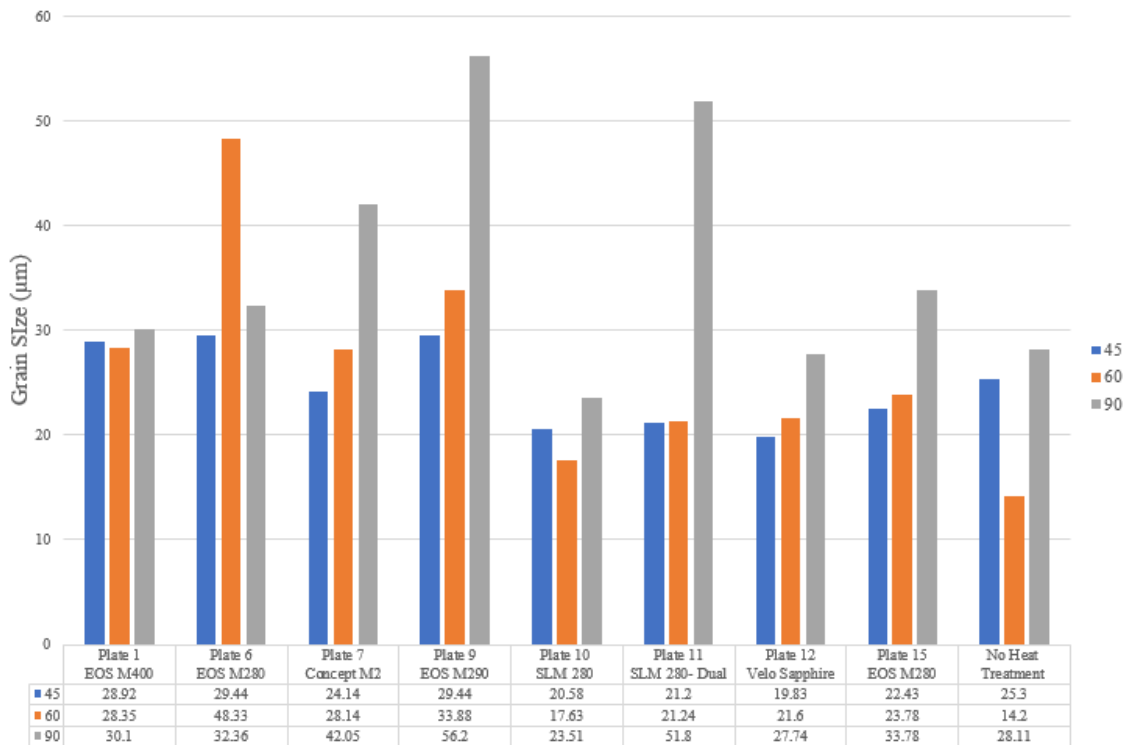
increase in the dimensions of the grain to a magnitude of 33.9 microns. This sample also exhibits the presence of carbides and supplementary precipitates in the grain boundaries.

In image (c), the sample is depicted at a 90-degree orientation, revealing a decrease in grain visibility and an increase in the concentration of precipitates along the grain boundaries.

The mean grain size within this specific orientation is approximately 66 micrometers.

Additionally, the microstructural analysis indicates a significant presence of directional characteristics and elongation within the grain structures, which are in alignment with the sample's build direction.

Table 3.14: Average Grain Size



Based on observations made across various machines, it can be concluded that the 90° build angle exhibits the largest grain size. The observation remains consistent across Plates 1, 7, 9, 10, 11, 12, and 15, along with the plate denoted as 'No Heat Treatment'. This observation

implies that the vertical build orientation may promote the formation of larger grains that are commonly associated with this specific build orientation. Plate 6, which has been manufactured utilizing the EOS M280, exhibits an anomaly within this pattern. The maximum grain size for this plate is documented to be observed at the build angle of 60° , as opposed to 90° . This observation highlights that although a pattern can be noticed, there are instances that deviate from it. It is observed that a 90° angle typically exhibits larger grain sizes. However, it is important to note that the extent of variation in grain sizes among different angles is not uniformly consistent across all plates and machines. The disparity in grain size between angles for Plate 7, manufactured using Concept M2, exhibits a significant contrast, whereas Plate 1, produced by EOS M400, showcases relatively closer grain sizes across all angles.

Materials with smaller grains typically exhibit distinct mechanical properties due to the influence of grain size. When it comes to elongation or ductility, smaller grains often result in lower ductility. This reduction in ductility is attributed to the increased number of grain boundaries present in fine-grained materials, which act as barriers to dislocation movement, an essential mechanism in plastic deformation. Conversely, materials with larger grains tend to exhibit higher ductility due to fewer grain boundaries, allowing for easier dislocation movement. However, the ultimate tensile strength and yield stress of a material are different. Small grains lead to an increase in both UTS and yield stress. The numerous grain boundaries in these materials provide significant resistance to dislocation movement, thereby enhancing the

material's overall strength. In contrast, larger grains, with their fewer grain boundaries, usually result in lower UTS and yield stress, as there is less impediment to dislocation movement.

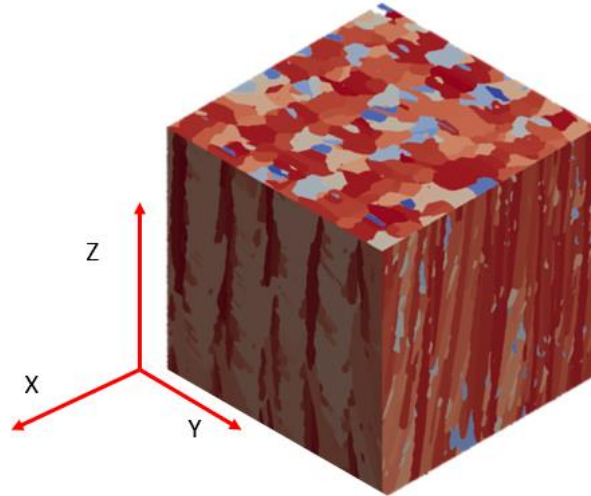


Figure 3.9: Grain Morphology View

Figure 3.9 presents a clear depiction of the grain boundary distribution. In every sample oriented at 90 degrees, the presence of the ZY phase is evident, accounting for the observable elongation in all samples. Conversely, the samples examined at 45-degree angles showcase equiaxed grains, a characteristic typical of the XY orientation, a trait also observed in the 60-degree build samples.

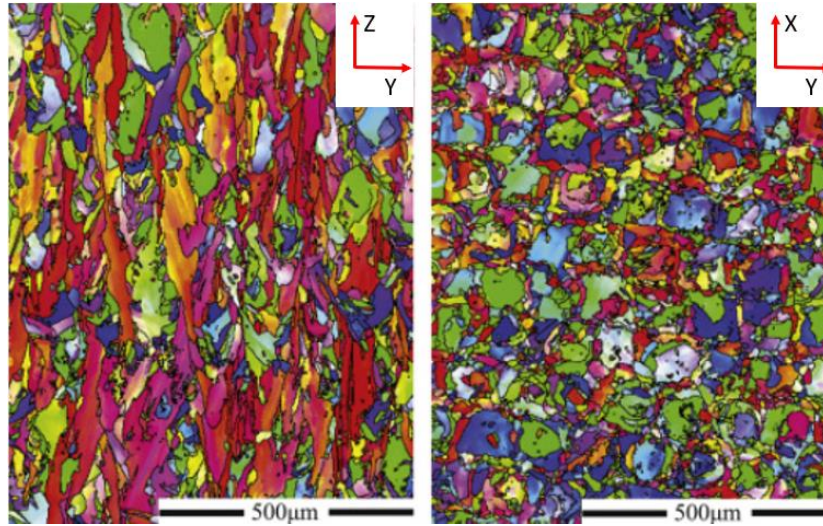


Figure 3.10: Inverse pole figure (IPF) color mappings and the corresponding IPFs of (a) vertically built and (b) horizontally built as-manufactured sample [138].

Supporting the grain morphology view figure, the color mappings in figure 3.10 display the grains morphology seen in all samples at 45, 60, and 90 degrees. This visualization is essential for comprehending the material's structural characteristics from different angular perspectives, illustrating how the grain patterns and orientations vary with each angle. The utilization of color mappings significantly enhances the visibility of these variations, offering a detailed and thorough portrayal of the grain morphology in all the examined samples.

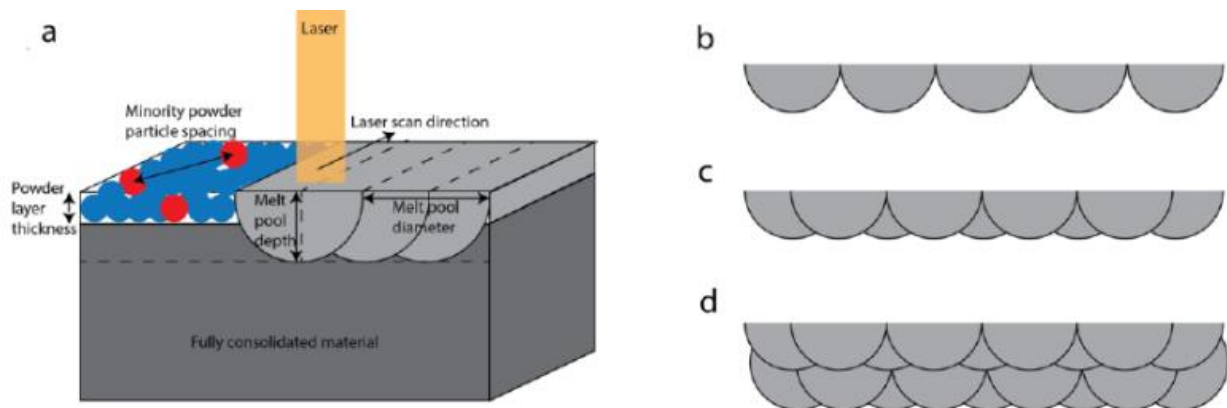


Figure 3.11: a) schematic illustration of L-PBF process showing overlap of melt pools and remelting of previously deposited layers, b-d) deconvolution of melting and mixing process used in the model [136].

In the Laser Powder Bed Fusion process, the formation of molten pools holds a vital role in the fabrication of a structurally sound three-dimensional entity. The laser system is designed to emit a highly concentrated beam of thermal energy, which is then used to selectively induce localized melting of the powder material in specific regions. The application of thermal energy raises the temperature of the powder material to a level at which it undergoes a phase transition, resulting in the creation of a small molten area commonly referred to as a melt pool. Upon the moving of the laser, the melt pool experiences fast cooling and solidification, thereby yielding a compact and consolidated layer that fuses with the adjacent and underlying material. The LPBF procedure continues by repeatedly depositing the next layers of powder material, which are subsequently melted by the laser. This laser-induced melting may also cause re-melting of certain regions within the underlying layer, thereby guaranteeing robust interlayer adhesion. The selection of the geometry of these melt pools, which plays a vital role in achieving the desired final density and structural integrity of the part, is contingent upon the adjustment of several process parameters. The parameters include laser power, scan speed, beam focus, and the thermal properties of the powder. The optimization of these parameters is of utmost importance in the management of the overlap of melt pools and the attainment of the desired microstructure and material properties in the final product.

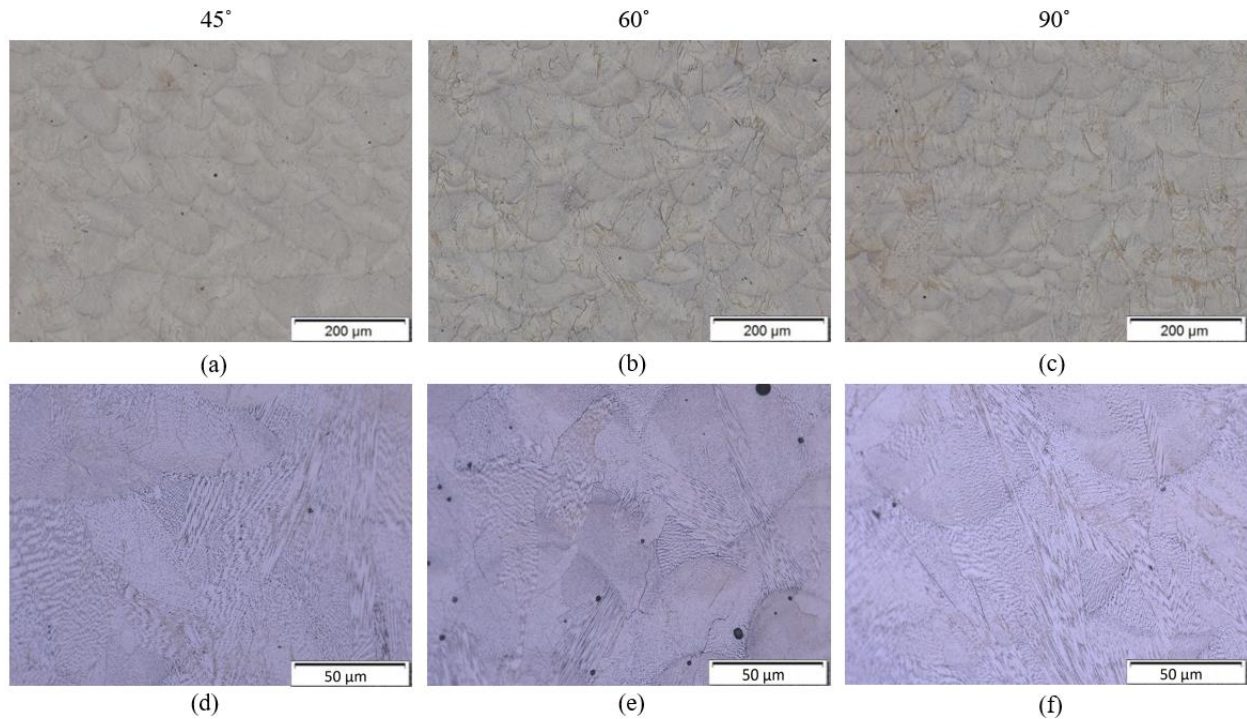


Figure 3.12: As built plate (a) 45° sample at 200 μm (b) 60° sample at 200 μm (c) 90° sample at 200 μm (d) 45° sample at 50 μm (e) 60° sample at 50 μm (f) 60° sample at 50 μm

In figure 3.12 (a-c), the images show distinct melt pool boundaries - the hallmark of the layer-wise construction process. Within these melt pools, we can often observe columnar grains that have grown perpendicular to the pool boundaries, indicating the direction of heat transfer. The variation in microstructure across different areas of the melt pool is indicative of the thermal gradients experienced during the process. The overall heterogeneity in the microstructure is characteristic of the rapid solidification inherent to additive manufacturing and has a direct impact on the mechanical properties of the material.

Upon examining images at 50 μm , the intricate details within the melt pools are much more pronounced. The fine dendritic structures within the melt pools are visible, demonstrating the rapid solidification phenomena characteristic of additive manufacturing. Figure 3.12 (d-f) allows to discern the primary and potentially secondary dendritic arms, with the former indicating the primary direction of heat extraction. Micro-segregation is also apparent in the interdendritic regions, where alloying elements may concentrate, potentially forming secondary phases. Porosity

becomes more noticeable at this magnification, visible as small spherical voids that could be detrimental to the mechanical performance. The higher magnification also allows for the observation of contrast variations within the solidified metal, which may signify different crystal orientations or phases, crucial for understanding the material's behavior. Samples at 45 and 60 degrees follow the grain size pattern as the previously mentioned samples. However, the sample at 90 degrees does not have strong distinctive grain boundaries to measure but follows the directionality expected for this build orientation. The melt pool dimensions across the three samples depicted in Figures 3.12 (a-c) exhibit consistent sizing, with the average diameter of the melt pools measuring approximately 106 microns.

Chapter 4: Conclusion

A few mechanical characteristics that additive manufacturing machines provide the materials they create include yield stress, elongation % at fracture, and ultimate tensile stress. These are essential factors to consider when assessing the machines' performance. Based on these characteristics, every machine has its advantages and best applications.

The Dual and SLM machines are appropriate for high-strength applications where builds must bear substantial loads because of their proven ability to produce materials with high yield stress and UTS. Their reduced elongation percentages, however, imply that the builds they generate are less ductile, which could restrict their applicability in situations where deformation and flexibility are necessary.

Conversely, the Concept machine is notable for its effectiveness when built at a 90-degree angle. While yield stress isn't particularly improved, it performs well in UTS, suggesting it can create strong materials under tension. It also provides more ductility, which benefits applications requiring strength and flexibility. This is demonstrated by its higher elongation % at fracture in vertical constructions.

The M290, M400, and M280 are among the EOS machines with a balanced profile. The EOS M290 and M400 are flexible options for a variety of applications because of their strong yield stress and ductility. The EOS M280 exhibits strong ductility while having a lower yield stress, which could be better in some situations where material flexibility is more important than ultimate strength.

On the other hand, the Velo machine shows lower yield stress, UTS, and elongation %, suggesting that it is less competent across all measured mechanical parameters. This indicates that

it would be better suited for non-critical applications or could require process enhancements as it creates materials that are neither as strong nor as ductile as those produced by the other machines.

In conclusion, the final product's particular mechanical requirements should be considered when choosing an additive manufacturing machine. In cases when ductility is not as important as strength, the Dual and SLM machines are good choices. Perhaps the ideal choice for components that need to be both flexible and strong, particularly in vertical positions, is the Concept machine. In situations where a compromise between ductility and strength is required, the EOS M290 and M400 are viable competitors. Lastly, the Velo machine could be used for less demanding applications or would need more work to improve the material quality.

Analysis was performed on Minitab software to perform a statistical analysis on the impact of different printing parameters on the mechanical properties of objects printed using EOS M280 and M290 models. A variety of operating parameters were considered, thanks to the substantial amount of testing data available for these models. The main effect plots and other statistical methods, including ANOVA, provided clear insights into how each variable influenced the mechanical properties.

For the EOS M280 the use of different recoaters significantly affects the mechanical properties of the materials produced. Specifically, the Carbon Fiber Brush (CFB) recoater tends to result in materials with lower yield and tensile stresses, suggesting a decrease in material strength, but with increased ductility as shown by higher elongation at fracture percentages. On the other hand, the Brush recoater is associated with higher yield and tensile stresses, indicating stronger materials, but with reduced ductility. The statistical tests confirm these differences with significant p-values ($p < 0.000$) for both yield stress and ultimate tensile stress, and an R-squared value of 76.23% for yield stress and 67.77% for tensile stress, highlighting the strong influence of the

recoater type. However, the test for equal variances shows no significant difference in the spread of data across recoater types for yield stress and ultimate tensile stress, with p-values well above the 0.05 threshold.

Similarly, with the EOS M290, the type of recoater and scan speeds used notably influence the mechanical properties. The 'CFB', 'Carbon', and 'Steel' recoaters at higher scan speeds are conducive to higher yield and tensile strengths, whereas the 'EOS Steel' recoater at a scan speed of 900 exhibits lower strength yet enhanced ductility. The ANOVA test results for the EOS M290 demonstrate significant differences in yield stress (p-value of 0.000, F-value of 141.11, R-squared of 91.12%) and ultimate tensile stress (p-value of 0.000, F-value of 43.50, R-squared of 75.98%), indicating that the recoater type significantly affects these properties. However, the test for equal variances indicates no significant difference in the variability of these properties across different recoater types and scan speeds, with all p-values exceeding the 0.05 significance level.

In conclusion, while the tests for equal variances suggest that the variability of mechanical properties does not differ significantly across recoater types and scan speeds, the one-way ANOVA results clearly show that the choice of recoater has a substantial impact on the yield stress, ultimate tensile stress, and elongation at fracture. These findings are crucial for optimizing the 3D printing process to achieve desired material properties by selecting the appropriate recoater type.

The analysis of the porosity and grain size in various plates produced by different machines reveals notable findings. Plate 7, made by Concept M2 at a 90° build angle, stands out with the largest porosity size of 189 μm , a value significantly larger than those from other plates and build angles. While variations in porosity sizes and build angles are seen across different machines, no consistent pattern directly correlates build angle with porosity size. The 90° build angle generally corresponds to the largest grain size across multiple plates, and the 'No Heat Treatment' Plate

suggests a tendency for vertical build orientations to foster larger grains. However, exceptions like Plate 6, produced by EOS M280, deviate from this pattern, exhibiting a maximum grain size at a 60° angle. These observations indicate that while trends exist in grain and porosity size relative to build angle and machine type, they are not universally consistent, underscoring the complexity of the relationship between these factors in additive manufacturing processes.

References

- [1] Najmon, Joel C., Sajjad Raesi, and Andres Tovar. “2 - Review of Additive Manufacturing Technologies and Applications in the Aerospace Industry.” In *Additive Manufacturing for the Aerospace Industry*, edited by Francis Froes and Rodney Boyer, 7–31. Elsevier, 2019.
<https://doi.org/10.1016/B978-0-12-814062-8.00002-9>.
- [2] Buchanan, C., and L. Gardner. “Metal 3D Printing in Construction: A Review of Methods, Research, Applications, Opportunities and Challenges.” *Engineering Structures* 180 (February 1, 2019): 332–48. <https://doi.org/10.1016/j.engstruct.2018.11.045>.
- [3] Buj-Corral, Irene, Aitor Tejo-Otero, and Felip Fenollosa-Artés. “Development of AM Technologies for Metals in the Sector of Medical Implants.” *Metals* 10, no. 5 (May 2020): 686.
<https://doi.org/10.3390/met10050686>.
- [4] Godec, Damir, Ana Pilipović, Tomislav Breški, Julia Ureña, Olga Jordá, Mario Martínez, Joamin Gonzalez-Gutierrez, Stephan Schuschnigg, José Ramón Blasco, and Luis Portolés. “Introduction to Additive Manufacturing.” In *A Guide to Additive Manufacturing*, edited by Damir Godec, Joamin Gonzalez-Gutierrez, Axel Nordin, Eujin Pei, and Julia Ureña Alcázar, 1–44. Springer Tracts in Additive Manufacturing. Cham: Springer International Publishing, 2022.
https://doi.org/10.1007/978-3-031-05863-9_1.
- [5] Vafadar, Ana, Ferdinando Guzzomi, Alexander Rassau, and Kevin Hayward. “Advances in Metal Additive Manufacturing: A Review of Common Processes, Industrial Applications, and Current Challenges.” *Applied Sciences* 11, no. 3 (January 2021): 1213.
<https://doi.org/10.3390/app11031213>.
- [6] Huang, Yong, Ming C. Leu, Jyoti Mazumder, and Alkan Donmez. “Additive Manufacturing: Current State, Future Potential, Gaps and Needs, and Recommendations.” *Journal of*

Manufacturing Science and Engineering 137, no. 014001 (February 1, 2015).

<https://doi.org/10.1115/1.4028725>.

- [7] Monzón, M. D., Z. Ortega, A. Martínez, and F. Ortega. “Standardization in Additive Manufacturing: Activities Carried out by International Organizations and Projects.” *The International Journal of Advanced Manufacturing Technology* 76, no. 5 (February 1, 2015): 1111–21. <https://doi.org/10.1007/s00170-014-6334-1>.
- [8] Anandan Kumar, Hemnath, and Senthilkumaran Kumaraguru. “Distortion in Metal Additive Manufactured Parts.” In *3D Printing and Additive Manufacturing Technologies*, edited by L. Jyothish Kumar, Pulak M. Pandey, and David Ian Wimpenny, 281–95. Singapore: Springer, 2019. https://doi.org/10.1007/978-981-13-0305-0_24.
- [9] Kok, Y., X. P. Tan, P. Wang, M. L. S. Nai, N. H. Loh, E. Liu, and S. B. Tor. “Anisotropy and Heterogeneity of Microstructure and Mechanical Properties in Metal Additive Manufacturing: A Critical Review.” *Materials & Design* 139 (February 5, 2018): 565–86. <https://doi.org/10.1016/j.matdes.2017.11.021>.
- [10] Seifi, Mohsen, Michael Gorelik, Jess Waller, Nik Hrabe, Nima Shamsaei, Steve Daniewicz, and John J. Lewandowski. “Progress Towards Metal Additive Manufacturing Standardization to Support Qualification and Certification.” *JOM* 69, no. 3 (March 1, 2017): 439–55. <https://doi.org/10.1007/s11837-017-2265-2>.
- [11] Ngo, Tuan D., Alireza Kashani, Gabriele Imbalzano, Kate T. Q. Nguyen, and David Hui. “Additive Manufacturing (3D Printing): A Review of Materials, Methods, Applications and Challenges.” *Composites Part B: Engineering* 143 (June 15, 2018): 172–96. <https://doi.org/10.1016/j.compositesb.2018.02.012>.

- [12] Seifi, Mohsen, Ayman Salem, Jack Beuth, Ola Harrysson, and John J. Lewandowski. “Overview of Materials Qualification Needs for Metal Additive Manufacturing.” *JOM* 68, no. 3 (March 1, 2016): 747–64. <https://doi.org/10.1007/s11837-015-1810-0>.
- [13] Singh, Sunpreet, Seeram Ramakrishna, and Rupinder Singh. “Material Issues in Additive Manufacturing: A Review.” *Journal of Manufacturing Processes* 25 (January 1, 2017): 185–200. <https://doi.org/10.1016/j.jmapro.2016.11.006>.
- [14] Lewandowski, John J., and Mohsen Seifi. “Metal Additive Manufacturing: A Review of Mechanical Properties.” *Annual Review of Materials Research* 46, no. 1 (2016): 151–86. <https://doi.org/10.1146/annurev-matsci-070115-032024>.
- [15] Shapiro, A. A., J. P. Borgonia, Q. N. Chen, R. P. Dillon, B. McEnerney, R. Polit-Casillas, and L. Soloway. “Additive Manufacturing for Aerospace Flight Applications.” *Journal of Spacecraft and Rockets* 53, no. 5 (2016): 952–59. <https://doi.org/10.2514/1.A33544>.
- [16] Herzog, Dirk, Vanessa Seyda, Eric Wycisk, and Claus Emmelmann. “Additive Manufacturing of Metals.” *Acta Materialia* 117 (September 15, 2016): 371–92. <https://doi.org/10.1016/j.actamat.2016.07.019>.
- [17] Bocanegra-Bernal, M. H. “Hot Isostatic Pressing (HIP) Technology and Its Applications to Metals and Ceramics.” *Journal of Materials Science* 39, no. 21 (November 1, 2004): 6399–6420. <https://doi.org/10.1023/B:JMSC.0000044878.11441.90>.
- [18] Atkinson, H. V., and S. Davies. “Fundamental Aspects of Hot Isostatic Pressing: An Overview.” *Metallurgical and Materials Transactions A* 31, no. 12 (December 1, 2000): 2981–3000. <https://doi.org/10.1007/s11661-000-0078-2>.
- [19] Petrovic, Vojislav, Juan Vicente Haro Gonzalez, Olga Jordá Ferrando, Javier Delgado Gordillo, Jose Ramón Blasco Puchades, and Luis Portolés Griñan. “Additive Layered Manufacturing:

Sectors of Industrial Application Shown through Case Studies.” *International Journal of Production Research* 49, no. 4 (February 15, 2011): 1061–79.

<https://doi.org/10.1080/00207540903479786>.

[20] Thomas, Douglas S., and Stanley W. Gilbert. “Costs and Cost Effectiveness of Additive Manufacturing.” National Institute of Standards and Technology, December 2014.

<https://doi.org/10.6028/NIST.SP.1176>.

[21] Walter, Manfred, Jan Holmström, and Hannu Yrjölä. “Rapid Manufacturing and Its Impact on Supply Chain Management.” *Proceedings of Logistics Research Network Annual Conference, Dublin, Ireland*, January 1, 2004.

[22] Gibson, Ian, et al. *Additive Manufacturing Technologies: 3D Printing, Rapid Prototyping, and Direct Digital Manufacturing*. 2nd Edition. Germany, Springer New York, 2014.

[23] Dutta, B., and F. H. (Sam) Froes. “The Additive Manufacturing (AM) of Titanium Alloys.” *Metal Powder Report* 72, no. 2 (March 1, 2017): 96–106.

<https://doi.org/10.1016/j.mprp.2016.12.062>.

[24] Duda, Thomas, and L. Venkat Raghavan. “3D Metal Printing Technology.” *IFAC-PapersOnLine*, 17th IFAC Conference on International Stability, Technology and Culture TECIS 2016, 49, no. 29 (January 1, 2016): 103–10. <https://doi.org/10.1016/j.ifacol.2016.11.111>.

[25] Gibson, Ian, David Rosen, Brent Stucker, and Mahyar Khorasani. “Powder Bed Fusion.” In *Additive Manufacturing Technologies*, edited by Ian Gibson, David Rosen, Brent Stucker, and Mahyar Khorasani, 125–70. 3rd Edition. Cham: Springer International Publishing, 2021.

https://doi.org/10.1007/978-3-030-56127-7_5.

- [26] Shahrubudin, Nurhalida, Lee Te Chuan, and Rohaizan Ramlan. “An Overview on 3D Printing Technology: Technological, Materials, and Applications” 35 (August 15, 2019): 1286–96. <https://doi.org/10.1016/j.promfg.2019.06.089>.
- [27] Tiwari, Sunil Kumar, Sarang Pande, Sanat Agrawal, and Santosh M. Bobade. “Selection of Selective Laser Sintering Materials for Different Applications.” *Rapid Prototyping Journal* 21, no. 6 (2015): 630.
- [28] Jansen, Deniz, Theresa Hanemann, Markus Radek, Astrid Rota, Jörg Schröpfer, and Martin Heilmaier. “Development of Actual Powder Layer Height Depending on Nominal Layer Thicknesses and Selection of Laser Parameters.” *Journal of Materials Processing Technology* 298 (December 1, 2021): 117305. <https://doi.org/10.1016/j.jmatprotec.2021.117305>.
- [29] Caltanissetta, Fabio, Marco Grasso, Stefano Petró, and Bianca Maria Colosimo. “Characterization of In-Situ Measurements Based on Layerwise Imaging in Laser Powder Bed Fusion.” *Additive Manufacturing* 24 (December 1, 2018): 183–99. <https://doi.org/10.1016/j.addma.2018.09.017>.
- [30] Lancaster, Robert, Gareth Davies, Henry Illsley, Spencer Jeffs, and G. Baxter. “Structural Integrity of an Electron Beam Melted Titanium Alloy.” *Materials* 9 (June 14, 2016): 470. <https://doi.org/10.3390/ma9060470>.
- [31] Gaikwad, Aniruddha, Richard Williams, Harry Winton, Benjamin Bevans, Ziyad Smoqi, Prahalada Rao, and Paul Hooper. “Multi Phenomena Melt Pool Sensor Data Fusion for Enhanced Process Monitoring of Laser Powder Bed Fusion Additive Manufacturing.” *Materials & Design* 221 (July 1, 2022): 110919. <https://doi.org/10.1016/j.matdes.2022.110919>.
- [32] Mostafaei, Amir, Cang Zhao, Yining He, Seyed Reza Ghiaasiaan, Bo Shi, Shuai Shao, Nima Shamsaei, et al. “Defects and Anomalies in Powder Bed Fusion Metal Additive Manufacturing.”

Current Opinion in Solid State and Materials Science 26, no. 2 (April 1, 2022): 100974.

<https://doi.org/10.1016/j.cossms.2021.100974>.

- [33] Mahmood, Muhammad Arif, Diana Chioibas, Asif Ur Rehman, Sabin Mihai, and Andrei C. Popescu. “Post-Processing Techniques to Enhance the Quality of Metallic Parts Produced by Additive Manufacturing.” *Metals* 12, no. 1 (January 2022): 77.

<https://doi.org/10.3390/met12010077>.

- [34] Aboulkhair, Nesma T., Marco Simonelli, Luke Parry, Ian Ashcroft, Christopher Tuck, and Richard Hague. “3D Printing of Aluminium Alloys: Additive Manufacturing of Aluminium Alloys Using Selective Laser Melting.” *Progress in Materials Science* 106 (December 1, 2019): 100578. <https://doi.org/10.1016/j.pmatsci.2019.100578>.

- [35] “Residual Stress - an Overview | ScienceDirect Topics.” Accessed October 26, 2023.

<https://www.sciencedirect.com/topics/materials-science/residual-stress>.

- [36] “Residual Stress - Industrial Metallurgists,” September 16, 2016.

<https://www.imetllc.com/residual-stress/>.

- [37] Kim, Felix H, and Shawn P Moylan. “Literature Review of Metal Additive Manufacturing Defects.” Gaithersburg, MD: National Institute of Standards and Technology, May 2018.

<https://doi.org/10.6028/NIST.AMS.100-16>.

- [38] Snell, Robert, Sam Tamas-Williams, Lova Chechik, Alistair Lyle, Everth Hernández-Nava, Charlotte Boig, George Panoutsos, and Iain Todd. “Methods for Rapid Pore Classification in Metal Additive Manufacturing.” *JOM* 72, no. 1 (January 1, 2020): 101–9.

<https://doi.org/10.1007/s11837-019-03761-9>.

- [39] Kim, F. H., S. P. Moylan, E. J. Garboczi, and J. A. Slotwinski. “Investigation of Pore Structure in Cobalt Chrome Additively Manufactured Parts Using X-Ray Computed Tomography and Three-

Dimensional Image Analysis.” *Additive Manufacturing* 17 (October 1, 2017): 23–38.

<https://doi.org/10.1016/j.addma.2017.06.011>.

- [40] Rai, R, J W Elmer, T A Palmer, and T DebRoy. “Heat Transfer and Fluid Flow during Keyhole Mode Laser Welding of Tantalum, Ti–6Al–4V, 304L Stainless Steel and Vanadium.” *Journal of Physics D: Applied Physics* 40, no. 18 (September 21, 2007): 5753–66.

<https://doi.org/10.1088/0022-3727/40/18/037>.

- [50] Metal AM magazine. “How Process Parameters Drive Successful Metal AM Part Production,” June 1, 2018. <https://www.metal-am.com/articles/70927-2/>.

- [51] INSIDE METAL ADDITIVE MANUFACTURING. “Particles Properties Inducing Porosity in Metal AM.” Accessed October 28, 2023.

<http://www.insidemetaladditivemanufacturing.com/1/post/2018/03/particles-properties-inducing-porosity-in-metal-am.html>.

- [52] Kan, Wen Hao, Louis Ngai Sam Chiu, Chao Voon Samuel Lim, Yuman Zhu, Yang Tian, Derui Jiang, and Aijun Huang. “A Critical Review on the Effects of Process-Induced Porosity on the Mechanical Properties of Alloys Fabricated by Laser Powder Bed Fusion.” *Journal of Materials Science* 57, no. 21 (June 1, 2022): 9818–65. <https://doi.org/10.1007/s10853-022-06990-7>.

- [53] Zhang, Bi, Yongtao Li, and Qian Bai. “Defect Formation Mechanisms in Selective Laser Melting: A Review.” *Chinese Journal of Mechanical Engineering* 30, no. 3 (May 1, 2017): 515–27. <https://doi.org/10.1007/s10033-017-0121-5>.

- [54] Balbaa, Mohamed, Sameh Mekhiel, Mohamed Elbestawi, and J. McIsaac. “On Selective Laser Melting of Inconel 718: Densification, Surface Roughness, and Residual Stresses.” *Materials & Design*, May 22, 2020. <https://doi.org/10.1016/j.matdes.2020.108818>.

- [55] Yuasa, Kenya, Masaharu Tagami, Makiko Yonehara, Toshi-Taka Ikeshoji, Koki Takeshita, Hiroshi Aoki, and Hideki Kyogoku. “Influences of Powder Characteristics and Recoating Conditions on Surface Morphology of Powder Bed in Metal Additive Manufacturing.” *The International Journal of Advanced Manufacturing Technology* 115, no. 11 (August 1, 2021): 3919–32. <https://doi.org/10.1007/s00170-021-07359-x>.
- [56] “Powder Bed Layer Characteristics: The Overseen First-Order Process Input | SpringerLink.” <https://link.springer.com/article/10.1007/s11661-016-3470-2>.
- [57] “Powder Bed Layer Characteristics: The Overseen First-Order Process Input | SpringerLink.” <https://link.springer.com/article/10.1007/s11661-016-3470-2>.
- [58] “Electron Beam Additive Manufacturing of Titanium Components: Properties and Performance | J. Manuf. Sci. Eng. | ASME Digital Collection.” Accessed October 28, 2023. https://asmedigitalcollection.asme.org/manufacturingscience/article/135/6/061016/375746/Electron-Beam-Additive-Manufacturing-of-Titanium?casa_token=PhCSE8sQkn4AAAAA:ur7fEEU4w673fzssSAX866b_qdXJTIQeSevkudutMIwmTq2m3MqfIWE6JOoJIIVzeWGVd9g.
- [59] “What Is Electron Beam Melting (EBM)?” Accessed October 28, 2023. <https://markforged.com/resources/learn/3d-printing-basics/3d-printing-processes/what-is-electron-beam-melting-ebm>.
- [60] Nagarajan, Balasubramanian, Zhiheng Hu, Xu Song, Wei Zhai, and Jun Wei. “Development of Micro Selective Laser Melting: The State of the Art and Future Perspectives.” *Engineering* 5, no. 4 (August 1, 2019): 702–20. <https://doi.org/10.1016/j.eng.2019.07.002>.
- [61] Narra, Sneha P. “Powder Bed Fusion – Metals.” In *Encyclopedia of Materials: Metals and Alloys*, 85–94. Elsevier, 2022. <https://doi.org/10.1016/B978-0-12-819726-4.00107-1>.

- [62] Singh, R., S. Singh, and M.S.J. Hashmi. “Implant Materials and Their Processing Technologies.” In *Reference Module in Materials Science and Materials Engineering*, B9780128035818041564. Elsevier, 2016. <https://doi.org/10.1016/B978-0-12-803581-8.04156-4>.
- [63] “EBM Technology | GE Additive.” Accessed October 28, 2023. <https://www.ge.com/additive/ebm>.
- [64] Testbook. “Electron Beam Machining: Diagram, Parts, Working, Applications.” Accessed October 28, 2023. <https://testbook.com/mechanical-engineering/electron-beam-machining-definition-construction-and-types>.
- [65] Samant, Rutuja, and Frank Medina. “Electron Beam Melting: From Powder to Part,” n.d.
- [66] Vock, Silvia, Burghardt Klöden, Alexander Kirchner, Thomas Weißgärber, and Bernd Kieback. “Powders for Powder Bed Fusion: A Review.” *Progress in Additive Manufacturing* 4, no. 4 (December 1, 2019): 383–97. <https://doi.org/10.1007/s40964-019-00078-6>.
- [67] Habiba, Ummay, and Rainer J. Hebert. “Powder Spreading Mechanism in Laser Powder Bed Fusion Additive Manufacturing: Experiments and Computational Approach Using Discrete Element Method.” *Materials* 16, no. 7 (April 2023). <https://doi.org/10.3390/ma16072824>.
- [68] B.a, Praveena, Lokesh N, Abdulrajak Buradi, Santhosh N, Praveena B I, and Vignesh R. “A Comprehensive Review of Emerging Additive Manufacturing (3D Printing Technology): Methods, Materials, Applications, Challenges, Trends and Future Potential.” *Materials Today: Proceedings*, International Conference on Smart and Sustainable Developments in Materials, Manufacturing and Energy Engineering, 52 (January 1, 2022): 1309–13. <https://doi.org/10.1016/j.matpr.2021.11.059>.
- [69] Chowdhury, Sohini, N. Yadaiah, Chander Prakash, Seeram Ramakrishna, Saurav Dixit, Lovi Raj Gupta, and Dharam Buddhi. “Laser Powder Bed Fusion: A State-of-the-Art Review of the

Technology, Materials, Properties & Defects, and Numerical Modelling.” *Journal of Materials Research and Technology* 20 (September 1, 2022): 2109–72.

<https://doi.org/10.1016/j.jmrt.2022.07.121>.

[70] “Inconel 718: A Workhorse Material for Additive Manufacturing.” Accessed October 28, 2023.

<https://www.protolabs.com/resources/blog/inconel-718-a-workhorse-material-for-additive-manufacturing/>.

[71] “Welding of Inconel Alloy 718: A Historical Overview | Semantic Scholar.” Accessed October

28, 2023. <https://www.semanticscholar.org/paper/Welding-of-Inconel-Alloy-718%3A-A-Historical-Overview-Lingenfelter/c12c7786cc12603feba9ba8f686a9517cbf1ce41>.

[72] ResearchGate. “Applications of Nickel Alloy -718.” Accessed October 28, 2023.

https://www.researchgate.net/figure/Applications-of-nickel-alloy-718_tbl2_342269180.

[73] AZoM.com. “Nickel Alloy Inconel 718 - Properties and Applications by United Performance

Metals,” November 14, 2008. <https://www.azom.com/article.aspx?ArticleID=4459>.

[74] “Chromium (Cr) - Chemical Properties, Health and Environmental Effects.” Accessed October

28, 2023. <https://www.lenntech.com/periodic/elements/cr.htm>.

[75] “Iron (Fe) - Properties, Applications.” Accessed October 28, 2023.

<https://www.azom.com/article.aspx?ArticleID=9094>.

[76] “Molybdenum (Mo) - Chemical Properties, Health and Environmental Effects.” Accessed

October 28, 2023. <https://www.lenntech.com/periodic/elements/mo.htm>.

[77] “Niobium (Nb) - Chemical Properties, Health and Environmental Effects.” Accessed October 28,

2023. <https://www.lenntech.com/periodic/elements/nb.htm>.

[78] Ghasemi-Tabasi, Hossein, Charlotte de Formanoir, Steven Van Petegem, Jamasp Jhabvala, Samy

Hocine, Eric Boillat, Navid Sohrabi, et al. “Direct Observation of Crack Formation Mechanisms

with Operando Laser Powder Bed Fusion X-Ray Imaging.” *Additive Manufacturing* 51 (March 1, 2022): 102619. <https://doi.org/10.1016/j.addma.2022.102619>.

[79] Ghasemi-Tabasi, Hossein, Charlotte de Formanoir, Steven Van Petegem, Jamasp Jhabvala, Samy Hocine, Eric Boillat, Navid Sohrabi, et al. “Direct Observation of Crack Formation Mechanisms with Operando Laser Powder Bed Fusion X-Ray Imaging.” *Additive Manufacturing* 51 (March 1, 2022): 102619. <https://doi.org/10.1016/j.addma.2022.102619>.

[80] Hooper, Paul A. “Melt Pool Temperature and Cooling Rates in Laser Powder Bed Fusion.” *Additive Manufacturing* 22 (August 1, 2018): 548–59. <https://doi.org/10.1016/j.addma.2018.05.032>.

[81] Tran, Hai T., and Albert C. To. “Cracking Prediction at Solid-Tooth Support Interface during Laser Powder Bed Fusion Additive Manufacturing.” *Journal of Science: Advanced Materials and Devices* 8, no. 4 (December 1, 2023): 100615. <https://doi.org/10.1016/j.jsamd.2023.100615>.

[82] Jiang, Jingchao, Xun Xu, and Jonathan Stringer. “Support Structures for Additive Manufacturing: A Review.” *Journal of Manufacturing and Materials Processing* 2, no. 4 (December 2018): 64. <https://doi.org/10.3390/jmmp2040064>.

[83] Boswell, John H., Daniel Clark, Wei Li, and Moataz M. Attallah. “Cracking during Thermal Post-Processing of Laser Powder Bed Fabricated CM247LC Ni-Superalloy.” *Materials & Design* 174 (July 15, 2019): 107793. <https://doi.org/10.1016/j.matdes.2019.107793>.

[84] Zhao, Cang, Kamel Fezzaa, Ross W. Cunningham, Haidan Wen, Francesco De Carlo, Lianyi Chen, Anthony D. Rollett, and Tao Sun. “Real-Time Monitoring of Laser Powder Bed Fusion Process Using High-Speed X-Ray Imaging and Diffraction.” *Scientific Reports* 7, no. 1 (June 15, 2017): 3602. <https://doi.org/10.1038/s41598-017-03761-2>.

- [85] Yin, Jie, Dengzhi Wang, Liangliang Yang, Huiliang Wei, Peng Dong, Linda Ke, Guoqing Wang, Haihong Zhu, and Xiaoyan Zeng. “Correlation between Forming Quality and Spatter Dynamics in Laser Powder Bed Fusion.” *Additive Manufacturing* 31 (January 1, 2020): 100958. <https://doi.org/10.1016/j.addma.2019.100958>.
- [86] Yin, Jie, Dengzhi Wang, Liangliang Yang, Huiliang Wei, Peng Dong, Linda Ke, Guoqing Wang, Haihong Zhu, and Xiaoyan Zeng. “Correlation between Forming Quality and Spatter Dynamics in Laser Powder Bed Fusion.” *Additive Manufacturing* 31 (January 1, 2020): 100958. <https://doi.org/10.1016/j.addma.2019.100958>.
- [87] Lindström, Viktor, Giandomenico Lupo, Jian Yang, Vladyslav Turlo, and Christian Leinenbach. “A Simple Scaling Model for Balling Defect Formation during Laser Powder Bed Fusion.” *Additive Manufacturing* 63 (February 5, 2023): 103431. <https://doi.org/10.1016/j.addma.2023.103431>.
- [88] Aboulkhair, Nesma, Nicola Everitt, Ian Ashcroft, and Christopher Tuck. “Reducing Porosity in AlSi10Mg Parts Processed by Selective Laser Melting.” *Additive Manufacturing* 1–4 (August 1, 2014). <https://doi.org/10.1016/j.addma.2014.08.001>.
- [89] Metal AM magazine. “Residual Stress in AM Can Cause Major Build Failures: How to Prevent It,” December 1, 2018. <https://www.metal-am.com/articles/how-residual-stress-can-cause-major-build-failures-in-3d-printing/>.
- [90] Li, C., Z. Y. Liu, X. Y. Fang, and Y. B. Guo. “Residual Stress in Metal Additive Manufacturing.” *Procedia CIRP*, 4th CIRP Conference on Surface Integrity (CSI 2018), 71 (January 1, 2018): 348–53. <https://doi.org/10.1016/j.procir.2018.05.039>.

- [91] V, Carlota. "Post-Processing Trends Report Reveals Current Methods and Challenges." 3Dnatives, September 2, 2020. <https://www.3dnatives.com/en/postprocess-trends-2020-020920204/>.
- [92] Ahmed, Farid, Usman Ali, Dyuti Sarker, Ehsan Marzbanrad, Kaylie Choi, Yahya Mahmoodkhani, and Ehsan Toyserkani. "Study of Powder Recycling and Its Effect on Printed Parts during Laser Powder-Bed Fusion of 17-4 PH Stainless Steel." *Journal of Materials Processing Technology* 278 (April 1, 2020): 116522. <https://doi.org/10.1016/j.jmatprotec.2019.116522>.
- [93] Solukon. "Powder Removal in Additive Manufacturing: Solukon Survey." Accessed October 30, 2023. <https://www.solukon.de/en/news/the-challenges-of-manual-powder-removal-in-additive-manufacturing/>.
- [94] Rapid 3D. "3D Printing Post-Processing - Powder Removal and Cleaning." Accessed October 30, 2023. <https://rapid3d.co.za/3d-printing-post-processing-cleaning/>.
- [95] "Stress Relieving on Metal Products - Heat Treatment - Bodycote Plc." Accessed October 30, 2023. <https://www.bodycote.com/services/heat-treatment/stress-relieving/>.
- [96] "Postprocessing Steps and Costs for Metal 3D Printing," October 24, 2023. <https://www.additivemanufacturing.media/articles/postprocessing-steps-and-costs-for-metal-3d-printing>.
- [97] Carrozza, Alessandro, Alberta Aversa, Federico Mazzucato, Emilio Bassini, Diego Manfredi, Sara Biamino, Anna Valente, and Paolo Fino. "An Investigation on the Effect of Different Multi-Step Heat Treatments on the Microstructure, Texture and Mechanical Properties of the DED-Produced Ti-6Al-4V Alloy." *Materials Characterization* 189 (July 1, 2022): 111958. <https://doi.org/10.1016/j.matchar.2022.111958>.

- [98] MakerVerse. “The Guide to Laser Powder Bed Fusion (L-PBF) Post Processing.” Accessed October 30, 2023. <https://www.makerverse.ai/metal-3d-printing/the-guide-to-laser-powder-bed-fusion-%28l-pbf%29-post-processing>.
- [99] Zhang, Jiong, Qiqiang Cao, and Wen Feng Lu. “A Review on Design and Removal of Support Structures in Metal Additive Manufacturing.” *Materials Today: Proceedings*, The International Conference on Additive Manufacturing for a Better World (AMBW 2022), 70 (January 1, 2022): 407–11. <https://doi.org/10.1016/j.matpr.2022.09.277>.
- [100] Metal AM magazine. “Hot Isostatic Pressing: Improving Quality and Performance in AM,” December 1, 2015. <https://www.metal-am.com/articles/hot-isostatic-pressing-improving-quality-and-performance-in-3d-printing/>.
- [101] “Isostatic Pressing.” Accessed October 30, 2023. <https://www.mpif.org/IntrotoPM/Processes/IsostaticPressing.aspx>.
- [102] Muley, A V & Aravindan, S. & Singh, I.P.. (2015). Nano and hybrid aluminum-based metal matrix composites: An overview. *Manufacturing Review*. 2. 15. 10.1051/mfreview/2015018.
- [103] Ferreri, Nicholas C., Sven C. Vogel, and Marko Knezevic. “Determining Volume Fractions of γ , Γ' , Γ'' , δ , and MC-Carbide Phases in Inconel 718 as a Function of Its Processing History Using an Advanced Neutron Diffraction Procedure.” *Materials Science and Engineering: A* 781 (April 20, 2020): 139228. <https://doi.org/10.1016/j.msea.2020.139228>.
- [104] “What Is Annealing? A Complete Process Guide.” Accessed October 30, 2023. <https://www.twi-global.com/technical-knowledge/faqs/what-is-annealing.aspx>.
- [105] Bambhania, Haresh. “What Is Annealing?- Definition, Process, And Stages.” *Engineering Choice* (blog), April 17, 2021. <https://www.engineeringchoice.com/what-is-annealing/>.

- [106] “What Is Metal Aging? | Metal Supermarkets.” Accessed October 30, 2023.
<https://www.metalsupermarkets.com/what-is-metal-aging/>.
- [107] Aston, 20 Kent Road, and Pa 19014 877.846.7628. “Quenching Heat Treated Metals.” L&L Special Furnace Co, Inc., July 30, 2020. <https://lffurnace.com/blog/quenching-heat-treated-metals/>.
- [108] Fractory. “Quenching Explained – Definition, Process, Benefits and More,” March 24, 2023.
<http://https%253A%252F%252Ffractory.com%252Fquenching-explained%252F>.
- [109] “Quenching Heat Treatment | Specialty Steel Treating.” Accessed October 31, 2023.
<https://www.sst.net/service/quenching-heat-treatment/>.
- [110] Fractory. “Tempering Explained | Definition, Process, Benefits and More,” December 19, 2022.
<http://https%253A%252F%252Ffractory.com%252Ftempering-explained%252F>.
- [111] HÄRTHA GROUP. “Quenching and Tempering.” Accessed October 31, 2023.
<https://haertha.de/en/process/vergueten/>.
- [112] “What Is the Difference Between Tempering and Annealing? - TWI.” Accessed October 31, 2023. <https://www.twi-global.com/technical-knowledge/faqs/annealing-vs-tempering>.
- [113] “JMMP | Free Full-Text | Microstructure Evolution in Inconel 718 Produced by Powder Bed Fusion Additive Manufacturing.” Accessed December 3, 2023. <https://www.mdpi.com/2504-4494/6/1/20>.
- [114] Shamsdini, SeyedAmirReza, M. H. Ghoncheh, and Mohsen Mohammadi. “Effect of Recoater-Blade Type on the Mechanical Properties and Microstructure of Additively Manufactured Maraging Steels.” *Materials Science and Engineering: A* 812 (April 22, 2021): 141104.
<https://doi.org/10.1016/j.msea.2021.141104>.

- [115] Kozhevnikov, Andrei, Rudie P.J. Kunnen, Gregor E. van Baars, and Herman J.H. Clercx. “Investigation of the Fluid Flow during the Recoating Process in Additive Manufacturing.” *Rapid Prototyping Journal* 26, no. 4 (January 1, 2020): 605–13. <https://doi.org/10.1108/RPJ-06-2019-0152>.
- [116] Snow, Zackary, Richard Martukanitz, and Sanjay Joshi. “On the Development of Powder Spreadability Metrics and Feedstock Requirements for Powder Bed Fusion Additive Manufacturing.” *Additive Manufacturing* 28 (August 1, 2019): 78–86. <https://doi.org/10.1016/j.addma.2019.04.017>.
- [117] Daňa, Milan, Ivana Zetková, and Pavel Hanzl. “The Influence of a Ceramic Recoater Blade on 3D Printing Using Direct Metal Laser Sintering.” *Manufacturing Technology* 19, no. 1 (February 1, 2019): 23–28. <https://doi.org/10.21062/ujep/239.2019/a/1213-2489/MT/19/1/23>.
- [118] M. J. Donachie, S. J. Donachie, *Superalloys: A Technical Guide*, 2nd Edition, 2002, ASM International, Materials Park, OH
- [119] IMR Test Labs. “ICP Analysis Services.” <https://imrtest.com/chemical-analysis-services/icp-analysis/>.
- [120] AZoM.com. “Exploring Extensometers - What Are They and Why Are They Used,” March 5, 2021. <https://www.azom.com/article.aspx?ArticleID=20189>.
- [121] Saba, N., M. Jawaid, and M. T. H. Sultan. “1 - An Overview of Mechanical and Physical Testing of Composite Materials.” In *Mechanical and Physical Testing of Biocomposites, Fibre-Reinforced Composites and Hybrid Composites*, edited by Mohammad Jawaid, Mohamed Thariq, and Naheed Saba, 1–12. Woodhead Publishing Series in Composites Science and Engineering. Woodhead Publishing, 2019. <https://doi.org/10.1016/B978-0-08-102292-4.00001-1>.

- [122] “Elongation - Matmatch.” <https://matmatch.com/learn/property/elongation>.
- [123] “Elongation: Definition, How To Calculate, and Importance.”
<https://www.xometry.com/resources/3d-printing/elongation/>.
- [124] “Ultimate Tensile Strength (UTS): Definition, How It Works, Calculation, and Example.”
Accessed November 10, 2023. <https://www.xometry.com/resources/materials/ultimate-tensile-strength/>.
- [125] Materion Brush Performance Alloys. (2012, November). Yield strength and other near-elastic properties- Materion. <https://materion.com/-/media/files/alloy/newsletters/technical-tidbits/issue-no-47---yield-strength-and-other-near-elastic-properties.pdf>
- [126] Yield strength and offset yield Rp 0.2. “Yield Strength and Offset Yield Rp 0.2.” Accessed November 10, 2023. <https://www.zwickroell.com/industries/materials-testing/tensile-test/yield-point/>.
- [127] Silbernagel, Cassidy, Leonidas Gargalis, Ian Ashcroft, Richard Hague, Mikiel Galea, and Philip Dickens. *Electrical Resistivity of Pure Copper Processed by Medium-Powered Laser Powder Bed Fusion Additive Manufacturing for Use in Electromagnetic Applications. Additive Manufacturing*. Vol. 29, 2019. <https://doi.org/10.1016/j.addma.2019.100831>.
- [128] “Fractography | Nanoscience Instruments.” Accessed November 15, 2023.
<https://www.nanoscience.com/applications/fractography/>.
- [129] Radhika, N., Manu Sam, and Thirumalini Subramaniam. “Experimental Studies on Mechanical and Wear Behaviour of TiC Reinforced Cu-Sn-Ni Functionally Graded Composite.” *Tribology in Industry* 41 (December 15, 2019): 537–47. <https://doi.org/10.24874/ti.2019.41.04.07>.

- [130] Nuclear Power. “Ductility - What Is Ductile Material.” Accessed November 22, 2023.
<https://www.nuclear-power.com/nuclear-engineering/materials-science/material-properties/ductility/>.
- [131] Inconel alloy 718 (Sept 07) web - special metals corporation. Special Metals. (n.d.). Table 6.
<https://www.specialmetals.com/documents/technical-bulletins/inconel/inconel-alloy-718.pdf>
- [132] Alloy 718 (AMS 5662 and 5663). Veostalpine. (n.d.).
<https://www.voestalpine.com/specialtymetals/nam/en/alloy-718-ams-5662-and-5663/>
- [133] “Vickers Hardness Testing.” <https://www.hardnesstesters.com/test-types/vickers-hardness-testing>.
- [134] Schur, R., S. Ghods, E. Schultz, C. Wisdom, R. Pahuja, A. Montelione, D. Arola, and M. Ramulu. “A Fractographic Analysis of Additively Manufactured Ti6Al4V by Electron Beam Melting: Effects of Powder Reuse.” *Journal of Failure Analysis and Prevention* 20, no. 3 (June 1, 2020): 794–803. <https://doi.org/10.1007/s11668-020-00875-0>.
- [135] Parrington, Ronald J. “Fractography of Metals and Plastics.” In *Plastics Failure Analysis and Prevention*, edited by John Moalli, 127–34. Plastics Design Library. Norwich, NY: William Andrew Publishing, 2001. <https://doi.org/10.1016/B978-188420792-1.50018-4>.
- [136] Thomas, Sebastian, and Christopher Hutchinson. “Delivering Microstructural Complexity to Additively Manufactured Metals through Controlled Mesoscale Chemical Heterogeneity.” *Acta Materialia* in press (January 10, 2022). <https://doi.org/10.1016/j.actamat.2022.117637>.
- [137] “Compass.” <https://compass.astm.org/document/?contentCode=ASTM%7CE0112-13R21%7Cen-US&proxycl=https%3A%2F%2Fsecure.astm.org&fromLogin=true>.

- [138] Deng, Dunyong, Ru Lin Peng, Håkan Brodin, and Johan Moverare. “Microstructure and Mechanical Properties of Inconel 718 Produced by Selective Laser Melting: Sample Orientation Dependence and Effects of Post Heat Treatments.” *Materials Science and Engineering: A* 713 (January 24, 2018): 294–306. <https://doi.org/10.1016/j.msea.2017.12.043>.
- [139] Test methods for tension testing of metallic materials. (n.d.). ASTM International. https://doi.org/10.1520/e0008_e0008m-21
- [140] “718 - National Specialty Alloys.” <https://www.nsalloys.com/products/nickel-alloy-bar/718inconel-nickel-alloy-bar.html>.

APPENDIX A

Method

Null hypothesis All variances are equal
 Alternative hypothesis At least one variance is different
 Significance level $\alpha = 0.05$

95% Bonferroni Confidence Intervals for Standard Deviations

Recoater	Scan speed	N	StDev	CI
Brush	960	12	9.9617	(6.40352, 19.7329)
CFB	960	12	8.7590	(6.06270, 16.1132)
HSS	960	12	9.3294	(5.80165, 19.1028)
Soft Recoater	960	12	12.1123	(8.03923, 23.2368)
Steel	*	11	8.1579	(5.78819, 15.0133)

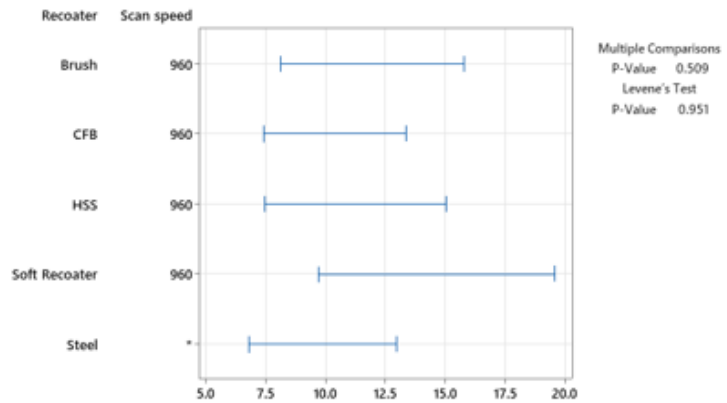
Individual confidence level = 99%

Tests

Method	Test	
	Statistic	P-Value
Multiple comparisons	—	0.509
Levene	0.17	0.951

Test for Equal Variances: Stress At 0.2% Offset Yield vs Recoater, Scan speed

Multiple comparison intervals for the standard deviation, $\alpha = 0.05$



If intervals do not overlap, the corresponding stdevs are significantly different.

Test for Equal Variances: Stress At 0.2% Offset Yield vs Recoater, Scan Speed M280

Method

Null hypothesis All means are equal
 Alternative hypothesis Not all means are equal
 Significance level $\alpha = 0.05$
 Rows unused 1

Equal variances were assumed for the analysis.

Factor Information

Factor	Levels	Values
Recoater	5	Brush, CFB, HSS, Soft Recoater, Steel

Analysis of Variance

Source	DF	Adj SS	Adj MS	F-Value	P-Value
Recoater	4	16590	4147.38	43.30	0.000
Error	54	5172	95.78		
Total	58	21762			

Model Summary

S	R-sq	R-sq(adj)	R-sq(pred)
9.78683	76.23%	74.47%	71.65%

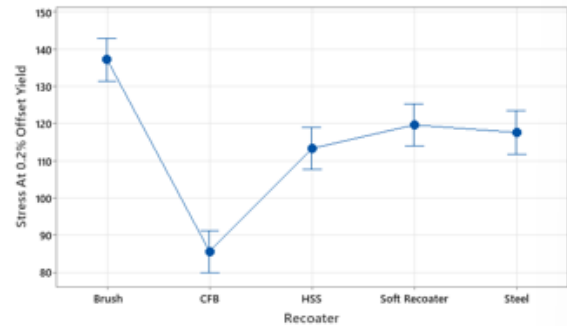
Means

Recoater	N	Mean	StDev	95% CI
Brush	12	137.06	9.96	(131.40, 142.73)
CFB	12	85.55	8.76	(79.89, 91.22)
HSS	12	113.22	9.33	(107.56, 118.89)
Soft Recoater	12	119.55	12.11	(113.89, 125.21)
Steel	11	117.52	8.16	(111.60, 123.44)

Pooled StDev = 9.78683

Interval Plot of Stress At 0.2% Offset Yield vs Recoater

95% CI for the Mean



The pooled standard deviation is used to calculate the intervals.

One-Way ANOVA: Stress At 0.2% Offset Yield vs Recoater, M280

Method

Null hypothesis All variances are equal
 Alternative hypothesis At least one variance is different
 Significance level $\alpha = 0.05$

95% Bonferroni Confidence Intervals for Standard Deviations

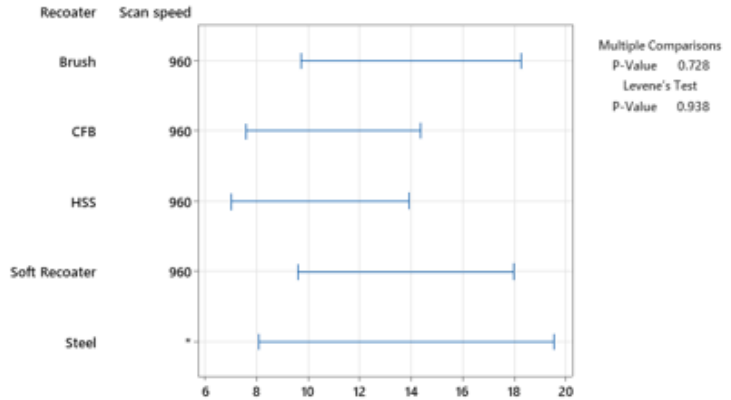
Recoater	Scan speed	N	StDev	CI
Brush	960	12	11.7117	(7.75888, 22.5103)
CFB	960	12	9.1921	(6.27950, 17.1335)
HSS	960	12	8.6979	(5.78170, 16.6614)
Soft Recoater	960	12	11.5563	(7.66320, 22.1904)
Steel	*	12	11.0479	(6.14038, 25.3107)

Individual confidence level = 99%

Tests

Method	Test Statistic	P-Value
Multiple comparisons	—	0.728
Levene	0.20	0.938

Test for Equal Variances: Ultimate Tensile Stress vs Recoater, Scan speed
 Multiple comparison intervals for the standard deviation, $\alpha = 0.05$



If intervals do not overlap, the corresponding stdevs are significantly different.

Test for Equal Variances: Ultimate Tensile Stress vs Recoater, Scan Speed M280

Method

Null hypothesis All means are equal
 Alternative hypothesis Not all means are equal
 Significance level $\alpha = 0.05$

Equal variances were assumed for the analysis.

Factor Information

Factor	Levels	Values
Recoater	5	Brush, CFB, HSS, Soft Recoater, Steel

Model Summary

S	R-sq	R-sq(adj)	R-sq(pred)
10.5159	67.77%	65.43%	61.64%

Analysis of Variance

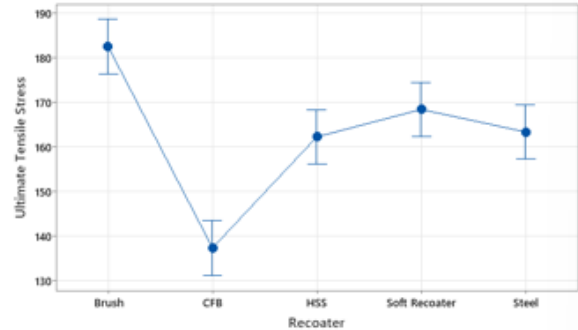
Source	DF	Adj SS	Adj MS	F-Value	P-Value
Recoater	4	12788	3197.1	28.91	0.000
Error	55	6082	110.6		
Total	59	18870			

Means

Recoater	N	Mean	StDev	95% CI
Brush	12	182.42	11.71	(176.34, 188.51)
CFB	12	137.32	9.19	(131.23, 143.40)
HSS	12	162.19	8.70	(156.10, 168.27)
Soft Recoater	12	168.34	11.56	(162.26, 174.43)
Steel	12	163.30	11.05	(157.21, 169.38)

Pooled StDev = 10.5159

Interval Plot of Ultimate Tensile Stress vs Recoater
 95% CI for the Mean



The pooled standard deviation is used to calculate the intervals.

One-Way ANOVA: Ultimate Tensile Stress vs Recoater, M280

Method

Null hypothesis All variances are equal
 Alternative hypothesis At least one variance is different
 Significance level $\alpha = 0.05$

95% Bonferroni Confidence Intervals for Standard Deviations

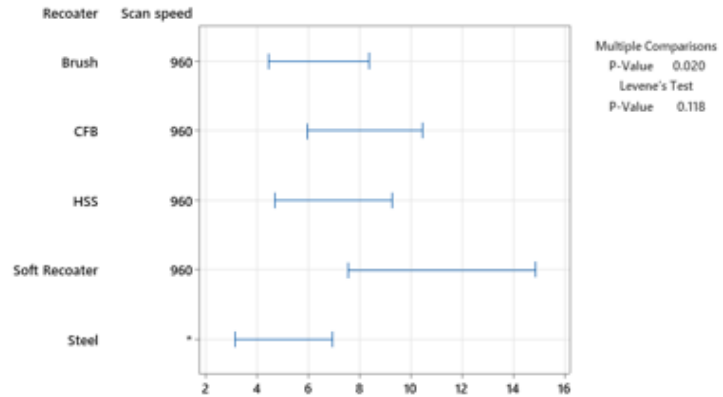
Recoater	Scan speed	N	StDev	CI
Brush	960	12	5.38037	(3.54260, 10.4050)
CFB	960	12	6.94496	(4.87187, 12.6061)
HSS	960	12	5.81974	(3.68213, 11.7124)
Soft Recoater	960	12	9.33314	(6.62106, 16.7520)
Steel	*	11	4.08406	(2.89969, 7.5110)

Individual confidence level = 99%

Tests

Method	Test	
	Statistic	P-Value
Multiple comparisons	—	0.020
Levene	1.93	0.118

Test for Equal Variances: Elongation % at Fracture vs Recoater, Scan speed
 Multiple comparison intervals for the standard deviation, $\alpha = 0.05$



If intervals do not overlap, the corresponding stdevs are significantly different.

Test for Equal Variances: Elongation % at Fracture vs Recoater, Scan Speed M280

Method

Null hypothesis All means are equal
 Alternative hypothesis Not all means are equal
 Significance level $\alpha = 0.05$
 Rows unused 1

Equal variances were assumed for the analysis.

Factor Information

Factor	Levels	Values
Recoater	5	Brush, CFB, HSS, Soft Recoater, Steel

Model Summary

S	R-sq	R-sq(adj)	R-sq(pred)
6.59198	44.79%	40.71%	34.22%

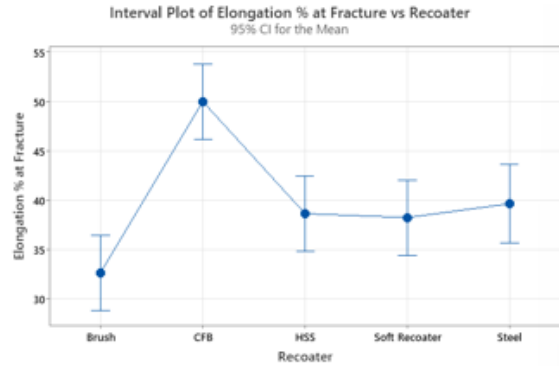
Analysis of Variance

Source	DF	Adj SS	Adj MS	F-Value	P-Value
Recoater	4	1904	476.00	10.95	0.000
Error	54	2347	43.45		
Total	58	4251			

Means

Recoater	N	Mean	StDev	95% CI
Brush	12	32.65	5.38	(28.83, 36.46)
CFB	12	49.98	6.94	(46.16, 53.79)
HSS	12	38.63	5.82	(34.81, 42.44)
Soft Recoater	12	38.23	9.33	(34.41, 42.04)
Steel	11	39.64	4.08	(35.65, 43.62)

Pooled StDev = 6.59198



The pooled standard deviation is used to calculate the intervals.

One-Way ANOVA: Elongation % at Fracture vs Recoater, M280

Method

Null hypothesis All variances are equal
 Alternative hypothesis At least one variance is different
 Significance level $\alpha = 0.05$

95% Bonferroni Confidence Intervals for Standard Deviations

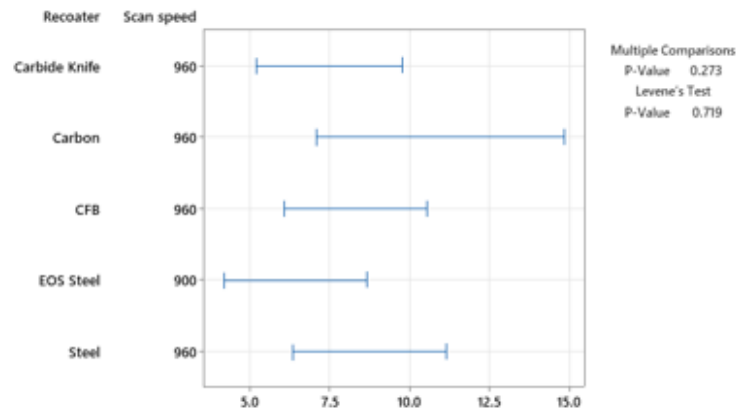
Recoater	Scan speed	N	StDev	CI
Carbide Knife	960	12	6.27487	(4.15583, 12.0639)
Carbon	960	12	9.03441	(5.97462, 17.3951)
CFB	960	12	7.03412	(4.84068, 12.7518)
EOS Steel	900	12	5.30493	(3.32122, 10.7895)
Steel	960	12	7.39975	(5.14928, 13.5402)

Individual confidence level = 99%

Tests

Method	Test	
	Statistic	P-Value
Multiple comparisons	—	0.273
Levene	0.52	0.719

Test for Equal Variances: Stress At 0.2% Offset Yield vs Recoater, Scan speed
 Multiple comparison intervals for the standard deviation, $\alpha = 0.05$



If intervals do not overlap, the corresponding stdevs are significantly different.

Test for Equal Variances: Stress At 0.2% Offset Yield vs Recoater, Scan Speed M290

Method

Null hypothesis All means are equal
 Alternative hypothesis Not all means are equal
 Significance level $\alpha = 0.05$
 Equal variances were assumed for the analysis.

Factor Information

Factor	Levels	Values
Recoater	5	Carbide Knife, Carbon, CFB, EOS Steel, Steel

Model Summary

S	R-sq	R-sq(adj)	R-sq(pred)
5.50217	58.73%	55.73%	50.88%

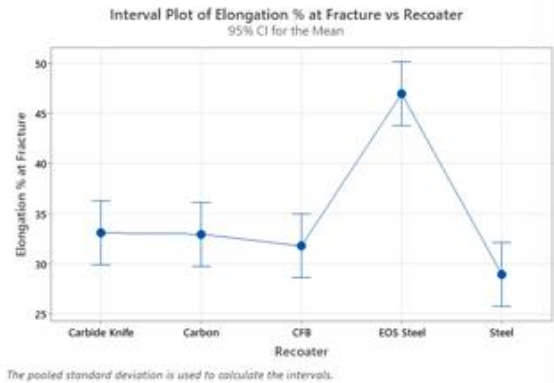
Analysis of Variance

Source	DF	Adj SS	Adj MS	F-Value	P-Value
Recoater	4	2369	592.35	19.57	0.000
Error	55	1665	30.27		
Total	59	4034			

Means

Recoater	N	Mean	StDev	95% CI
Carbide Knife	12	33.06	5.79	(29.88, 36.25)
Carbon	12	32.94	6.24	(29.75, 36.12)
CFB	12	31.75	4.00	(28.57, 34.93)
EOS Steel	12	46.94	5.90	(43.75, 50.12)
Steel	12	28.94	5.31	(25.75, 32.12)

Pooled StDev = 5.50217



The pooled standard deviation is used to calculate the intervals.

One-Way ANOVA: Stress At 0.2% Offset Yield vs Recoater, M290

Method

Null hypothesis All variances are equal
 Alternative hypothesis At least one variance is different
 Significance level $\alpha = 0.05$

95% Bonferroni Confidence Intervals for Standard Deviations

Recoater	Scan speed	N	StDev	CI
Carbide Knife	960	12	10.8238	(7.29505, 20.4487)
Carbon	960	12	11.4068	(7.62007, 21.7423)
CFB	960	12	6.9248	(5.18423, 11.7780)
EOS Steel	900	12	8.1330	(5.22067, 16.1331)
Steel	960	12	11.1939	(7.65815, 20.8340)

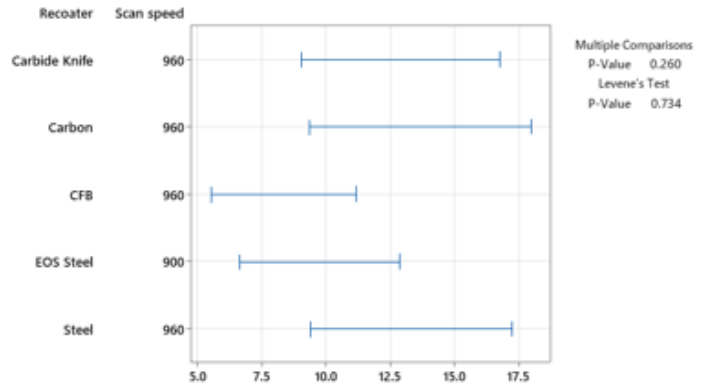
Individual confidence level = 99%

Tests

Method	Test	
	Statistic	P-Value
Multiple comparisons	---	0.260
Levene	0.50	0.734

Test for Equal Variances: Ultimate Tensile Stress vs Recoater, Scan speed

Multiple comparison intervals for the standard deviation, $\alpha = 0.05$



If intervals do not overlap, the corresponding stdevs are significantly different.

Test for Equal Variances: Ultimate Tensile Stress vs Recoater, Scan Speed M290

Method

Null hypothesis All means are equal
 Alternative hypothesis Not all means are equal
 Significance level $\alpha = 0.05$

Equal variances were assumed for the analysis.

Factor Information

Factor	Levels	Values
Recoater	5	Carbide Knife, Carbon, CFB, EOS Steel, Steel

Analysis of Variance

Source	DF	Adj SS	Adj MS	F-Value	P-Value
Recoater	4	16937	4234.22	43.50	0.000
Error	55	5353	97.33		
Total	59	22290			

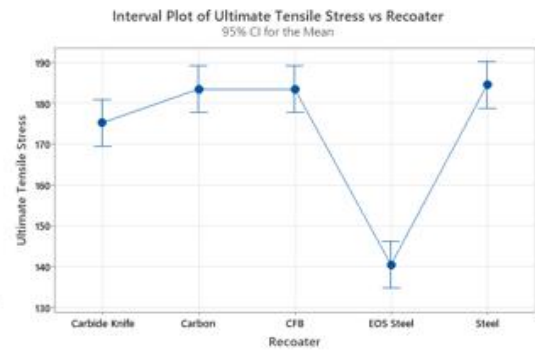
Model Summary

S	R-sq	R-sq(adj)	R-sq(pred)
9.86581	75.98%	74.24%	71.42%

Means

Recoater	N	Mean	StDev	95% CI
Carbide Knife	12	175.21	10.82	(169.50, 180.92)
Carbon	12	183.43	11.41	(177.73, 189.15)
CFB	12	183.44	6.92	(177.73, 189.15)
EOS Steel	12	140.49	8.13	(134.78, 146.19)
Steel	12	184.50	11.19	(178.79, 190.21)

Pooled StDev = 9.86581



One- Way ANOVA: Ultimate Tensile Stress vs Recoater, M290

Method

Null hypothesis All variances are equal
 Alternative hypothesis At least one variance is different
 Significance level $\alpha = 0.05$

95% Bonferroni Confidence Intervals for Standard Deviations

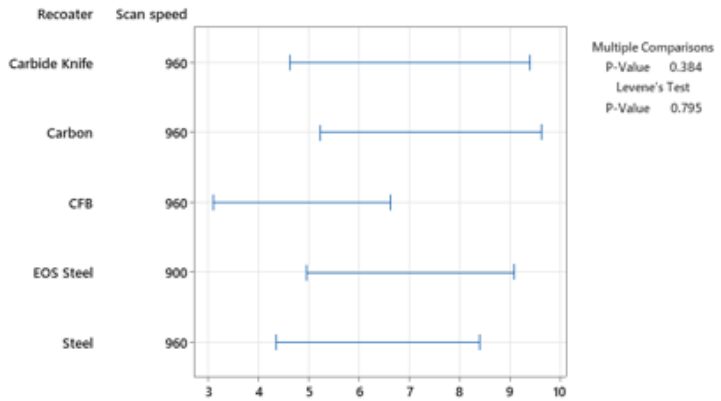
Recoater	Scan speed	N	StDev	CI
Carbide Knife	960	12	5.78804	(3.61629, 11.7961)
Carbon	960	12	6.23783	(4.21894, 11.7436)
CFB	960	12	3.99574	(2.67602, 7.5970)
EOS Steel	900	12	5.89696	(3.95936, 11.1833)
Steel	960	12	5.31200	(3.40614, 10.5485)

Individual confidence level = 99%

Tests

Method	Test Statistic	P-Value
Multiple comparisons	—	0.384
Levene	0.42	0.795

Test for Equal Variances: Elongation % at Fracture vs Recoater, Scan speed
 Multiple comparison intervals for the standard deviation, $\alpha = 0.05$



If intervals do not overlap, the corresponding stdevs are significantly different.

Test for Equal Variances: Elongation % at Fracture vs Recoater, Scan Speed M290

Method

Null hypothesis All means are equal
 Alternative hypothesis Not all means are equal
 Significance level $\alpha = 0.05$

Equal variances were assumed for the analysis.

Factor Information

Factor	Levels	Values
Recoater	5	Carbide Knife, Carbon, CFB, EOS Steel, Steel

Model Summary

S	R-sq	R-sq(adj)	R-sq(pred)
7.11859	91.12%	90.48%	89.43%

Analysis of Variance

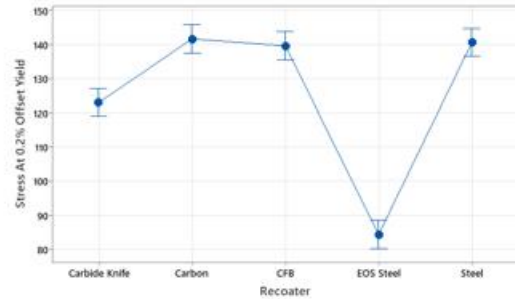
Source	DF	Adj SS	Adj MS	F-Value	P-Value
Recoater	4	28603	7150.64	141.11	0.000
Error	55	2787	50.67		
Total	59	31390			

Means

Recoater	N	Mean	StDev	95% CI
Carbide Knife	12	123.00	6.27	(118.89, 127.12)
Carbon	12	141.61	9.03	(137.50, 145.73)
CFB	12	139.58	7.03	(135.46, 143.70)
EOS Steel	12	84.36	5.30	(80.24, 88.48)
Steel	12	140.59	7.40	(136.47, 144.70)

Pooled StDev = 7.11859




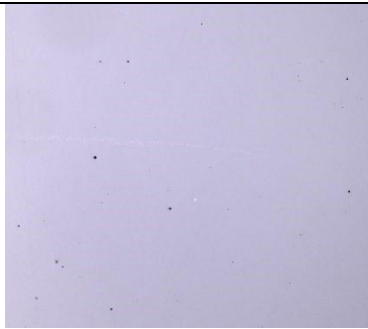
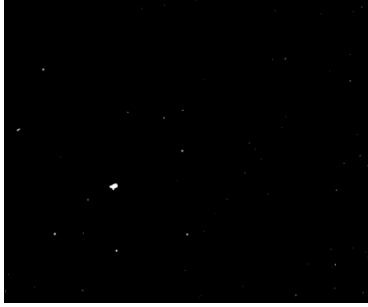
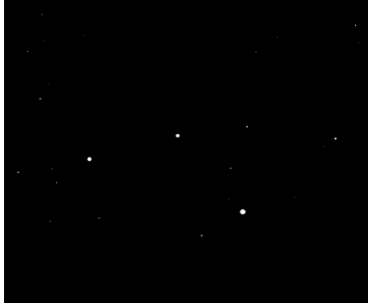

Interval Plot of Stress At 0.2% Offset Yield vs Recoater
 95% CI for the Mean







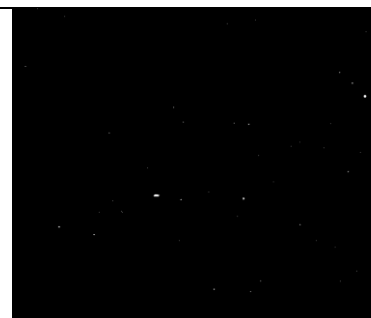

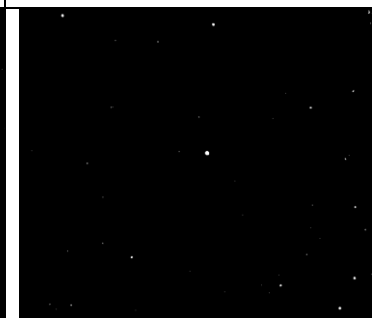
The pooled standard deviation is used to calculate the intervals.

One-Way ANOVA: Elongation % at Fracture vs Recoater, M290


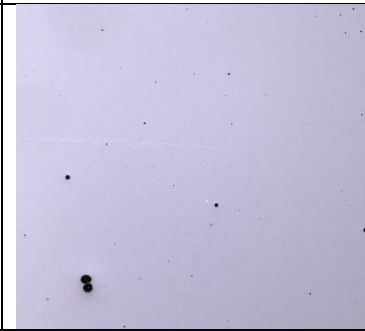
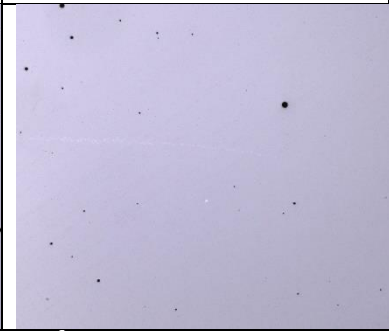
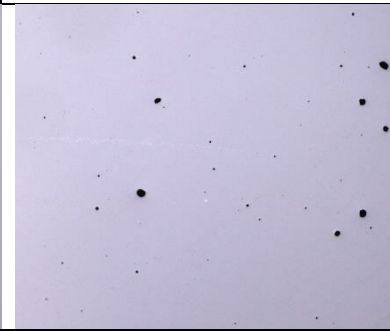



APPENDIX B

	45°	60°	90°
			
Plate 1 EOS M400			
			
	Average Porosity Size (μm): 20.4 Density of material: 99.93%	Average Porosity Size (μm):43.4 Density of material: 99.94%	Average Porosity Size (μm): 22.6 Density of material: 99.96%







As polished micrographs of plates 1, 6, 9, 10, 11, 12, 15 with their respective angles 45, 60, 90 are illustrated at 50x magnification 200 μm .

	45°	60°	90°
 Plate 6 EOS M280			
			
	Average Porosity Size (μm): 16.5 Density of material: 99.96%	Average Porosity Size (μm): 17 Density of material: 99.96%	Average Porosity Size (μm): 23 Density of material: 99.94%







As polished micrographs of plates 1, 6, 9, 10, 11, 12, 15 with their respective angles 45, 60, 90 are illustrated at 50x magnification 200 μm.

			
	45°	60°	90°
Plate 7 Concept M2			
			
	Average Porosity Size (μm): 89 Density of material: 99.78%	Average Porosity Size (μm): 85.7 Density of material: 99.78%	Average Porosity Size (μm): 189 Density of material: 99.63%









As polished micrographs of plates 1, 6, 9, 10, 11, 12, 15 with their respective angles 45, 60, 90 are illustrated at 50x magnification 200 μm .

	45°	60°	90°
Plate 9 EOS M290			
			
	Average Porosity Size (μm): 19 Density of material: 99.88%	Average Porosity Size (μm): 20.6 Density of material: 99.94%	Average Porosity Size (μm): 17.4 Density of material: 99.93%







As polished micrographs of plates 1, 6, 9, 10, 11, 12, 15 with their respective angles 45, 60, 90 are illustrated at 50x magnification 200 μm .

	45°	60°	90°
Plate 10 SLM280			
			
	Average Porosity Size (μm): 33.9 Density of material: 99.93%	Average Porosity Size (μm): 28.3 Density of material: 99.92%	Average Porosity Size (μm): 12.3 Density of material: 99.93%








As polished micrographs of plates 1, 6, 9, 10, 11, 12, 15 with their respective angles 45, 60, 90 are illustrated at 50x magnification 200 μm .

	45°	60°	90°
Plate 11 SLM280 -Dual			
			
	Average Porosity Size (μm): 34.9 Density of material: 99.81%	Average Porosity Size (μm): 35 Density of material: 99.84%	Average Porosity Size (μm): 23 Density of material: 99.94%




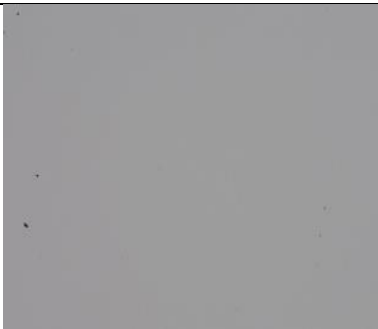


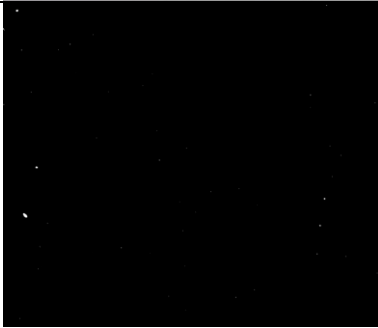
As polished micrographs of plates 1, 6, 9, 10, 11, 12, 15 with their respective angles 45, 60, 90 are illustrated at 50x magnification 200 μm .

	45°	60°	90°
Plate 12 Velo Sapphire			
			
	Average Porosity Size (μm): 13 Density of material: 99.78%	Average Porosity Size (μm): 11.4 Density of material: 99.79%	Average Porosity Size (μm): 21.5 Density of material: 99.9%

As polished micrographs of plates 1, 6, 9, 10, 11, 12, 15 with their respective angles 45, 60, 90 are illustrated at 50x magnification 200 μm .





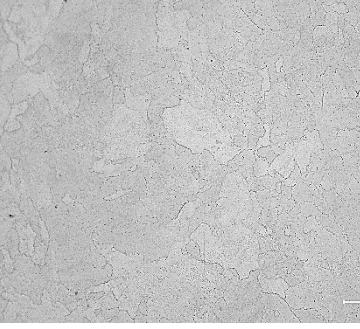
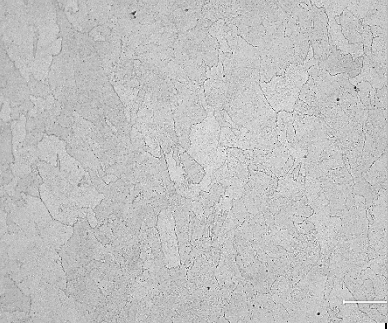
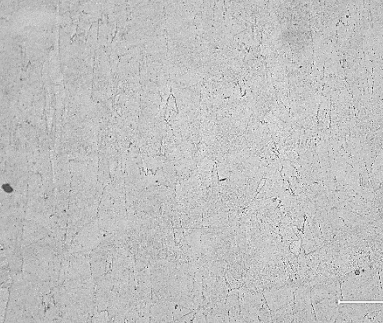
			
	45°	60°	90°
Plate 15 EOS M280			
			
	Average Porosity Size (μm): 8.6 Density of material: 99.6%	Average Porosity Size (μm): 6 Density of material: 99.74%	Average Porosity Size (μm): 6.9 Density of material: 99.88%






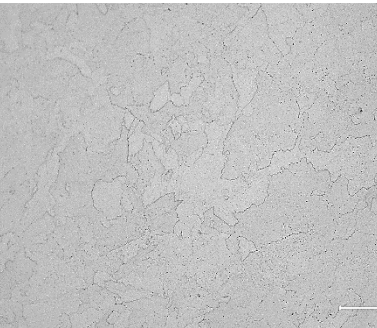
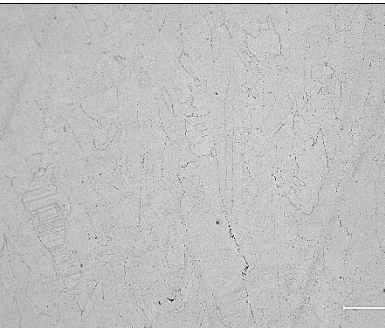
As polished micrographs of plates 1, 6, 9, 10, 11, 12, 15 with their respective angles 45, 60, 90 are illustrated at 50x magnification 200 μm .

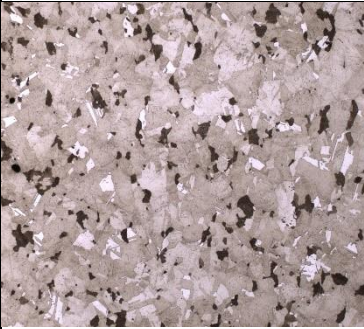
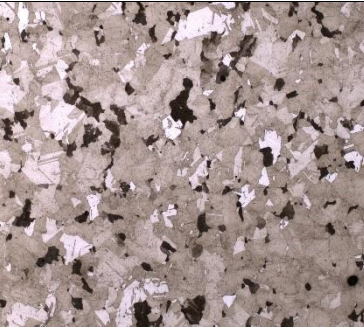

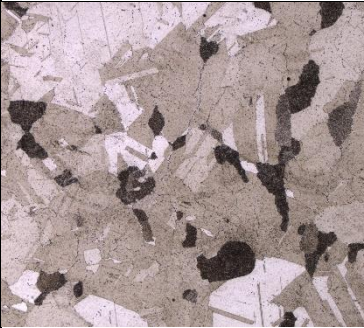
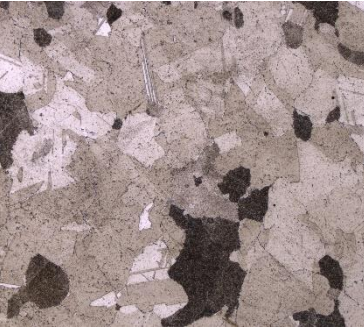

			
	45°	60°	90°
No Heat Treatment			
			
	Average Porosity Size (µm): 4 Density of material: 99.98%	Average Porosity Size (µm): 6.7 Density of material: 99.97%	Average Porosity Size (µm): 6.3 Density of material: 99.98%


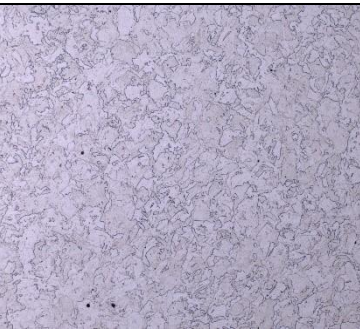
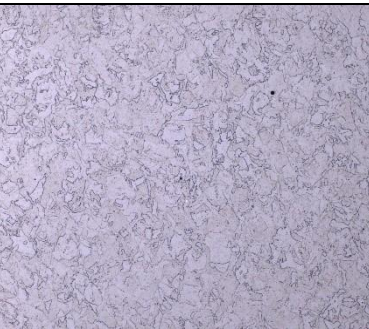
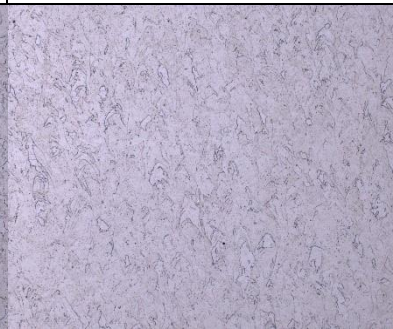
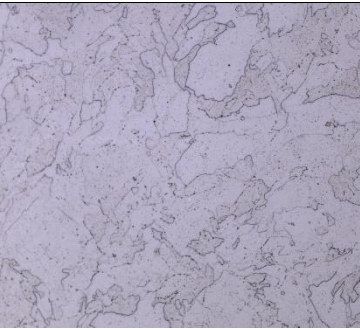
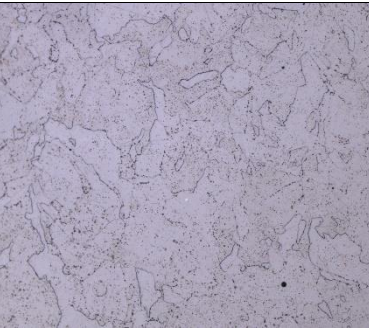

As polished micrographs of plates 1, 6, 9, 10, 11, 12, 15 with their respective angles 45, 60, 90 are illustrated at 50x magnification 200 µm.


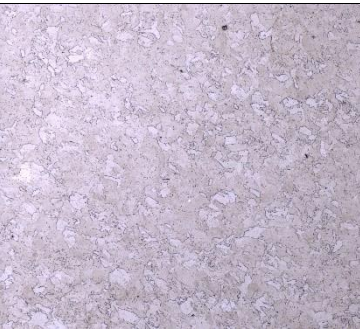
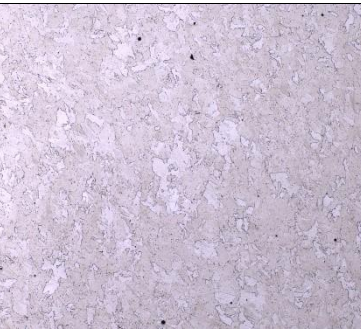

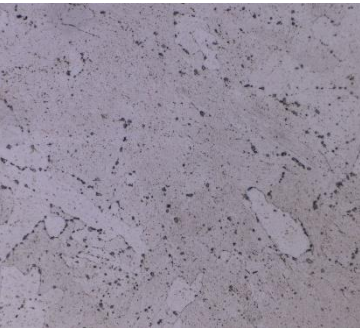

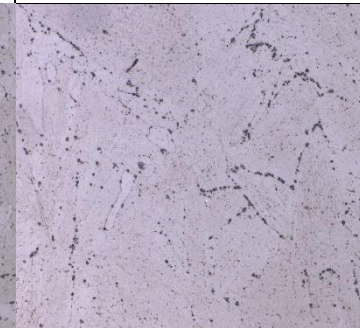
APPENDIX C


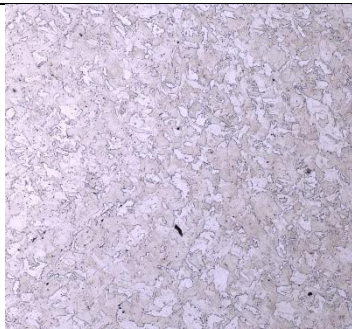
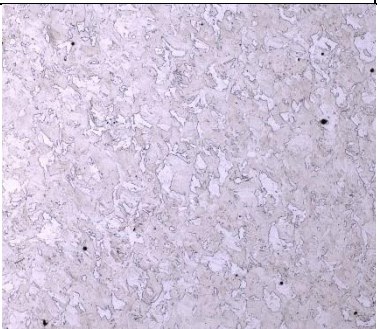
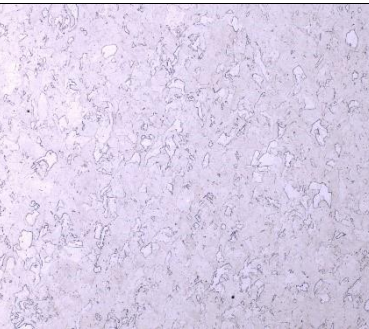
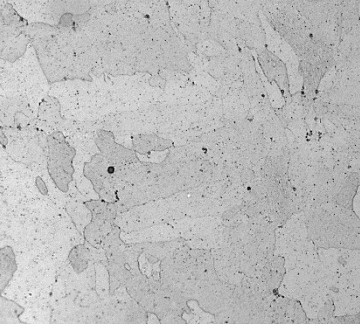
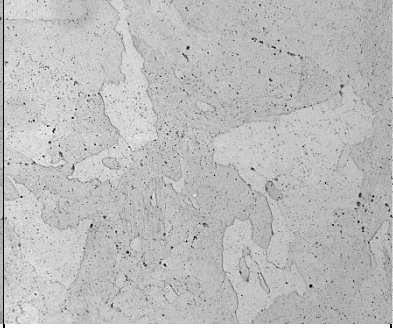
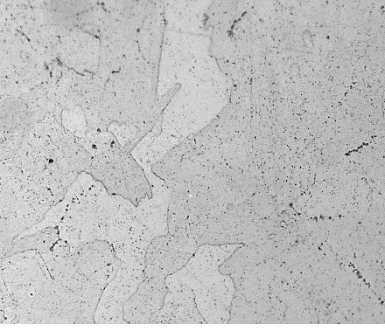
			
	45°	60°	90°
Plate 1 EOS M400 50x mag. (200μm)			
500x mag. (200μm)			
Grain Size:	28.9μm	28.35 μm	30.05 μm





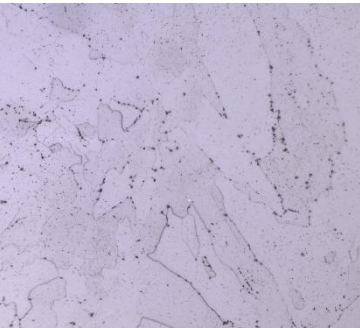
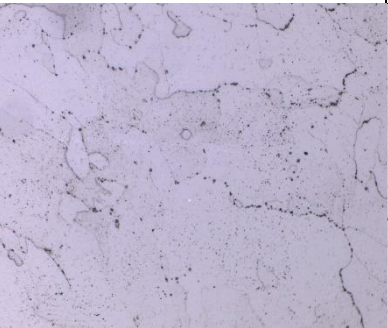
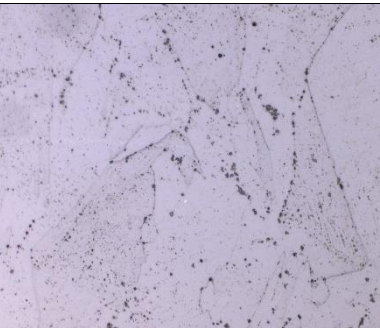
	45°	60°	90°
 Plate 6 EOS M280 50x mag. (200μm)			
500x mag. (200μm)			
Grain Size:	23.19 μm	31.05 μm	22.30 μm





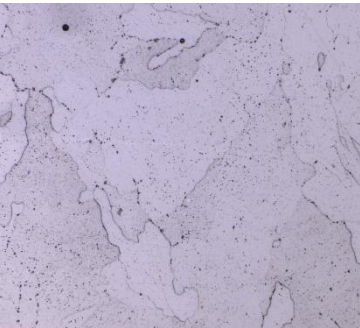
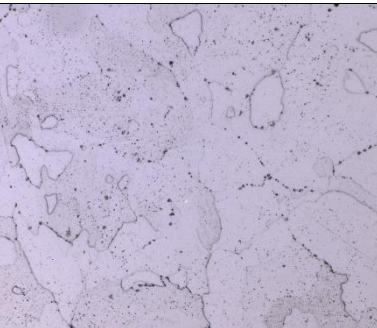
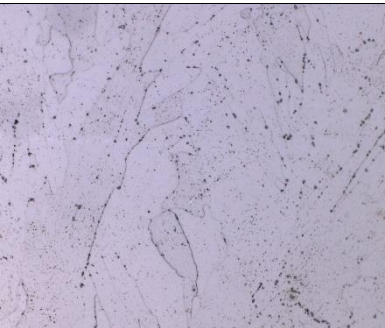
		45°	60°	90°
Plate 7 Concept M2	50x mag. (200μm)			
	500x mag. (200μm)			
Grain Size:		24.14 μm	28.14 μm	42 μm






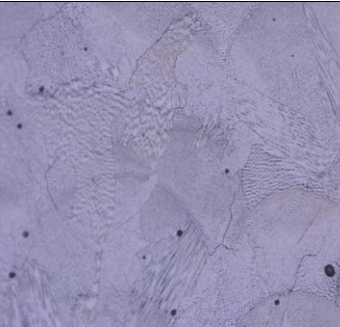
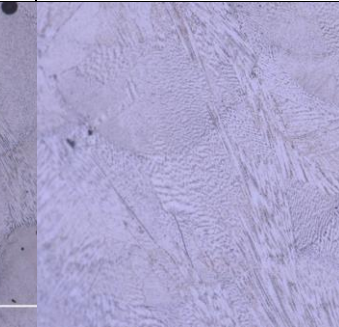
	45°	60°	90°
 Plate 9 EOS M290 50x mag. (200μm)			
500x mag. (200μm)			
Grain Size:	29.44 μm	33.88 μm	56.20 μm

			
	45°	60°	90°
Plate 10 SLM 280 50x mag. (200μm)			
500x mag. (200μm)			
Grain Size:	20.6 μm	17.63 μm	23.5 μm

	45°	60°	90°
 Plate 11 SLM 280- Dual 50x mag. (200μm)			
500x mag. (200μm)			
Grain Size:	21.15 μm	21.24 μm	51.77 μm

			
	45°	60°	90°
Plate 12 Velo Sapphire 50x mag. (200μm)			
500x mag. (200μm)			
Grain Size:	19.84μm	21.60μm	27.74 μm

			
	45°	60°	90°
Plate 15 EOS M280 50x mag. (200μm)			
500x mag. (200μm)			
Grain Size:	22.43μm	23.78μm	19.74 μm

	45°	60°	90°
			
No Heat Treatment			
50x mag. (200μm)			
Melt Pool Size:	Width: 110.36 μm Depth: 90.66 μm	Width: 102.78 μm Depth: 94.44 μm	Width: 106.06 μm Depth: 78.54 μm
500x mag. (50μm)			
Grain Size:	29.53μm	14.17μm	28.11 μm

Vita

Laura Marquez earned her Bachelor of Science in Mechanical Engineering in May 2022 from The University of Texas at El Paso, where she honed her engineering skills and developed a passion for advanced additive manufacturing techniques. Throughout her academic journey, Laura had the privilege of working as a Research Assistant at the W.M. Keck Center, affiliated with the University of Texas at El Paso, where she contributed to cutting-edge research in 3D printing materials and processes. Additionally, she gained valuable practical experience during a summer internship at Lawrence Livermore National Laboratory in 2023, where she conducted experiments in powder deposition for Powder Bed Fusion systems, further enhancing her expertise in experimental design and data collection. Laura's dedication to innovation, along with her strong analytical and problem-solving skills, positions her as a valuable asset in research and development roles within the field of mechanical engineering.

Contact Information: limarquez3@miners.utep.edu